Mathematical Engineering, Statistics and Operations Research Doctoral Program

Universidad Politécnica de Madrid
and
Universidad Complutense de Madrid

On the use of a 3D glacier–plume model to estimate frontal ablation of marine–terminating glaciers

PhD thesis

Author: **José Manuel Muñoz Hermosilla**
Supervisor: **Jaime Otero García**

Madrid, 2024

UNIVERSIDAD POLITÉCNICA DE MADRID
Escuela Técnica Superior de Ingenieros de Telecomunicación

Doctoral Degree in Mathematical Engineering, Statistics and Operations Research

On the use of a 3D glacier–plume model to estimate frontal ablation of marine–terminating glaciers

DOCTORAL THESIS

Submitted for the degree of Doctor by:

José Manuel Muñoz Hermosilla
PhD Candidate

Under the supervision of:
Dr. Jaime Otero García

Madrid, 2024

Title: On the use of a 3D glacier–plume model to estimate frontal ablation of marine–terminating glaciers
Author: José Manuel Muñoz Hermosilla
Doctoral Programme: Mathematical Engineering, Statistics and Operations Research

Thesis Supervision:

Dr. Jaime Otero García, Senior Lecturer at Polytechnic University of Madrid (Supervisor)

External Reviewers:

Thesis Defense Committee:

Thesis Defense Date:

This thesis was carried out under project PID2020-113051RB-C31, funded by MCIN / AEI /10.13039/501100011033/ FEDER, UE, and grant PRE2018-084318 funded by MCIN / AEI /10.13039/501100011033 and the FSE 'El FSE invierte en tu futuro'. Field measurements in Hornsund were supported by the Polish–Norwegian project AWAKE-2 (contract No. Pol–Nor/198675/17/2013). Additional supporting field data were provided by the Hornsund Polish Polar Station.

A quienes llegaron.
A quienes no llegaron.
A las raíces que los sostienen.
A las hijas e hijos de la clase obrera.

Declaration

I hereby declare that except where specific reference is made to the work of others, the contents of this dissertation are original and have not been submitted in whole or in part for consideration for any other degree or qualification in this, or any other University. This dissertation is my own work and contains nothing which is the outcome of work done in collaboration with others, except where work which has formed part of jointly–authored publications has been included. The contribution of the candidate and the other authors to this work has been explicitly indicated below.

Chapter 4:

Citation: Munoz–Hermosilla, J. M.: A 3D glacier dynamics–line plume model to estimate frontal ablation of Hansbreen, Svalbar, The Cryosphere

Author contribution: JMM and JO designed the experiments. JMM also developed the model code and executed the experiments with contributions from JO. EA and KS provided surface mass balance and surface meltwater data. IP and JO provided surface velocities data. JMM analysed the model outputs and wrote the manuscript, with significant contributions from JO and FN. All authors contributed to and approved the final manuscript.

José Manuel Muñoz Hermosilla

June 2024

Acknowledgement

Esta investigación se ha llevado a cabo bajo el proyecto PID2020-113051RB-C31, financiado por el MCIN / AEI /10.13039/501100011033/ FEDER, UE, y bajo el contrato predoctoral PRE2018-084318 financiado por el MCIN / AEI /10.13039/501100011033 y el FSE ’El FSE invierte en tu futuro’. Los datos de campo en el área de Hornsund han sido proporcionados por el proyecto polaco-noruego AWAKE-2 (contrato no. Pol–Nor/198675/17/2013). Además, también para los datos de campo se ha contado con el apoyo adicional de la base polar polaca Honrsund.

Me gustaría agradecer a Jaime, mi director, por todas las horas dedicadas a sacar adelante un modelo que se resistió a arrancar más de dos años. También a Paco, mi tutor. A ambos les agradezco su guía, disposición y ayuda indispensable en el día a día de este trabajo, no solo en los contenidos propios de la tesis, sino también en los temás más allá de la propia investigación, como la burocracia inherente a este trabajo. Agradezco también a la Escuela Técncia Superior de Ingenieros de Telecomunicación, perteneciente a la Universidad Politécnica de Madrid, por proporcionarme un espacio de trabajo.

Al resto de componentes del Grupo de Simulación Numérica en Ciencias e Ingeniería (GSNCI): Javi, aunque fue poco el tiempo que compartimos trabajando; Ricardo, con quien además coincidí en la campaña antártica; Kaian y Unai, compañeros de fatigas; y finalmente Eva, con quien compartí despacho, discusiones y un congreso genial en el Ártico. Todos ellos han contribuido un poquito a este trabajo. También querría agradecer a Olivier Gagliardini y Tom Cowton por acogerme en mis estancias internacionales y ayudarme a discurrir los escollos que se me presentaban en ese momento, así como a Samuel Cook por su imprescindible ayuda para arrancar con el modelo después de tantos problemas.

Sin embargo, todo eso no habría podido ser posible sin la incombustible ayuda de mi familia, quienes siempre han confiado en mí y nunca han dudado de mis decisiones. Su esfuerzo y confianza han conseguido llevar a un niño que creció entre olivares a los lugares más inexplorados del mundo. Sin ellos, no podría estar escribiendo estas palabras en una tesis doctoral, ni tampoco sé que habría sido de mí en la vida. También he sentido siempre el apoyo de mis amigos, quienes, a pesar de estar lejos y no tener muy claro cuál es mi trabajo, siempre se han preocupado de hacerme llegar su energía y han estado ahí para cualquier cosa.

Finalmente, esto tampoco habría sido posible sin ti, mi compañera, que llegaste a mi vida cuando apenas comenzaba este proyecto y me has acompañado todo el camino. Has compartido conmigo los mejores y los peores momentos, que no han sido pocos. Gracias por celebrar los unos y apoyarme en los otros. Tu apoyo en el día a día ha sido fundamental.

Resumen

La criosfera comprende la parte de agua congelada en la Tierra e incluye elementos como nieve, glaciares, casquetes polares, mantos de hielo, hielo marino o permafrost. En conjunto, todos ellos constituyen aproximadamente el 70 % del agua dulce de todo el planeta. La extensión de todos estos elementos congelados cubre en torno al 21 % de la superficie terrestre, y los glaciares representan aproximadamente un 15 % del total del hielo. El actual contexto de cambio climático representa una amenaza contra el equilibrio de la criosfera ya que puede influir tanto en la dinámica y el balance de masas de los glaciares, como en los procesos térmicos y dinámicos de los océanos. Todo esto podría tener efectos sobre la hidrología y la ecología a nivel local y global. Uno de estos efectos es la subida del nivel del mar.

Aunque constituyen solamente una pequeña fracción del volumen total de hielo de los dos grandes mantos de hielo (Groenlandia y la Antártida), actualmente los glaciares están perdiendo más masa, y a una tasa similar o incluso superior, que cada uno de los mantos de hielo por separado. Es necesario, por tanto, entender que los glaciares, a pesar de su pequeño tamaño, son una parte importante de un sistema complejo en el que los efectos oceánicos y atmosféricos también juegan un papel esencial. Los *tidewater glaciers* (glaciares con terminación en el mar) son glaciares que terminan en el mar, ya sea a través de una lengua flotante o de un frente vertical anclado a tierra bajo el nivel del mar. En estos glaciares, una parte importante de la pérdida de masa es debida a la ablación frontal, y los principales contribuyentes a la ablación frontal son el *calving* o desprendimiento de icebergs y la fusión submarina. El *calving* es generalmente el principal contribuyente, sin embargo, la fusión submarina no solo ejerce un efecto directo sobre el frente glaciar, también puede promover más eventos de *calving* al inducir cambios en el campo de tensiones del frente. Por tanto, ambos procesos deben ser analizados conjuntamente. Entre los factores que afectan a los procesos de fusión submarina, uno de los procesos más importantes es la formación de plumas de flotabilidad debido a la descarga subglacial de agua dulce.

En este estudio se ha usado el programa Elmer/Ice para desarrollar un modelo 3D de dinámica glaciar. El modelo, que incluye *calving* e hidrología subglacial, y está acoplado con un modelo de pluma lineal, calcula la posición del frente glaciar para cada paso temporal. Este modelo se ha aplicado al sistema glaciar–fjordo Hansbreen–Hansbukta situado en el suroeste de la isla de Spitsbergen, Svalbard, debido a la disponibilidad de grandes series de datos en esa zona. El estudio se ha realizado para el período comprendido entre septiembre de 2008 y marzo de 2011 y los resultados indican que el modelo 3D es capaz de reproducir el ciclo estacional de avance y retroceso. Además, al comparar las posiciones del frente del modelo con las observadas se encuentra que tienen un buen grado de acuerdo si se tienen en cuenta solamente los 350 m centrales del frente, con diferencias longitudinales, de media, por debajo de los 15 metros entre diciembre de 2009 y marzo de 2011. Sin embargo, hay regiones en las que el frente modelado presenta mayores divergencias respecto al observado, especialmente en el margen este. Al mejorar el modelo refinando las velocidades de superficie e introduciendo las tres zonas de condiciones ambientales para el modelo de pluma, el nuevo frente modelado reproduce mejor la fase de retroceso del glaciar en comparación con el modelo anterior. Además, la diferencias entre las posiciones modeladas y observadas se han reducido ya que se han obtenido diferencias longitudinales más pequeñas (por debajo de 10 metros), y al mismo tiempo se han extendido los anteriores 350 metros centrales, en los que se consigue que el modelo reproduzca con bastante exactitud las posiciones del frente observadas, hasta los 700 metros centrales, que es la mitad del frente del glaciar. Pese a todo, el problema en el margen este persiste.

Finalmente, se ha llevado a cabo un análisis de sensibilidad que prueba que el modelo es estable a variaciones de las condiciones iniciales. El análisis también indica que el *calving* es más sensible a cambios en las velocidades iniciales, seguido de cambios en las condiciones ambientales del fiordo y, finalmente, a cambios en la fusión en superficie.

Abstract

Cryosphere refers to the parts of the Earth where water is frozen, and includes snow, glaciers and ice caps, ice sheets, lake and river ice, sea ice, permafrost and seasonally frozen ground. Combined, all these elements constitute $\sim$70 % of the planet's total freshwater. The extension of the frozen components covers around 21 % of the Earth's surface, with glaciers representing around 0.15 % of the total of the ice. The ongoing climate change context represents a threat to the cryosphere's equilibrium, influencing the dynamics and mass balance of glaciers, as well as the ocean's thermal and dynamical processes. All of this could result in hydrological and ecological effects at regional and global scales, including sea level rise.

Glaciers, even if they constitute only a small fraction of the total volume of two main ice sheets – Greenland and Antarctica – are currently losing more mass, and at similar or greater acceleration rates, than either of the ice sheet individually. Therefore, it is necessary to understand glaciers as a part of a complex system in which oceanic and atmospheric effects also play an important role. Tidewater glaciers are glaciers that terminate in the sea, with terminus either floating or grounded below the sea level. In these glaciers, frontal ablation is responsible for a large fraction of the mass loss. The main contributors to frontal ablation are iceberg calving and submarine melting. Calving is usually the largest contributor, however, submarine melting not only has a direct effect on the glacier front, but also can promote calving events through the changes induced in the stress field at the glacier terminus. Therefore, both calving and submarine melting processes should be jointly analysed. Among the factors influencing submarine melting, one of the most important processes is the formation of a buoyant plume due to the emergence of fresh subglacial water at the glacier grounding line.

In this study Elmer/Ice software is used to develop a 3D glacier dynamics model including calving and subglacial hydrology, coupled with a line plume model to calculate the calving front position at every time step. This model was applied to the Hansbreen–Hansbukta glacier–fjord system in southern Spitsbergen, Svalbard, where a large set of data are available for both the glacier and the fjord, from September 2008 to March 2011. It is found that the 3D model reproduced the expected seasonal cycle of advance–retreat. Besides, the modelled front positions were in good agreement with the observed front positions at the central 350 m of the calving front, with longitudinal differences, on average, below 15 metres for the period from December 2009 to March 2011. But there were regions of the front, especially the eastern margin, that presented major differences. Improving the model by refining the input surface velocities and introducing a three–zone plume, the new modelled positions reproduced better the retreat season in comparison to the previous model. Furthermore, the level of agreement between modelled and observed front positions improved, resulting not only in lower longitudinal differences – below 10 metres –, but also extending the central part of the front from 350 m to 700 m, half the total its extension. But the problem in the eastern margin persists.

Finally, a sensitivity analysis was carried out proving that the model is stable at variations in the input parameter, but also that calving is more sensitive to velocity changes, followed by to changes in the fjord ambient conditions and changes in the surface melt water.

Contents

List of Figures

Chapter 1

Introduction

The ocean plays a pivotal role in regulating climate. Around 71 % Earth's surface is covered by the global ocean. This saline water mass extends from polar to equatorial regions, contains ∼97 % of the Earth's water and supplies ∼99 % of the Earth's biologically habitable space (Pörtner et al., 2019). The average depth of the ocean is around 3700 m, and is vertically stratified in density layers from more dense water (bottom of the ocean) to less dense water (surface). The density is determined by water temperature, salinity and pressure. But water in Earth is not only present in a liquid state. Cryosphere refers to the parts of the Earth where water is frozen, and includes snow, glaciers and ice caps, ice sheets, lake and river ice, sea ice, permafrost and seasonally frozen ground. Combined, all these elements comprise ∼70 % of the total freshwater volume on Earth. Besides, their extension covers around 21 % of the Earth's surface, of which 0.15 % corresponds to glaciers (Vaughan et al., 2013).

At the ocean surface, temperature has, on average, increased by 0.88 °C between 1850–1900 and 2011–2020, and it is projected to increase between 1995 to 2014 and 2081 to 2100 on average, depending of the scenario, between 0.86 °C and 2.89°C (Masson-Delmotte et al., 2021). The ongoing climate change context exerts an impact on the dynamics and mass balance of glaciers, as well as the ocean's thermal and dynamical processes, resulting in hydrological and ecological effects at regional and global scales, including sea level rise. Despite constituting only a small fraction of the total volume of the Antarctic and Greenland ice sheets, glaciers are currently losing more mass than both sheets taken separately and are doing so at similar or greater acceleration rates (Hugonnet et al., 2021). In fact, according to the Sixth Assessment Report of the IPCC of 2021 (Masson-Delmotte et al., 2021), glaciers have contributed substantially to sea level rise from 1971 to 2018, accounting for 22 % of the total estimated contribution. The main reason for this is the high susceptibility of glaciers to atmospheric and oceanic forcing (Rignot et al., 2010; Motyka et al., 2013; Straneo and Cenedese, 2015; Luckman et al., 2015; Holmes et al., 2019). Therefore, it is necessary to understand glaciers as a part of a complex system in which oceanic and atmospheric effects also play an important role. And the development of models including all these processes will contribute to make better predictions for the future.

In this work we aim to fill some of the above gaps by presenting a 3D full–Stokes ice flow model focused on the front evolution of Hansbreen, a tidewater glacier located in the Svalbard archipelago. To do so, we include atmospheric (through surface mass balance and surface meltwater), hydrological and oceanic processes (line plume model), and a 3D calving law. We run the model for a total of 30 months, from September 2008 to March 2011, and analyse the model performance by comparing the monthly front positions obtained with observational data. By including all elements involved in frontal ablation, this model is expected to be a valuable instrument to study the terminus evolution.

1.1 Background

This section presents the state of the art of the subject. To establish some context, it starts by giving a general view about the ice distribution, the mass change rate and contribution to sea level change for the main ice–covered regions, and some future predictions under different scenarios. After that, tidewater glaciers and some factors involved in the study of this type of glaciers such as atmospheric and oceanic processes, are presented as a complex system which still requires a deeper understanding.

1.1.1 Ice masses in a global context

The Greenland Ice Sheet (GrIS) encompasses an approximate area of 1.7×10^6 km^2 and contains a volume of around 3×10^6 km^3 of ice (Morlighem et al., 2017), while the Antarctic Ice Sheet (AIS), excluding ice shelves, covers a larger area, around 12.3×10^6 km^2, and holds an approximate volume of 26.5×10^6 km^3 of ice (Fretwell et al., 2013). On the other hand, about 215000 glaciers distinct from the Greenland and Antarctic ice sheets included in the Randolph Glacier Inventory version 6.0 (RGI Consortium, 2017) cover an approximate area of 7×10^5 km^2 globally, comprising an ice volume of about 1.58×10^5 km^3 (Farinotti et al., 2019).

The GrIS experienced a mass loss of 4890 [4140–5640] Gt between 1992 and 2020, resulting in a sea level rise of 13.5 [11.4 to 15.6] mm. Projections indicate that the GrIS is likely to contribute an additional 0.06 (0.01 to 0.10) m to 0.13 (0.09 to 0.18) m of sea level rise by 2100 relative to the 1995–2014 baseline. Similarly, the AIS underwent a mass loss of 2670 [1800 to 3540] Gt over the same period, translating to a global mean sea level rise of 7.4 (5.0 to 9.8) mm. Projections suggest that the AIS is likely to contribute an additional 0.11 (0.03 to 0.27) m to 0.12 (0.03 to 0.34) m of sea level rise by 2100 relative to the 1995–2014 baseline (Masson-Delmotte et al., 2021). Between 1993 and 2019, the global glacier mass loss rate, excluding peripheral glaciers of the Greenland and Antarctic Ice Sheets, was very likely 210 ± 50 Gt yr^{-1}, accounting for 6 [4 to 8] % of the total glacier mass in 1993 (Masson-Delmotte et al., 2021). The estimated global glacier mass loss rate in the period 2000–2019 is ascended to 266 ± 16 Gt yr^{-1} when the peripheral glaciers are included, representing 4 [3 to 6] % of the total glacier mass in 2000. This rate has increased from 240 ± 9 Gt yr^{-1} in 2000–2009 to 290 ± 10 Gt yr^{-1} in 2010–2019 (Hugonnet et al., 2021). Glaciers estimated contribution to global mean sea level rise for the period 1993-2019 was 17.1 [12.7 to 21.5] mm, and the projection for 2100 is an increase between

18 [5 to 31] % and 36 [16 to 56] % (Masson-Delmotte et al., 2021).

Svalbard, in particular, is an Arctic region with a very high climatic sensitivity (Isaksen et al., 2016; Nordli et al., 2020). The entire volume of water stored in Arctic glaciers, if melted completely, could rise sea level around 0.3 m (AMAP, 2017). The mass change rate of Arctic glaciers, including Greenland's periphery, during the period from 2000 to 2018 reached -124.6 Gt a^{-1}, and represents 46.7 % of the total rate for all the glaciers around the world (Hugonnet et al., 2021). The projections for this region through the 21st century show that its contribution will be significant (Meier et al., 2007; Church et al., 2013; Hock et al., 2019) so, by the end of this period the estimated ice loss from glaciers would contribute between 3.9 and 9.2 cm to the sea level rise, around 56 % of the total glacier estimation (Edwards et al., 2021). In the case of Svalbard, the contribution to sea level rise is estimated at between 0.75 and 1.25 cm (Edwards et al., 2021).

1.1.2 Tidewater glaciers

Tidewater glaciers (Figure 1.1) are glaciers that terminate in the sea, with terminus either floating or grounded below the sea level (Cogley et al., 2011). The terminus position of these glaciers is an essential climate variable that provides insights into significant processes such as glacier mass balance and ice–ocean interactions (Bojinski et al., 2014), and frontal ablation plays a primary role in controlling the terminus position. In regions like Svalbard and the Russian Arctic, frontal ablation of tidewater glaciers accounts for between 10 and 30 % of total glacier mass loss (Huss and Hock, 2015; Hanna et al., 2020). In fact, a recent study analysing the different northern ice–covered regions Kochtitzky et al. (2022) revealed that the Russian Arctic experienced the largest frontal ablation rate between 2000 and 2020, followed by Svalbard. The principal mechanism involved in frontal ablation are, on the one hand, calving, and, on the other hand, submarine melting.

Numerous studies have focused into the evolution of tidewater glacier front positions using remote sensing data, such as e.g. Błaszczyk et al. (2021) at a local level, or e.g. Kochtitzky et al. (2022) on a more global scale. However, the relative importance of the different processes influencing front position changes remains poorly understood due to the scarcity of in situ measurements. This scarcity is particularly acute in the case of basal conditions and subglacial hydrology as a consequence of the inaccessibility. Furthermore, the heavily crevassed zone near the calving front is often an obstacle in the acquisition of measurements that could be useful in constraining processes like calving and submarine melting. Some recent works have begun to address this scarcity of direct measurements by incorporating observations and models focused in fjord water properties (Jackson et al., 2017, 2019), glacier front alterations (Vallot et al., 2019), and the entire glacier–fjord system (Cassotto et al., 2018; Jouvet et al., 2018; Sutherland et al., 2019; Xie et al., 2019). However, current understanding still relies heavily on parameterizations of melting and entrainment, for which there is limited validation available (Hewitt, 2020). In summary, many aspects of tidewater glaciers remain under–observed and poorly characterised.

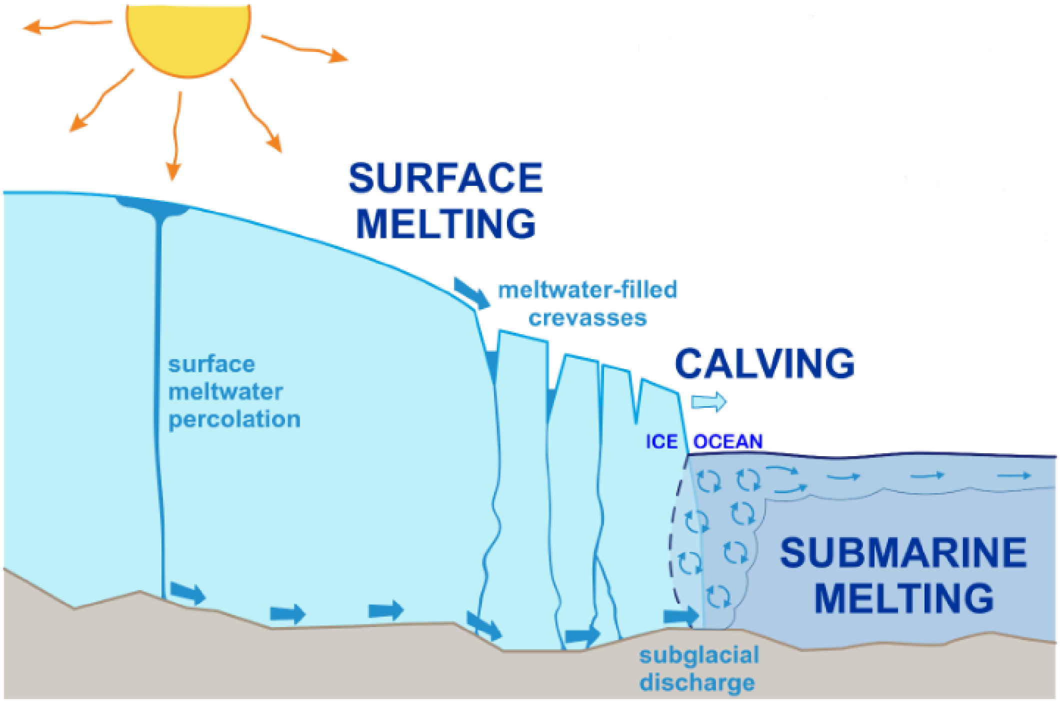

Figure 1.1: Schematic of a tidewater glacier and the main processes involved in frontal ablation (De Andrés, 2020)

1.1.3 Computational models in the context of a tidewater glacier

Computational models can help in understanding processes and predicting the future evolution of glaciers, yet they require at least a minimum of observational input data. Moreover, the more realistic and complex models require a larger variety and number of input data. In terms of calving, for example, the development of a simple calving law is still an unsolved problem (Benn et al., 2017; Benn and Åström, 2018). Therefore, the use of computationally expensive 3D calving models to reproduce the process with a fair degree of agreement with reality becomes necessary (Todd et al., 2018, 2019). In terms of submarine melting at tidewater glaciers, Jenkins (2011) implemented a one–dimensional plume model by adapting his previous work (Jenkins, 1991) based on the theory of Morton et al. (1956), finding a relation between the subglacial runoff and the submarine melt rate. This model has been used to compute submarine melting in tidewater glaciers (Cownton et al., 2015, 2019; Slater et al., 2015, 2018). Cook et al. (2020, 2022) studied both calving and subglacial melting by coupling subglacial hydrology and meltwater plumes to a 3D glacier dynamics model. These authors found significant results concerning the subglacial hydrology and its relationship with calving and plume processes, but they did not focus their work on the glacier terminus evolution. The front evolution, though, has been studied by some authors (Otero et al., 2017; De Andrés et al., 2018) using 2D models, evidencing the role of the back pressure and the importance of oceanic and atmospheric processes. Even so, the lack of the third dimension in the latter models has prevented incorporating important dynamical 3D effects, such as lateral front melting.

1.1.4 The Hansbreen–Hansbukta system

The two last–mentioned models were applied to the Hansbreen–Hansbutka glacier–fjord system, in Svalbard, which is our focus of interest, but there are not the only modelling works that refer to this system. Oerlemans et al. (2011) proposed a minimal glacier model, in which the ice mechanics was strongly parameterized. The simple law for iceberg calving used in their model was able to match observed and simulated glacier length since 1900. Vieli et al. (2000, 2002) found that basal–sliding processes strongly depend on the effective pressure and control the flow and the retreat of Hansbreen. Pętlicki et al. (2015), on the other hand, concluded that calving on Hansbreen is mainly triggered by the local imbalance of forces at the front, due to undercutting at the sea waterline and development of a thermo–erosional notch. More recently, De Andrés et al. (2021) made a comparison between a 2D glacier–fjord model and a 2D glacier–plume model regarding the calving front evolution. They determine that both models showed similar results for simulated glacier front positions under appropriate constraints of subglacial discharge, fjord temperature and crevasse water depth, but the glacier–plume model computational cost was significantly lower. Möller et al. (2023) presented a sensitivity study analysing the impact of five different bedrock datasets on projected mass losses from Hansbreen and suggested that under the influences of warmer climates accurate bedrock/ice thickness data are especially important for future glacier evolution modelling on decadal timescales. Finally, another recent study of Holmes et al. (2023) used a 3D model to study Kronebreen, a tidewater glacier in the same region – Hornsund fjord – and found that submarine melt is an important driver of seasonal variation in modelled glacier dynamics and calving activity.

1.2 Main objectives

Overall, the principal aim of this thesis is the study of the front position of a tidewater glacier by implementing a 3D model. To do so, the tasks carried out to fulfil the objectives of this work are the following:

- Building of a 3D glacier model. This dynamic model includes a series of input data such as the observed surface velocities, the geometry or the surface mass balance to simulate the ice dynamics of a real glacier during a time span.

- Solving the subglacial hydrology. Input data like surface meltwater has been included as a source term to the hydrology system. The solution of the hydrology provides a subglacial discharge, an essential variable in the study of a tidewater glacier.

- Including the front evolution into the 3D glacier dynamics model by incorporating modules to solve the two main frontal ablation processes: calving and submarine melting. To solve submarine melting a line plume model is used that receives the subglacial discharge – provided by the hydrology – and the fjord ambient conditions as inputs.

- Applying the model to a real and largely observed glacier, Hansbreen, to determine its level of performance, i.e., how good – or bad – behaves the model when contrasting with a real case. This is done by comparing the front positions of both, model and observations.

Additionally, there are some other secondary questions that this work pretend to address:

- Which, calving or submarine melting, is the primary contributor to frontal ablation?
- Which, surface meltwater of fjord ambient conditions, is the most important factor for submarine melting?
- What is the relation between submarine melting and calving activity?
- Does the inclusion of a 3D model improve the results obtained by previous 2D models?

On the whole, since atmospheric, hydrological and oceanic processes are included, as well as the main elements involved in frontal ablation – calving and submarine melting – this model is expected to be a valuable instrument to study the terminus evolution of tidewater glaciers.

Chapter 2

Methodology

This chapter addresses the methodology used for this study. It begins with a general overview of the model, which covers the following components: glacier dynamics, calving, subglacial hydrology, ice–ocean thermodynamics, submarine melting (plume model), boundary conditions, meshing, and the numerical model employed. Finally, the design of the model that was generated taking into account all of the mentioned components is explained.

2.1 Model overview

The core of this work is the development of a 3D model of a tidewater glacier to estimate frontal ablation. Since the front is in contact with a mass of water, ice–ocean interaction processes are essential in the behaviour of these glaciers. Therefore, the 3D model is composed of a central module that solves glacier dynamics, incorporating additional functionalities to address calving, subglacial hydrology, and submarine melting. To do so, the open–source, full–Stokes, finite–element, ice flow model Elmer/Ice (Gagliardini et al., 2013) is used, including the GlaDS (Glacier Drainage System) hydrological model (Werder et al., 2013) for the subglacial hydrology, a 3D calving module (Todd et al., 2018) and a continuous sheet–style line plume across the width of the calving front (Cook et al., 2020) to account for the submarine melting.

2.1.1 Ice flow model

On a long enough time scale, ice can be treated as an incompressible and extremely high–viscous fluid. This model, thus, solves the full–Stokes equations for ice flow, which consists of series of equations describing the steady conservation of linear momentum and mass conservation of an incompressible continuous medium:

$$div(\boldsymbol{\sigma}) + \rho\mathbf{g} = div(\boldsymbol{\tau}) - grad(p) + \rho\mathbf{g} = \mathbf{0} \tag{2.1}$$

$$div(\mathbf{u}) = tr(\dot{\boldsymbol{\varepsilon}}) = \mathbf{0} \tag{2.2}$$

where $\boldsymbol{\sigma}$ is the Cauchy stress tensor, $\boldsymbol{\tau}$ the deviatoric stress tensor, $\dot{\boldsymbol{\varepsilon}}$ the strain rate, $\mathbf{u}$=(u,v,w) the fluid velocity, $\mathbf{g}$=(0,0,-g) the gravity and ρ the ice density. The Cauchy stress and the deviatoric stress tensors are related following:

$$\boldsymbol{\sigma} = \boldsymbol{\tau} - p\mathbf{I} \ , \ p = -tr(\boldsymbol{\sigma})/3 \tag{2.3}$$

where $\boldsymbol{I}$ is the identity matrix. As the constitutive relation, Nye's generalisation of Glen's flow law is adopted (e.g., Cuffey and Paterson, 2010), which links the deviatoric stress and the strain rate:

$$\boldsymbol{\tau} = 2\eta\dot{\boldsymbol{\varepsilon}} \tag{2.4}$$

where the effective viscosity, η, is given by:

$$\eta = \frac{1}{2}(EA)^{-1/n}\dot{\varepsilon}_e^{(1-n)/n} \tag{2.5}$$

where $\dot{\varepsilon}_e^2 = tr(\dot{\boldsymbol{\varepsilon}}^2)/2$ is the square of the second invariant of the strain rate, E is the enhancement factor and A is a rheological parameter which follows:

$$A = A(T') = A_0 e^{-Q/RT'} \tag{2.6}$$

where T' denotes the ice temperature relative to the melting point and R the gas constant. A and Q are set following Cuffey and Paterson (2010), which establish:

$$\mathrm{A} = \begin{cases} \mathrm{A}_1 = 2.89 \times 10^{-13}\mathrm{s}^{-1}\mathrm{Pa}^{-3}, & \text{if} \quad \mathrm{T} \leq 10\text{ºC} \\ \mathrm{A}_2 = 2.89 \times 10^{-13}\mathrm{s}^{-1}\mathrm{Pa}^{-3}, & \text{if} \quad \mathrm{T} \geq \text{-10ºC} \end{cases}$$

$$\mathrm{Q} = \begin{cases} \mathrm{Q}_1 = 60 \ \mathrm{kJ\ mol}^{-1}, & \text{if} \quad \mathrm{T} \leq 10\text{ºC} \\ \mathrm{Q}_2 = 115 \ \mathrm{kJmol}^{-1}, & \text{if} \quad \mathrm{T} \geq \text{-10ºC} \end{cases}$$

assuming in this case a constant temperature of -1ºC.

2.1.2 Calving

Benn et al. (2007b) postulated that, from the different calving mechanisms contemplated in their study, longitudinal stretching in the large–scale velocity field of the glacier near the terminus would be the primary driver of calving. Therefore, the downward propagation of transverse surface crevasses near the calving front, induced by the extensional stress regime, is presumably what triggers calving (Benn et al., 2007a). The depth reached by a crevasse is determined by the balance between the longitudinal tensile strain rate tending to open the crevasse and the creep closure resulting from the ice overburden pressure (Nye and Perutz, 1957; Todd and Christoffersen, 2014). This model uses the calving implementation described by Todd et al. (2018, 2019) and Cook et al. (2020, 2022), following Otero et al. (2010) and Todd and Christoffersen

(2014). This implementation is an improved formulation of the crevasse depth (CD) calving criterion postulated by Benn et al. (2007a) and Nick et al. (2010) for use in a 3D framework. This calving criterion has been chosen because it is the one implemented in Elmer/Ice, but, when compared with other calving models such as the height–above–flotation model (HAF; Van der Veen, 1996), the fraction–above–flotation model (FAF; Vieli et al., 2001), the eigencalving model (EC; Levermann et al., 2012), the von Mises criterion (VM; Morlighem et al., 2016), and a calving relation based upon the surface stress maximum (SM; Mercenier et al., 2018), the results indicate that the crevasse depth calving model provides the best balance of high accuracy and low sensitivity to imperfect parameter calibration (Amaral et al., 2020). Moreover, a recent study of Benn et al. (2023) shows that the CD calving law reflects the glaciological controls on calving at a tidewater glacier (Sermeq Kujalleq) and exhibits considerable skill in simulating its mean position and seasonal fluctuations. Crevasse depths are, therefore, calculated following:

$$\sigma_n = 2\tau_e sgn(\tau_{xx}) - \rho_i g d + P_w \tag{2.7}$$

where σ_n is the net stress (positive for extension and negative for compression). The terms on the right–hand side represent the balance of forces: the first corresponds to the opening force of longitudinal stretching, where τ_e represents the effective stress, $\tau_e^2 = \tau_{xx}^2 + \tau_{zx}^2$ and the sign function ensures that crevasses opening is only produced under longitudinal extension; the second term corresponds to the ice overburden pressure, which leads to creep closure, where ρ_i is the ice density, g is the acceleration of gravity and d stands for the crevasses depth. P_w stands for the water pressure which contributes to opening the crevasses. This term is here considered to be zero for surface crevasses because they are capable of opening without water pressure. For basal crevasses, on the other hand, water pressure is controlled by the subglacial hydrological system and at the calving front can be expressed as:

$$P_w = (Z_{sl} - Z) \cdot \rho_w g \tag{2.8}$$

with ρ_w being the density of water at the calving front and Z the elevation with respect to sea level. Z_{sl} denotes the sea level and is set to 0 m. This improved criterion specifies calving to occur either when surface crevasses reach the waterline or when surface and basal crevasses meet, and its formulation disregards the formation of new fractures. Such a simplification is justifiable given the extensively fractured nature of ice near the calving front, leading extensional stresses primarily serve to propagate existing fractures. To determine crevasse propagation, the calving model uses a separated 2D mesh representing the frontal area of the glacier. This mesh extends 1850 m up the glacier and has a resolution of 30 m. When calving occurs, the model calculates a calving vector which is normal to the calving front and maps pre–calving to post–calving node positions. In order to maintain the mesh quality, calving events require subsequent remeshing of the main mesh.

2.1.3 Subglacial hydrology (GlaDS)

Subglacial hydrology is modelled using the GlaDS model (Werder et al., 2013). This model incorporates both inefficient distributed drainage, represented by a water sheet covering the entire glacier bed, and efficient channelized drainage, represented by a network of channels generated along the mesh element edges of the computational domain. There are three variables which describe the drainage system: the sheet thickness, h, the channel cross–section area, S, and the hydraulic potential, ϕ. The last term is defined as:

$$\phi = \rho_w g Z + P_w \tag{2.9}$$

and the set of equation describing the system is:

$$\frac{e_v}{\rho_w g}\frac{\partial \phi}{\partial t} - \nabla \cdot q + w_s - v_s - m_b = \mathbf{0} \tag{2.10}$$

$$\frac{\partial Q}{\partial s} + \frac{\Xi - \Pi}{L}(\frac{1}{\rho_i} - \frac{1}{\rho_w}) - v_c - m_c = \mathbf{0} \tag{2.11}$$

$$\frac{\partial h}{\partial t} = w_s - v_s \tag{2.12}$$

$$\frac{\partial S}{\partial t} = \frac{\Xi - \Pi}{L} - v_c \tag{2.13}$$

where e_v is the englacial void ratio which allows water storage in the sheet layer, m_b the source term, $\mathbf{q}$ the water discharge in the sheet, v_s the cavity closing rate due to creep of ice, w_s the cavity opening rate due to sliding over bumps, m_c the channel source term, Q the discharge in a channel, Ξ the potential energy dissipated per unit length of channel, Π the rate of change of sensible heat per unit length of channel due to changes in the pressure melting point, and L is the latent heat of fusion.

The implementation of the hydrological model for this work uses the GlaDS Elmer/Ice module, which has been adapted, regarding the size of the domain, following Gagliardini and Werder (2018) and Cook et al. (2020) to model Hansbreen's subglacial hydrology. The main parameters of the model are set out in Table 2.1. To avoid unnecessary complexity, GlaDS is applied at the glacier bed using the same mesh as the ice model to obtain subglacial discharge estimates at the grounding line. Water is not permitted to flow through the lateral boundaries and we set the hydraulic potential, ϕ, to zero at the grounding line. This is obtained from equation 2.8 and 2.9 combined with the definition of the hydraulic potential. Water input into the hydrological system is derived from surface and basal meltwater production. Surface melting is determined by calculating monthly averages for the surface meltwater, assuming it travels directly to the bed at the same point of production at the surface. As for basal meltwater, we

Table 2.1: Parameters used for the GlaDS model in this study

Description	Name	Value	Units
Pressure melt coefficient	c_t	$7.5\cdot 10^{-8}$	KPa^{-1}
Heat capacity of water	c_w	4220	$\mathrm{J\ kg^{-1}K^{-1}}$
Sheet flow exponent	α_s	3	
Sheet flow exponent	β_s	2	
Channel flow exponent	α_c	5/4	
Channel flow exponent	β_c	3/2	
Sheet conductivity	k_s	0.005	$\mathrm{m\ s^{-1}kg^{-1}}$
Channel conductivity	k_c	0.1	$\mathrm{m^{3/2}kg^{-1/2}}$
Sheet width below chann	l_c	0.2	m
Cavity spacing	l_r	0.5	m
Bedrock bump ratio	h_r	0.02	m
Englacial void ratio	e_v	10^{-4}	

suppose a distributed melt calculated using a geothermal heat flux of 63 mW $\mathrm{m^{-2}}$ (Gagliardini and Werder, 2018).

2.1.4 Ice–ocean thermodynamics

At an ice–ocean interface (Fig. 2.1), such as a floating ice shelf or tidewater glacier, the energy balance can be formulated as:

$$Q_a^T = Q_i^T - Q_{lat}^T \tag{2.14}$$
$$Q_a^S = Q_i^S - Q_{brine}^S \tag{2.15}$$

This means that there has to be a balance between the heat flux supplied to the glacier by the ambient fjord water, Q_a^T, and the heat flux into the ice, Q_i^T, plus the latent heat flux due to melting or freezing, Q_{lat}^T. And similarly for Q_a^S, Q_i^S, and Q_{brine}^S. This budget can be expressed in terms of the known ambient and ice properties by a set of equation following the parameterization developed by Holland and Jenkins (1999):

$$T_b = \lambda_1 S_b + \lambda_2 + \lambda_3 p_b \tag{2.16}$$
$$C_{pw}\rho\gamma_T(T_a - T_b) = -q[L_f + C_{pi}k(T_i - T_b)] \tag{2.17}$$
$$\rho\gamma_S(S_a - S_b) = -q(S_b - S_i) \tag{2.18}$$

where T_b, p_b and S_b are temperature, pressure and salinity at the boundary, the subscript a refers to ambient properties, and q the melt rate of ice. For seawater, λ_1 = -5.73 × 10^{-2} ºC is the freezing point slope; $\lambda_2 = 8.32 \times 10^{-}2$ ºC is the freezing point offset; and $\lambda_3 = 7.61 \times 10^{-4}$ºC m^{-1} is the depth–dependent freezing point slope. L$_f$ is the latent heat of fusion, C$_{pw,i}$ is the specific heat capacity for seawater and ice respectively (with values 3974 and 2000 J kg^{-1}K^{-1}), and $\gamma_{T,S}$ is the velocity–dependent turbulent transfer coefficients of heat and salt respectively.

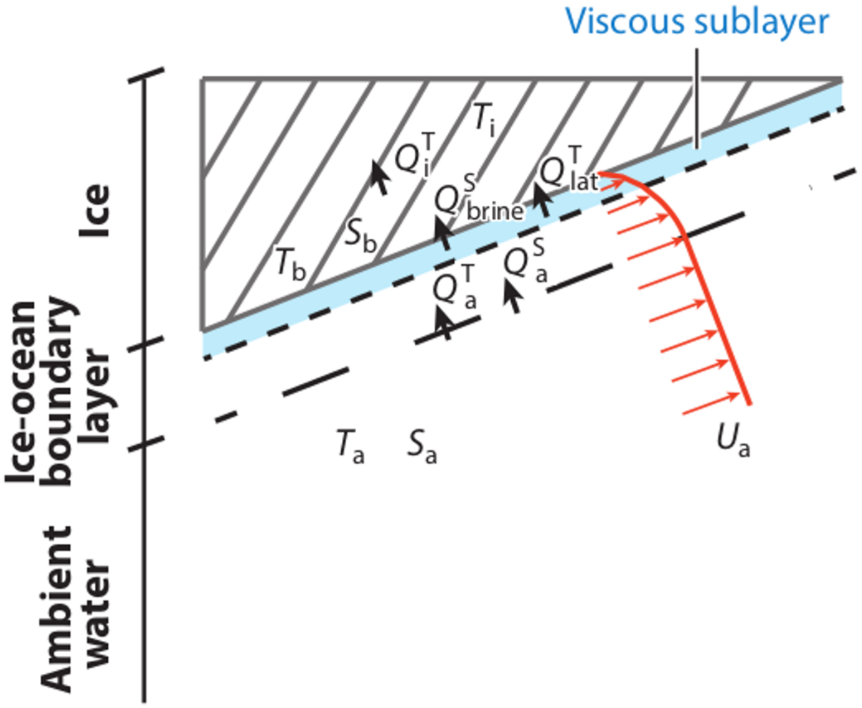

Figure 2.1: Schematic representation of heat and salt fluxes at the ice–ocean interface. S and T stand for salinity and temperature respectively, whereas subscripts b, i and a indicate boundary, ice and ambient water, respectively. Source: (Straneo and Cenedese, 2015).

Turbulent transference of heat and salt are considered proportional to the vertical velocity (U_a) near the glacier front wall, so:

$$\gamma_{T,S} = C_d^{1/2} \Gamma_{T,S} U_a \tag{2.19}$$

where $C_d^{1/2}$ and $\Gamma_{T,S}$ are the drag and turbulent–transfer coefficients, respectively.

2.1.5 Plume model

Models of ocean circulation can capture the broad–scale features of the buoyancy–driven circulation and reproduce the observed distribution of melting and freezing next to the glacier front. However, resolving all the processes that operate at the grounding line is generally beyond the capabilities of most ocean circulation models. In regions where fast–flowing tidewater glaciers terminate in fjords there will be a flow of freshwater draining across the grounding line from the glacier bed. When this water emerges, it provides buoyancy forcing for the overturning circulation in addition to that provided by melting at the ice–ocean interface. Figure 2.2 illustrates a one–dimensional model, based on the theory of buoyant plumes, developed by Jenkins (2011). The equations describing this model are as follows:

$$\frac{d}{dX}(DU) = \dot{e} + \dot{m} \tag{2.20}$$

$$\frac{d}{dX}(DU^2) = D\frac{\Delta\rho}{\rho_0}gsin\alpha - C_dU^2 \tag{2.21}$$

$$\frac{d}{dX}(DUT) = \dot{e}T_a + \dot{m}T_b - UC_d^{1/2}\Gamma_T(T - T_b) \tag{2.22}$$

$$\frac{d}{dX}(DUS) = \dot{e}S_a + \dot{m}S_b - UC_d^{1/2}\Gamma_S(S - S_b) \tag{2.23}$$

where D, U, T and S are the plume thickness, velocity, temperature and salinity respectively, α is the angle of the ice shelf base from the horizontal (in our case, $\alpha = 90^{o}$), $\dot{m}$ and $\dot{e}$ (defined as $E_0Usin\alpha$) are the melt and the entrainment rate respectively, and $C_d^{1/2}\Gamma_T$ and $C_d^{1/2}\Gamma_S$ are the thermal and haline Stanton numbers.

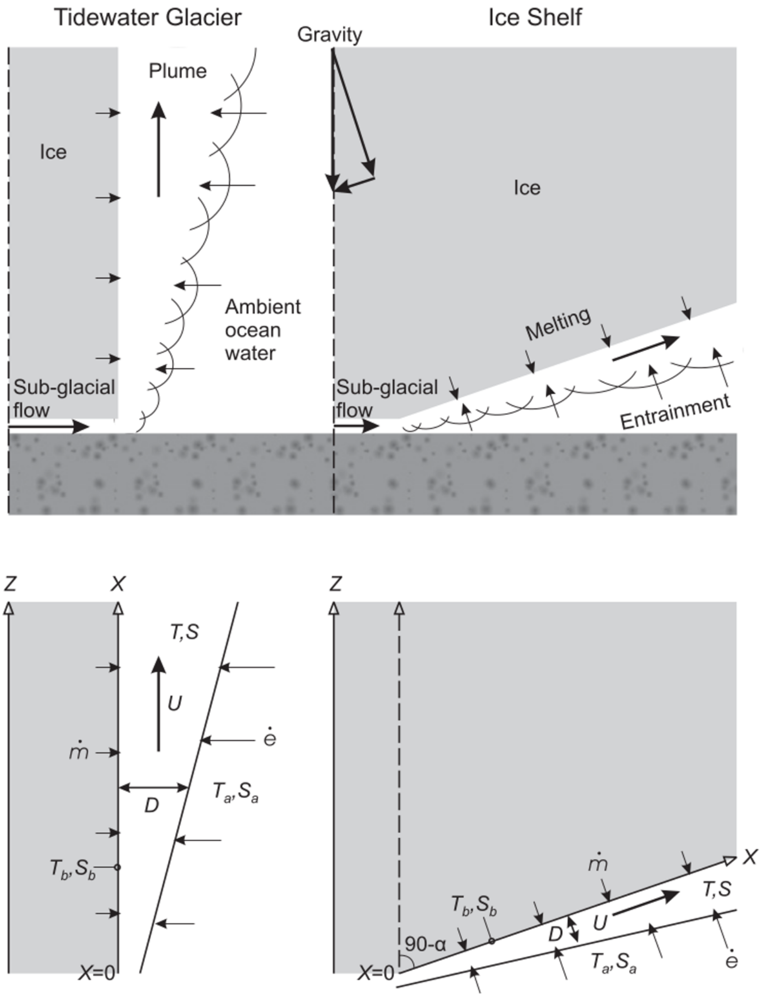

Figure 2.2: One–dimensional plume model. Source: (Jenkins, 2011).

The implementation of the plume model for this work uses the Plume Elmer/Ice module

(Cook et al., 2020, 2022) based on buoyant plume theory (Jenkins, 2011; Slater et al., 2015). In that model, a continuous sheet–style line plume, split into coterminous segments, is simulated across the calving front. The field studies carried out on tidewater glaciers (Fried et al., 2015; Jackson et al., 2017) justify the selection of this plume geometry.

The plume model is initialised using the subglacial discharge values at each node of the grounding line, which are obtained by solving the subglacial hydrology model. The buoyancy flux generated by the density difference between meltwater and fjord ambient water causes subglacial discharge water to ascend adjacent to the calving front, while it turbulently mixes with the surrounding water, inducing melting at the ice–water interface. The calculated melt rates are subsequently employed to modify the geometry of the submerged part of the calving front.

2.1.6 Boundary conditions

The calving front is determined by a series of nodes between two fixed points in the lateral margins of the glacier. Consequently, these nodes will be the ones that are allowed to advance and retreat. At the head of the glacier, the ice divide, horizontal velocities and shear stresses are set to zero. No flow is allowed through the lateral margins of the glacier, where no–slip conditions are additionally imposed. The upper free–surface is constrained to a surface mass balance accumulation flux boundary condition (positive for accumulation, negative for ablation). This flux is obtained by calculating monthly means of the SMB data described in Chapter 3:

$$\frac{\partial z_S}{\partial t} + u_S \frac{\partial z_S}{\partial x} + v_S \frac{\partial z_S}{\partial y} - w_S = a_s \tag{2.24}$$

where u_S, v_S and w_S are the surface velocities obtained from the Stokes solution and a_s accounts for the surface mass balance. As for the lower boundary, assuming that ice flows over hard bedrock at Hansbreen glacier, a simple Weertman–type sliding law is applied at the bed:

$$\tau_b = \beta u_b \tag{2.25}$$

where τ_b is the basal stress, u_b is the basal velocity and β is the slip coefficient. The Weertman–type sliding law has been chosen assuming that ice flows over hard bedrock at Hansbreen. Finally, a seawater hydrostatic pressure condition is imposed at the front of the glacier.

2.1.7 Meshing

The 3D mesh is built by vertically extruding the footprint of the glacier, an horizontal mesh composed of triangles. The footprint has been designed to have a maximum resolution of 50 m at the calving front. The resolution decreases progressively up glacier, reaching 200 m at 5 km from the front and, beyond that, the mesh continues coarsening to get to 500 m at the head of the glacier (Fig. 2.3). This horizontal mesh is then vertically extruded on 10 levels, resulting in a 3D mesh composed of triangular prisms (Fig. 2.4).

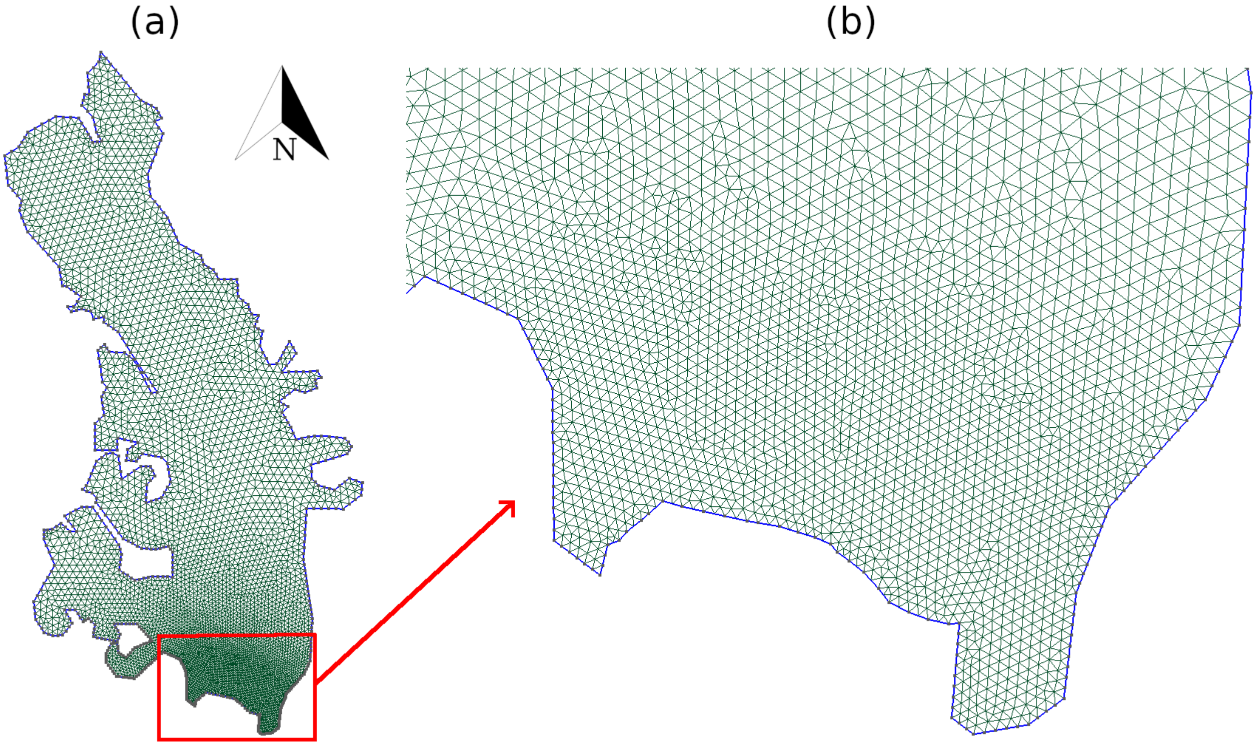

Figure 2.3: (a) Two–dimensional mesh representing the footprint of the glacier, and (b) detail of the area next to the calving front.

2.1.8 Numeric model: Elmer/Ice

Elmer/Ice is an open source finite–element software for ice sheet, glaciers and ice flow modelling. It has been used on more than 200 scientific publications and applied to a range of different problems such as full–Stokes equations for different ice rheologies, Shallow Ice Approximation (SIA) and Shallow Shelf Approximation (SSA), grounding line dynamics, age of ice, various friction laws, among others. The general functioning of Elmer/Ice can be summarised using the flowchart presented in Fig. 2.5. The main solver (ElmerSolver) needs a mesh file and a configuration file. The mesh file is obtained using the tool ElmerGrid, which requires a preprocessed input file describing the mesh (obtained by using the software Gmsh). The configuration file specifies a series of properties, the modules (solvers) to be executed, and the boundary conditions of the problem. Upon completion of the simulation, ElmerSolver can generate various output files, including an ASCII file containing the values of the selected variables, a VTU file for visualising the results using an external tool (Paraview), or files for internal use (.result).

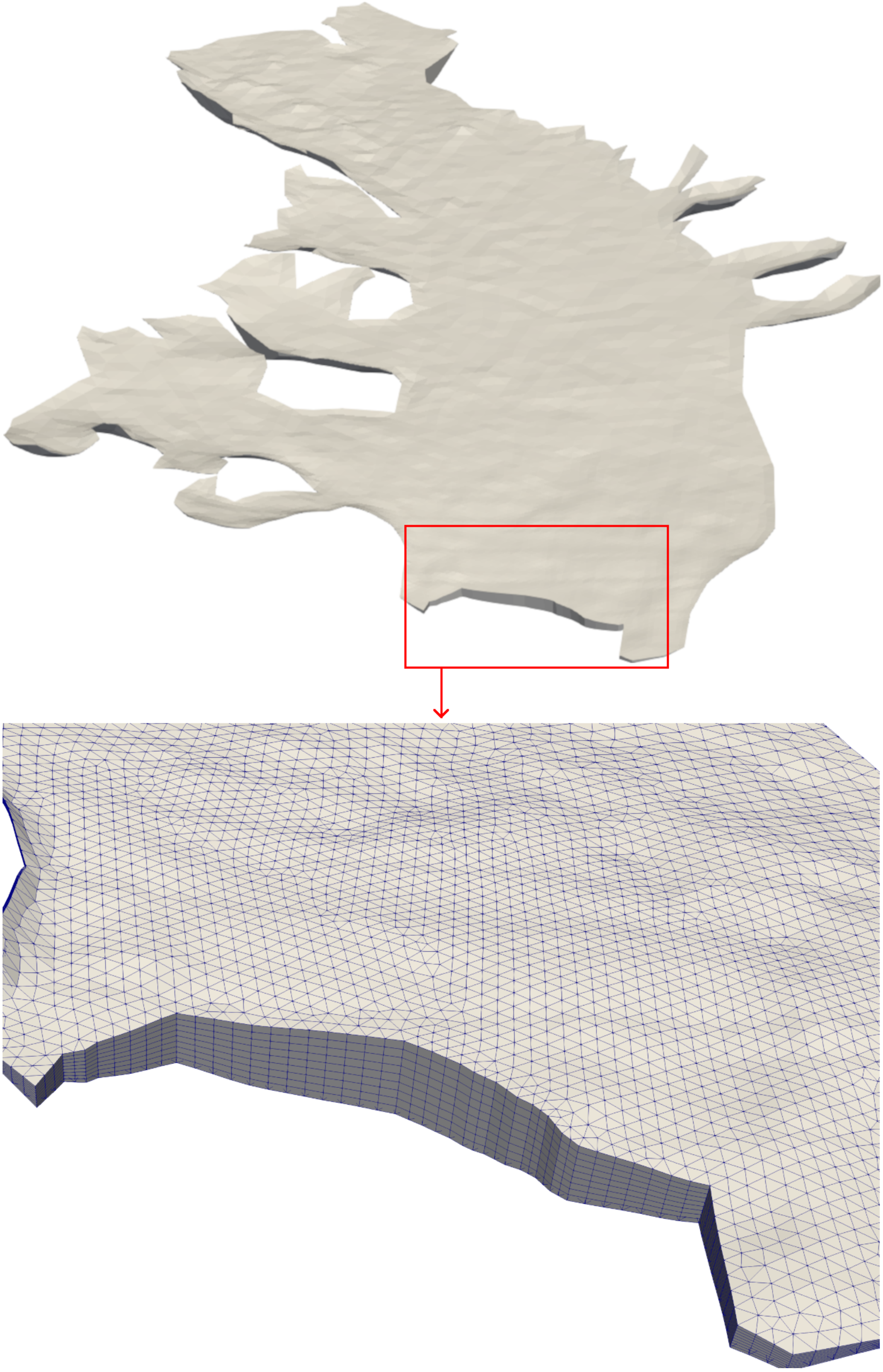

Figure 2.4: Three–dimensional mesh and detail of the front representing the geometry of the glacier.

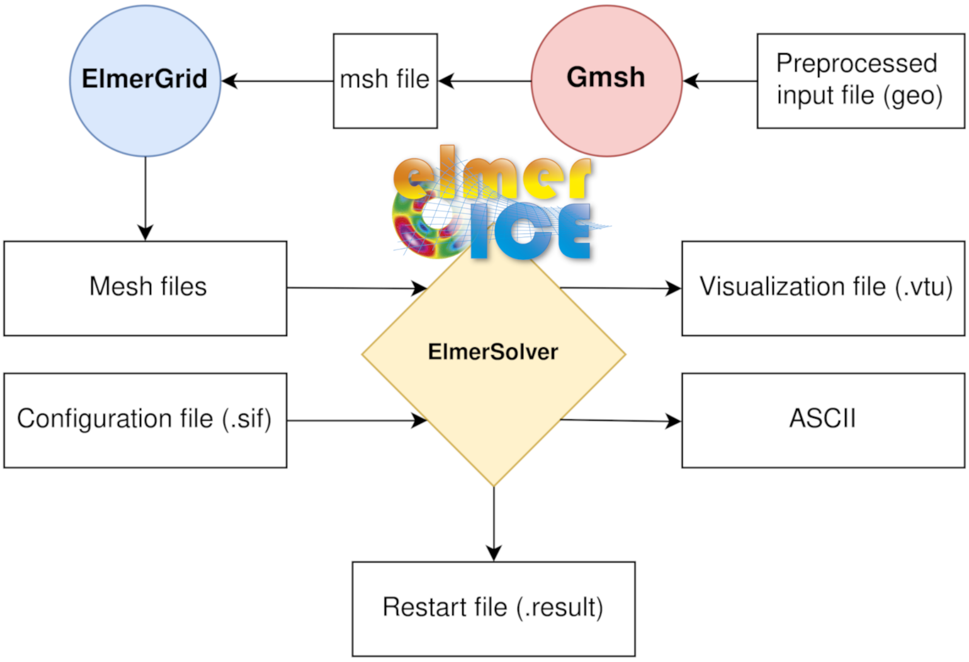

Figure 2.5: Schematics of the general functioning of Elmer/Ice.

2.2 Model Design

The model is implemented in 30–day monthly cycles with a 1–day time step that are run sequentially to cover the total time, September 2008 to March 2011. The starting date, September 2008, has been chosen taking into account the availability of an appropriate surface DEM of Hansbreen and the overlap between the different input data. The first 6 months is considered to be the initialization of the model. Therefore, the period of study extends from March 2009 to March 2011. Beyond that, there are no velocity data available. Every cycle is divided into three different steps (Fig. 2.6), as follows.

1. *Inversion for slip coefficient.* An inversion using adjoint methods (Gillet-Chaulet et al., 2012) is performed to adjust the slip coefficient to the changing mean velocities for a given month. This is done by minimising a cost function for the velocities, running monthly steady–state simulations. It is performed monthly to account for the changes in the velocity field while keeping a reasonable computational cost.

2. *Dynamical and hydrological models, and free–surface evolution.* Using the slip coefficient from the inversion, and the input surface mass balance and surface meltwater data, the hydrology is computed in a 30–day transient simulation with a 1–day time step. Subsequently, the daily subglacial discharge values are averaged over the month. At this point, the glacier surface is left to evolve freely, whereas the front remains fixed.

3. *Calving and plume models' activation.* The monthly–averaged values of subglacial discharge and the fjord ambient conditions are the required input for the line plume model. The dynamic model is run again for a month with a 1–day time step, but now with the modules for calving and plume enabled. In this case, the hydrology is not computed, the glacier

surface is left to evolve freely and the front is allowed to evolve as a combination of ice flow, submarine melting and calving. Therefore, each of these time steps results in a new glacier geometry and a new front position. To avoid mesh degeneration that could cause critical problems to the model, remeshing is performed either when calving occurs or after eight consecutive no–calving time steps.

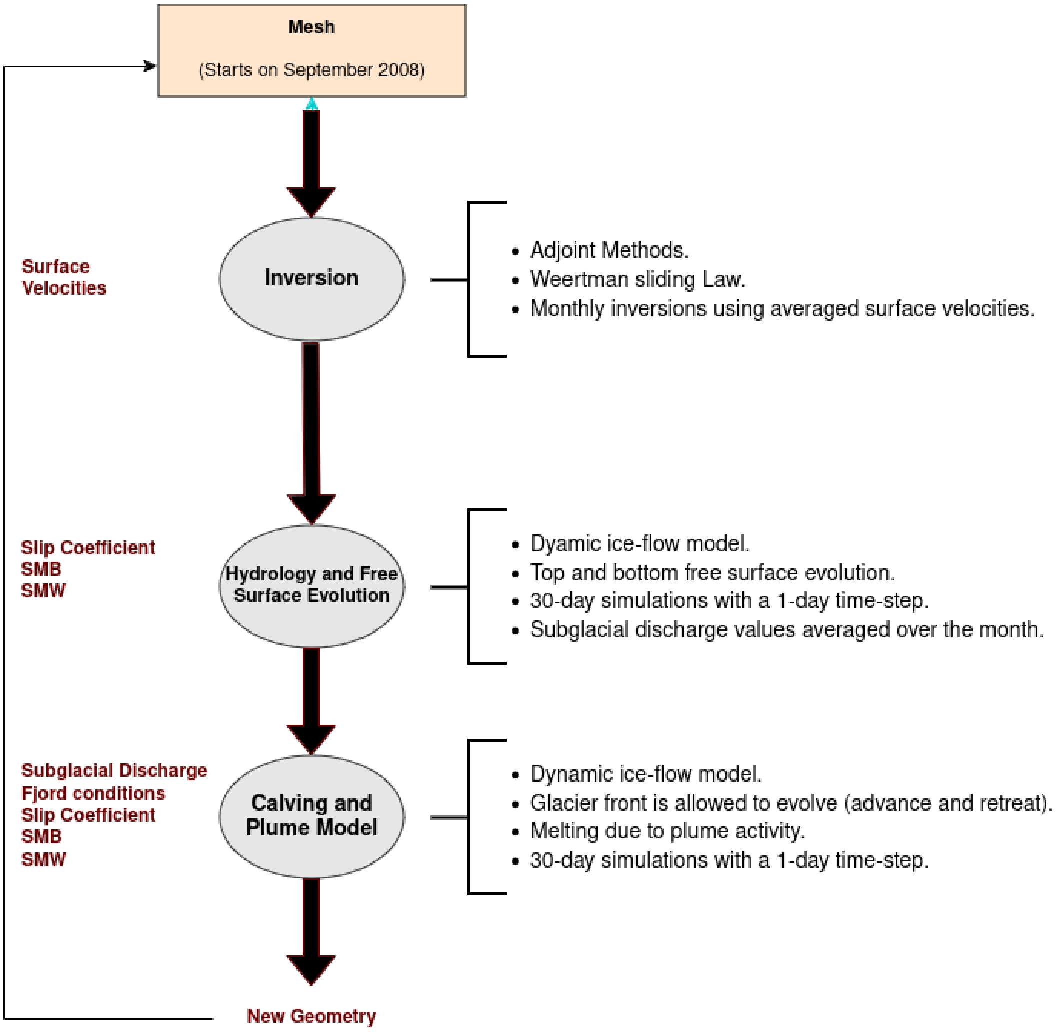

Figure 2.6: Schematics of the three–step model procedure: inversion, dynamic model with hydrology module, and dynamic model with calving and plume modules. The red arrow indicates that a series of N cycles are run to cover the total simulation period.

The initial mesh, corresponding to September 2008, is obtained from the geometry data described in Sect. 3.2.3. After every cycle, the model generates a new geometry that will be used as the input of the following one. Therefore, the model provides monthly front positions.

Chapter 3

Data and Study Area

This chapter starts with the description of the area of study, the Hansbreen–Hansbukta glacier–fjord system located in the Hornsund fjord, Svalbard. Next, the chapter details the data used as input to the model, such as velocities, mass balance, surface meltwater and fjord ambient conditions. Finally, the observed front positions used to evaluate the model's performance are presented.

3.1 Study area

Figure 3.1: Image of Hansbreen front taken on September 2023.

The glacier–fjord system Hansbreen–Hansbukta is located in one of the branches of the Hornsund fjord in southwest Spitsbergen, Svalbard, at ∼77ºN, ∼15.5ºE (Fig. 3.4). The entire drainage basin area of Hornsund amounts to ∼1200 km^2, of which ∼67% is covered by glaciers (Fig. 3.3). And tidewater glaciers constitute 97 % of the glacierized area (Błaszczyk et al., 2013).

Hansbreen is a polythermal tidewater glacier flowing in a southerly direction which covers an area of 57 km^2. It's about 16 km long with a very low mean surface slope, 1.8° along the central flow–line (Grabiec et al., 2012), and its calving front is 1.5 km wide with a vertical face 100 m thick approximately at the central flow–line, of which 50 to 60 m is below sea level. The

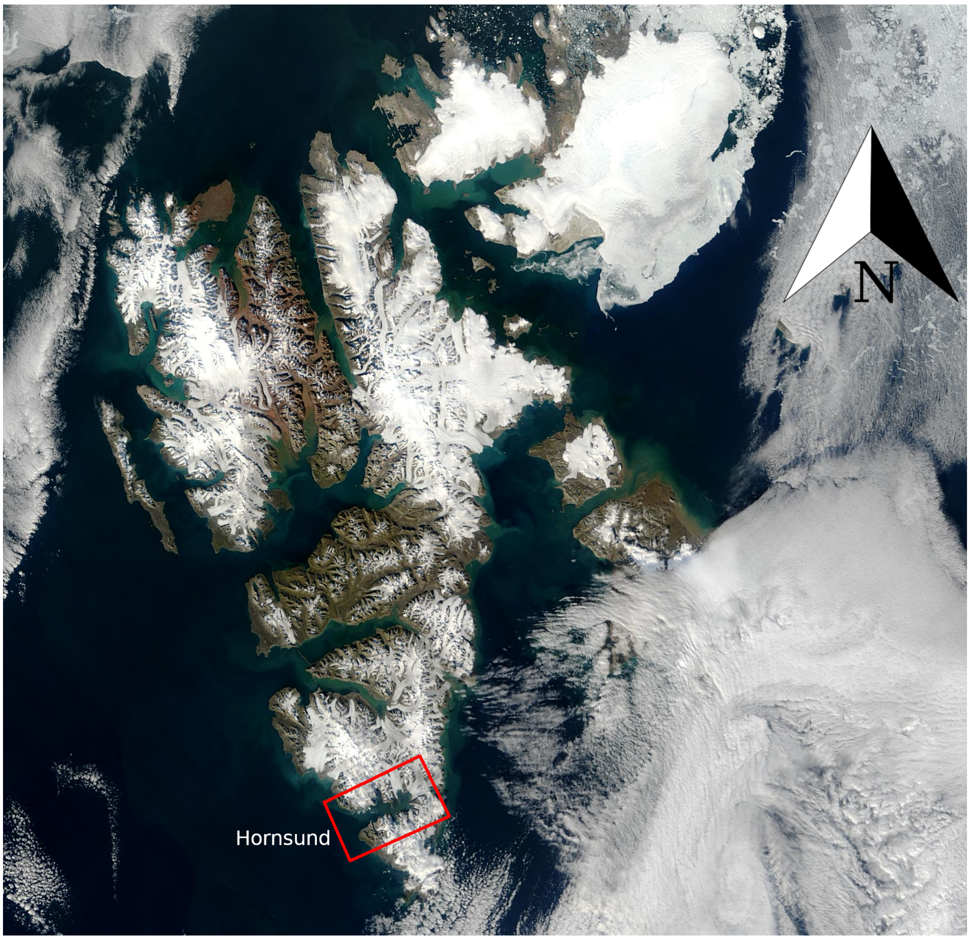

Figure 3.2: Satellite image of Svalbard. Retrieved from the Visible Earth (EOS Project Science Office at NASA Goddard Space Flight Center) website(EROS (USGS), 2013). The red box indicates the position of Hornsund fjord.

seasonal retreat of Hansbreen usually starts in June/July and lasts until late autumn/early winter, and the average summer and winter fluctuations amount to -125 and 79 m, respectively (Błaszczyk et al., 2021). As for Hansbukta, it's a ∼2 km long fjord, with maximum depth of ∼55–57 m next to the central part of the glacier front. Temperature and salinity in Hansbukta experience strong seasonal variability, ranging from -1.8 to 3°C and from 34.6 to 31.8 PSU between April and August, respectively.

3.2 Data

The data used by the model is divided into the input data – surface velocities, mass balance, surface meltwater, geometry, and oceanographic data – and the data used to validate the model – observed front positions.

3.2.1 Surface velocities

The model needs monthly surface velocities maps. Taking this into account, ice surface velocities were obtained by applying Bayesian kriging techniques (Perez-Doña and Otero, 2023) (Fig. 3.5).

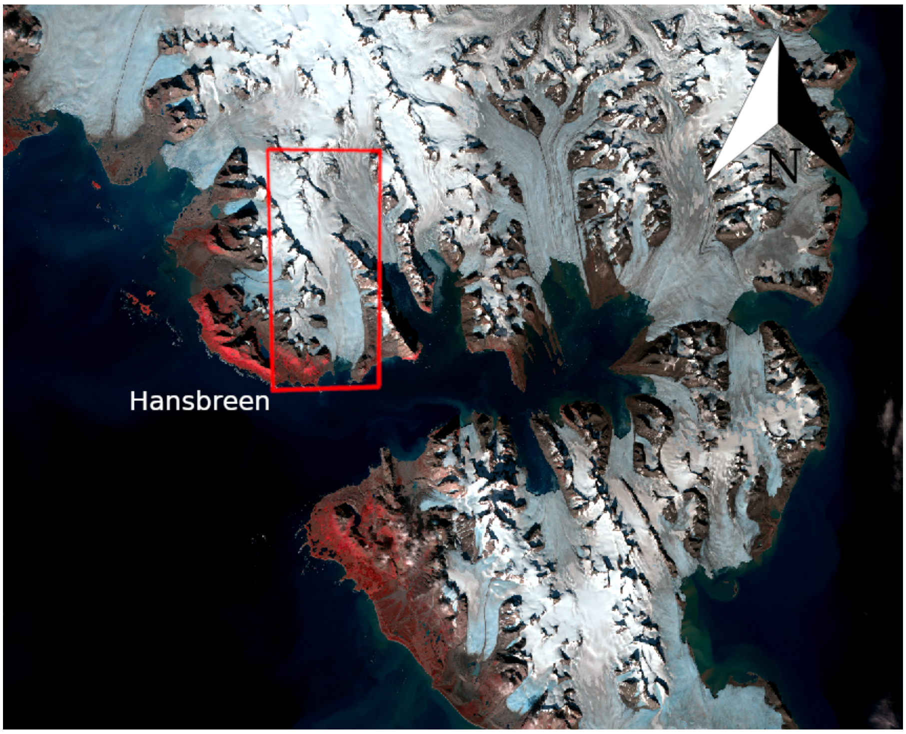

Figure 3.3: Satellite image of Hornsund. Retrieved from the USGS Earth Resources Observation and Science (EROS) Center website (Jacques Descloitres, MODIS Rapid Response Team, NASA/GSFC, 2003). The red box indicates the position of Hansbreen.

This involved using daily measurements of horizontal velocities between May 2005 and April 2011 at various locations across the glacier. As a prior, a map of the surface velocity module of Hansbreen Glacier was calculated as the mean of velocities derived from measurements taken by TerraSAR-X from January 2013 to August 2014 using feature tracking (Adrian Luckman, personal communication (September 2014)).

3.2.2 Mass balance and surface meltwater

Surface mass balance (SMB) and surface meltwater (SMW) were obtained from European Arctic Reanalysis data, with 2 km horizontal resolution and hourly temporal resolution, constrained by automatic weather stations and stake observations (Finkelnburg, 2013) (Fig. 3.6 and 3.7).

3.2.3 Geometry and topography

The surface elevation came from the SPIRIT digital elevation model for gentle slopes, with a 30 m rms absolute horizontal precision and 40 m resolution and corresponds to September 2008 (Korona et al., 2009). Bedrock topography was inferred from ground–penetrating radar data (Grabiec et al., 2012; Navarro et al., 2014). Together these data provide the geometry of glacier (Fig. 3.8).

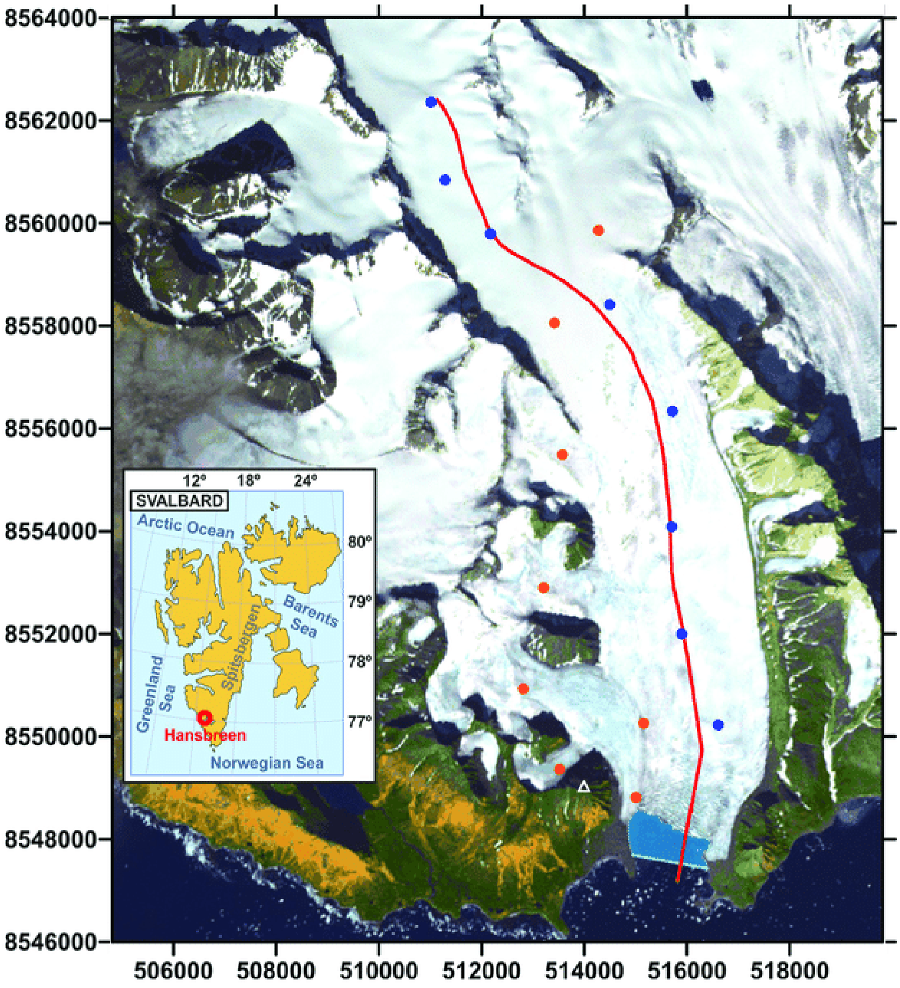

Figure 3.4: Location of Hansbreen–Hansbukta, Svalbard (inset). ASTER image of Hansbreen–Hansbukta showing the location of the stakes for velocity measurements (blue circles for the flow–line and red circles for the rest of the stakes) (Otero et al., 2017). The white triangle indicates the position of the time–lapse camera. The axes include the UTM coordinates (m) for zone 33X.

3.2.4 Oceanographic data

Oceanographic data consist on a set of CTD casts (i.e., conductivity, temperature and depth profiles) in Hansbukta (yellow points in Fig. 3.9). All the data were vertically averaged every 1 dbar (1 kPa). Available CTD oceanographic data only cover the period from April 2010 to August 2010, with a long gap between April and July. Therefore, to extend this data throughout the entire year, a combination of linear interpolation and linear extrapolation techniques was employed. Linear interpolation was used to fill in the period from April 2010 to July 2010, while a linear extrapolation was applied for the remaining months, supported by a set of mooring measurements (De Andrés et al., 2018, their 'Supplementary material').

The mooring data indicated that the temperature and salinity records remained relatively stable between November and April. Consequently, a linear extrapolation was used to calculate the values from August to November. Finally, and assuming that no changes in ambient conditions occurred between November and April, the values for November were used for the following months until March (Fig 3.10).

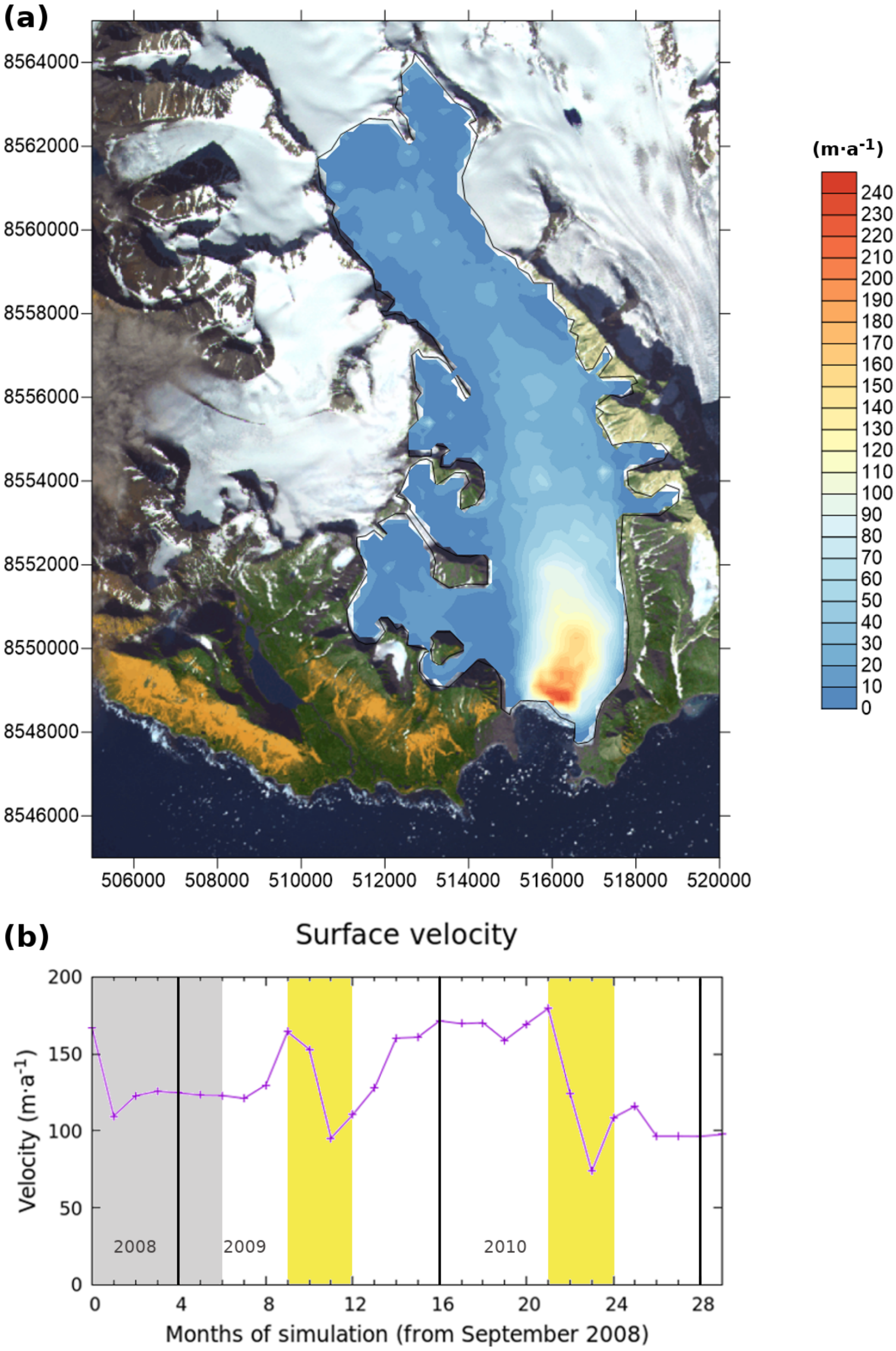

Figure 3.5: (a) Hansbreen surface velocity distribution obtained from the BK algorithm corresponding to September 2008, and (b) time evolution of the velocity at the stake located closer to the calving front (the southernmost blue point in Fig. 3.4). The shaded area corresponds to the initialization period. The yellow areas indicate the summer periods and the vertical black lines separate the different years. The satellite image used as background in (a) was available from ASTER © METI and NASA, all rights reserved, courtesy of the University of Silesia, Poland, within the frame of cooperation of the SvalGlac project.

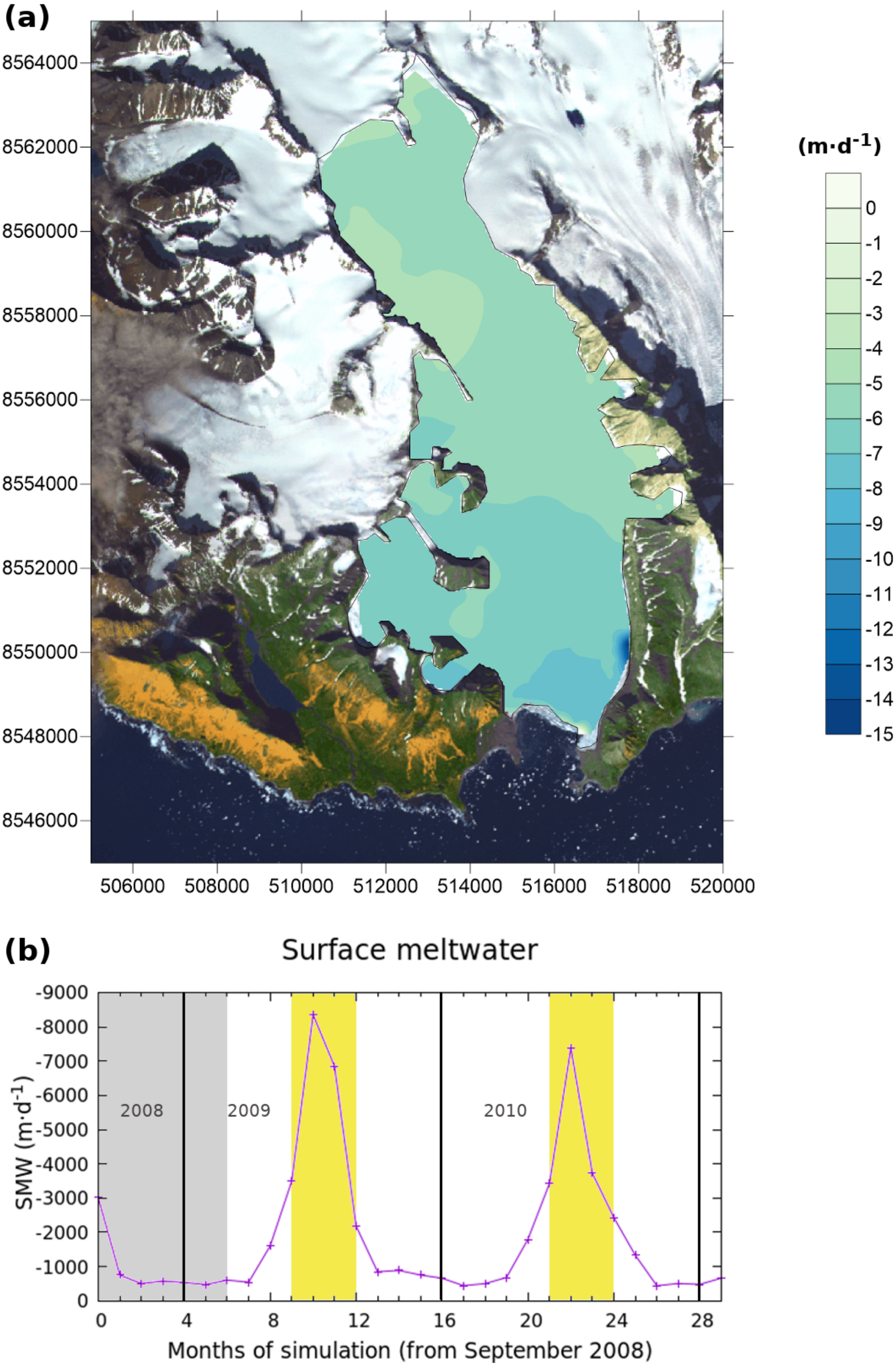

Figure 3.6: (a) Average surface meltwater (SMW) distribution corresponding to September 2008, and (b) evolution of the average surface meltwater for every month. The shaded area corresponds to the initialization period. The yellow areas indicate the summer periods and the vertical black lines separate the different years. The satellite image used as background in (a) was available from ASTER © METI and NASA, all rights reserved, courtesy of the University of Silesia, Poland, within the frame of cooperation of the SvalGlac project.

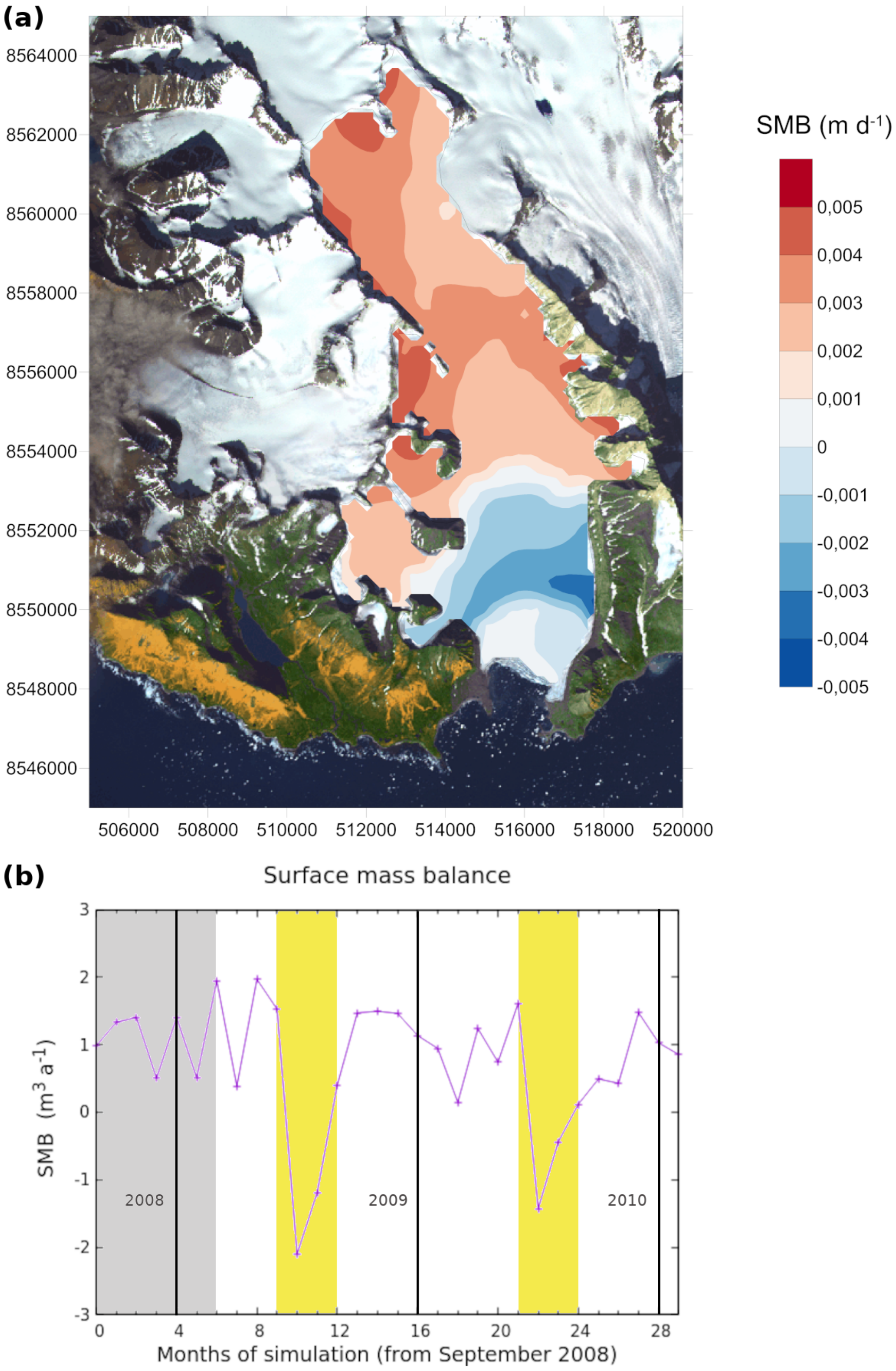

Figure 3.7: (a) Average surface mass balance (SMB) distribution corresponding to September 2008, and (b) evolution of the average surface mass balance for every month. The shaded area corresponds to the initialization period. The yellow areas indicate the summer periods and the vertical black lines separate the different years. The satellite image used as background in (a) was available from ASTER © METI and NASA, all rights reserved, courtesy of the University of Silesia, Poland, within the frame of cooperation of the SvalGlac project.

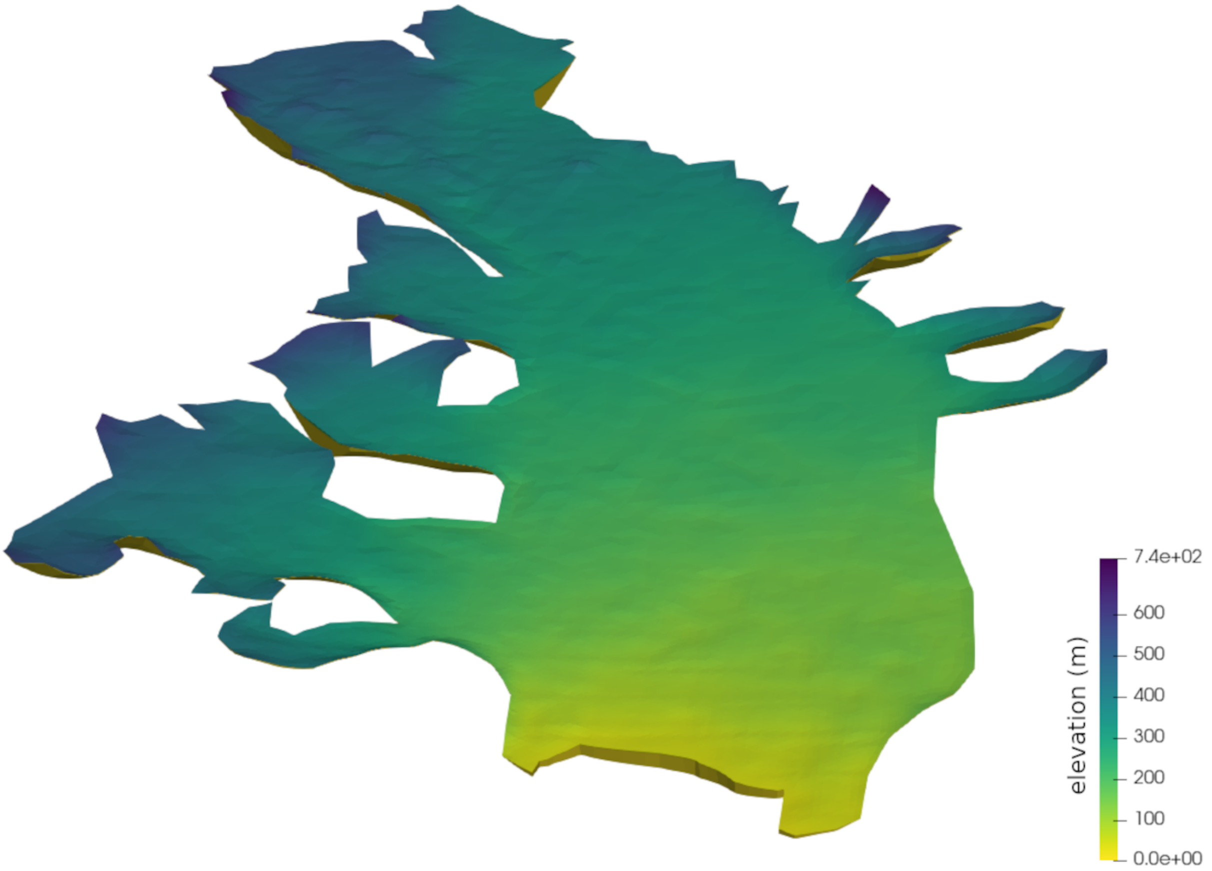

Figure 3.8: 3D representation of Hansbreen topography

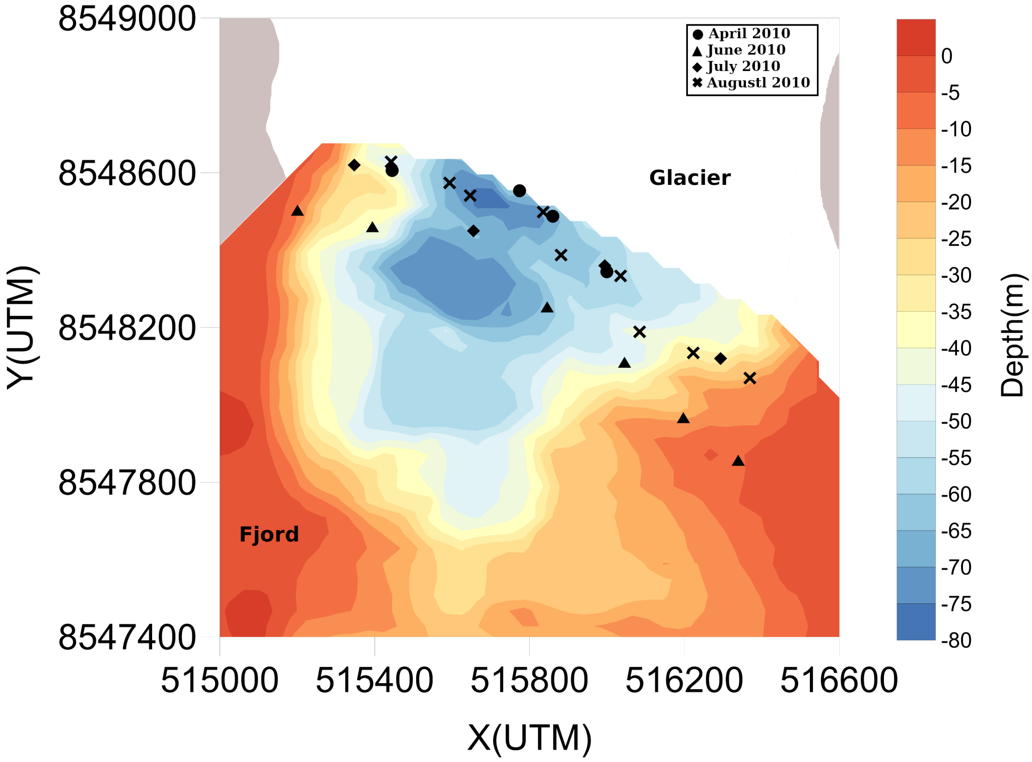

Figure 3.9: Bathymetry of Hansbukta. The symbols indicate the CTD casts distribution measured in different dates during the period April to August 2010.

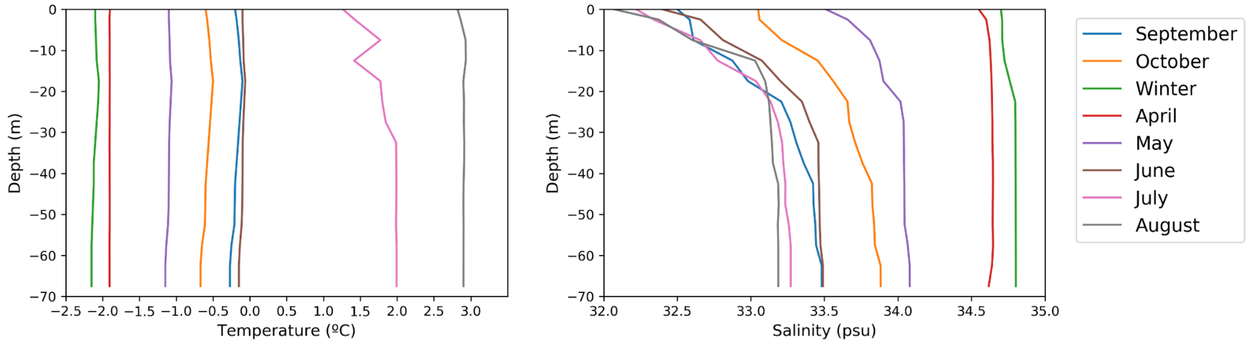

Figure 3.10: Temperature and salinity profiles in the central part of Hansbukta closest to Hansbreen calving front. Winter values cover from November to March.

3.2.5 Front positions

Front position data from time–lapse camera images taken every 3 hours were processed and averaged over weekly intervals between December 2009 and September 2011 (Otero et al., 2017). There is a lack of data in the western part of the glacier (Fig. 3.11), but the extension of the observed front is long enough to make a good comparison.

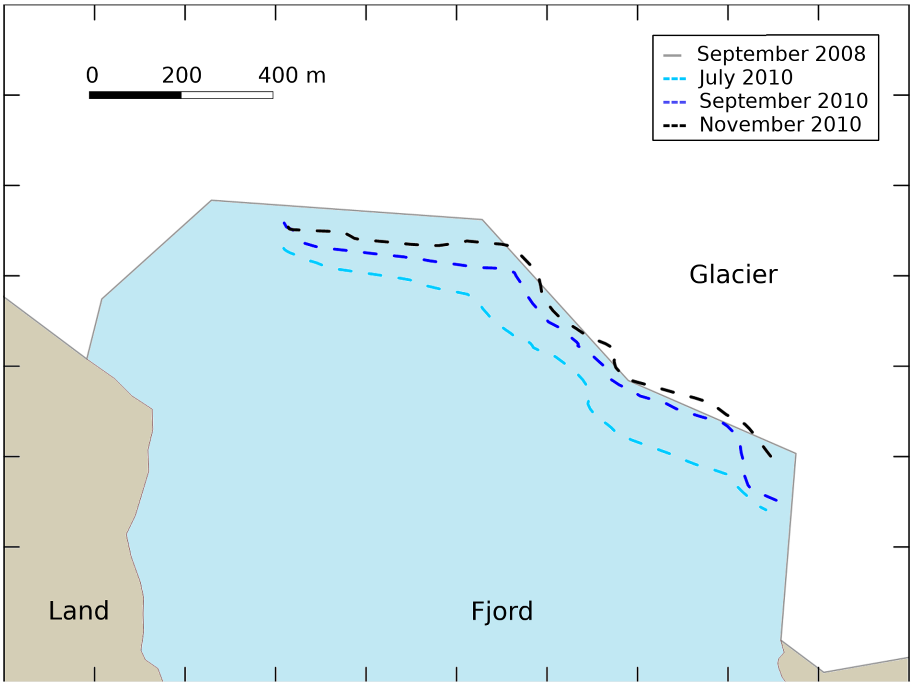

Figure 3.11: An example of some observed front positions. The grey solid line corresponds to the initial geometry, September 2008. The dashed lines correspond to July, September and November 2010.

Chapter 4

Application of the 3D Glacier Dynamics–line Plume Model to Hansbreen, Svalbard

In this work we aim to fill some of the gaps in the current state of the art mentioned in Chapter 1 by presenting a 3D full–Stokes Elmer/Ice–based ice flow model focused on Hansbreen front evolution. To do so, we include atmospheric (through surface mass balance and surface meltwater), hydrological and oceanic processes (line plume model), and a 3D calving law. We run the model for a total of 30 months, from September 2008 to March 2011, and analyse the model performance by comparing the monthly front positions obtained with observational data. By including all elements involved in frontal ablation, this model is expected to be a valuable instrument to study the terminus evolution.

This chapter includes, therefore, the results of the 3D glacier dynamics–line plume model described in Chapter 2 applied to the Hansbreen–Hansbukta system described in Chapter 3. The results are followed by a discussion of the main outputs of the model, and, finally, some conclusions of the application of the model are commented.

4.1 Results

Starting in March 2009, after an initialization period of four months, the modelled monthly values of surface meltwater, subglacial discharge, the plume melt rate, and calving volume exhibit a strong seasonality (Fig. 4.1). The largest SMW values are reached in July (8.9×10^5 m^3 a^{-1} and 8.3×10^5 m^3 a^{-1} for 2009 and 2010 respectively), and the cumulative SMW for both summer seasons is of the same order of magnitude, with the value for 2010 being ∼6 % lower than the one for 2009 (Fig. 4.1(a)). Subglacial discharge follows a similar seasonal pattern, with the largest values occurring in July (9.1×10^5 m^3 a^{-1} and 5.7×10^5 m^3 a^{-1} for 2009 and 2010 respectively). However, the total amount for both summer seasons presents substantial variations, by ∼25 % (Fig. 4.1(c)). Beyond the summer months, both SMW and subglacial discharge maintain a baseline value around 1×10^5 m^3 a^{-1}.

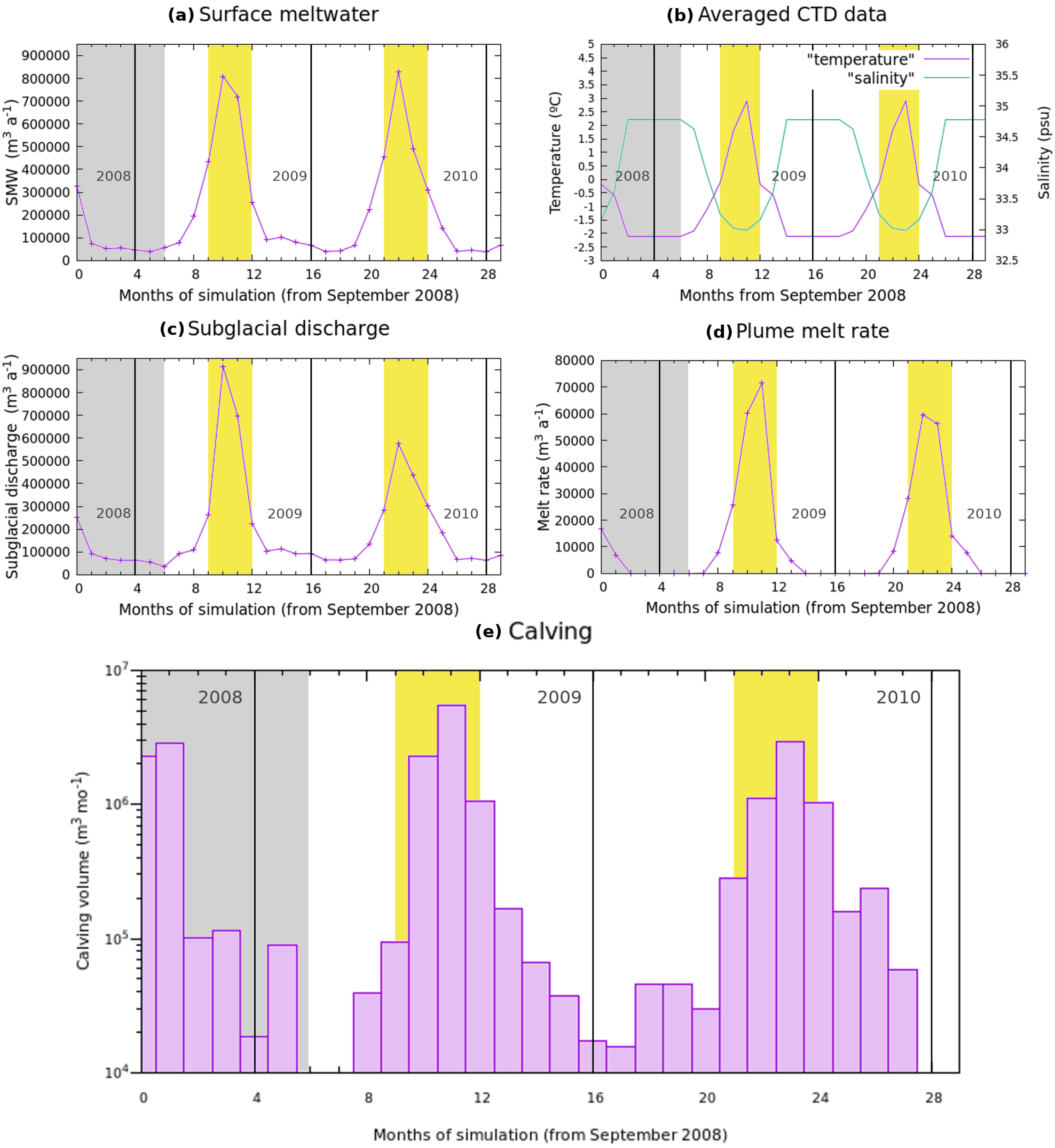

Figure 4.1: Temporal evolution of the (a) surface meltwater (SMW), (b) average temperature and salinity of the fjord water near the calving front, (c) subglacial discharge produced by surface and basal melt, (d) total melt rate produced by plume activity computed on the first day of every month and (e) calving volume produced by the model for every month of the simulation (log scale). The shaded areas correspond to the initialization period. The yellow areas indicate the summer periods and the vertical black lines separate the different years.

The total melt rate due to plume activity exhibits a difference of ∼6 % between the two summer seasons (1.7×10^5 m^3 a^{-1} and 1.6×10^5 m^3 a^{-1} for 2009 and 2010 respectively). The peak plume melt rates for each summer period occur in different months, August for 2009 (7.1×10^4 m^3 a^{-1}) and July for 2010 (5.9×10^4 m^3 a^{-1}) (Fig. 4.1(d)). Beyond these peak months, June exhibits values of around 2.6×10^4 m^3 a^{-1} and September exhibits values of around 1.3×10^4 m^3 a^{-1}. It is noteworthy that no plume melt rate is produced from November to April, since no plumes are formed during these months.

Calving volume also presents a pronounced seasonal pattern, with the highest values concentrated in the summer months(Fig. 4.1(e)). The total calving volume during the first summer is

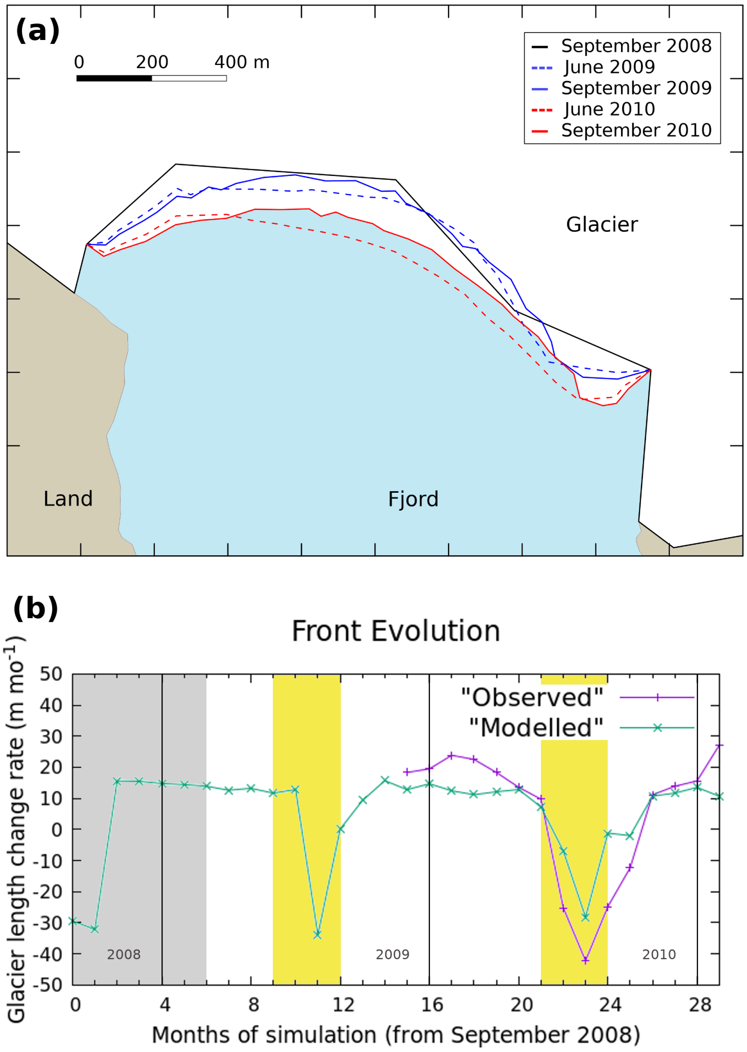

Figure 4.2: Calving front evolution. (a) The different positions represent the interannual evolution and the summer evolution of the calving front: the solid lines correspond to September 2008 (black), September 2009 (blue) and September 2010 (red), whereas the dashed lines correspond to June 2009 (blue) and June 2010 (red). (b) The graph represents the longitudinal difference along the whole simulation, calculated as the difference in area between subsequent months divided by the glacier width. The shaded area corresponds to the initialization period. The yellow areas indicate the summer periods, and the vertical black lines separate the different years.

considerably larger than during the second one, 8.89 × 10^6 m^3 per month versus 5.41 × 10^6 m^3 per month. The monthly distribution of calving volume within each summer season displays some similarities: August is the month with the largest calving volume, 5.47 × 10^6 m^3 per month for 2009 and 2.97 × 10^6 m^3 per month for 2010; July comes in second with 2.28 × 10^6 m^3 per month for 2009 and 1.12 × 10^6 m^3 per month for 2010, representing nearly half the volume of August in both cases; September exhibits values of around 1 × 10^6 m^3 per month in 2009 and 2010, while June presents the lowest values. The summer periods concentrate a significant portion, around 94 %, of the calving volume (1.43 × 10^7 m^3 per month out of 1.52 × 10^7 m^3 per month). However, calving occurs throughout the entire simulation period except for in 4 months. Outside of the summer period, autumn months like October and November exhibit moderate calving activity.

The calving front follows a seasonal pattern in terms of advance and retreat throughout the whole simulation period, generally retreating in summer and advancing during the rest of the year (Fig. 4.2 (b)). The periods of advance are longer and the advancing rate ranges from 10 m per month to 20 m per month of longitudinal difference, calculated as the difference in area between subsequent months divided by the glacier width. On the other hand, the periods of retreat are shorter and the retreating rate can reach up to -30 m per month. The most significant negative values, indicating retreat, occur in August of both 2009 and 2010. The total advance is larger during the first year (March 2009-2010), 129.35 m per month, than in the second one (March 2010-2011), 89.98 m per month. As for cumulative retreat, in the first year amounts to -33.94 m per month, whereas in the second one it is -38.23 m per month (Fig. 4.2 (a)). By the end of the first year of simulation, March 2010, the front position has advanced 95.42 m per month with respect to the position in March 2009, while by the end of the second year of simulation, March 2011, the front position has advanced 51.74 m per month with respect to March 2010, resulting in a total advance of 147.16 m per month with respect to March 2009.

4.2 Discussion

The results of the model indicate that the glacier presents a strong seasonal behaviour. This characteristic exemplifies not only in the model outputs, but also within the input data (Figures 4.3, 4.1(a) and (b)). Subglacial discharge values correlate with surface meltwater values (Fig. 4.1(a), (c)). A constant value of basal and internal melting ($\sim 2.6 \times 10^4$ m^3 a^{-1}) has been applied using the geothermal heat flux defined in Sect. 2.1.3, which, along with some other processes like internal refreezing, explains why in some months the subglacial discharge is larger than the SMW. A 6 % decrease in SMW in summer 2010 was responsible for the 25 % decrease in subglacial discharge for the same period. However, this reduction in subglacial discharge cannot be solely attributed to the decrease in SMW. A potential explanation for this discrepancy would be a change in the efficiency of the drainage system that is not being captured by the model. This change would be consistent with the pronounced decrease in the velocity values at the beginning of summer 2010 (Fig. 4.3(b)).

The plume melt rate is influenced by both fjord ambient conditions within the fjord and subglacial discharge. While the model calculates non–zero freshwater flux into the fjord in winter months (Fig. 4.1(c)), in agreement with Cook et al. (2020), in the present study, however, either the subglacial discharge values are not high enough or the winter ambient conditions are not suitable for the occurrence of plumes, unlike in the work of Cook et al. (2020) (Fig. 4.1(d)). This is a limitation of the model seeing as plumes have been observed at Hansbukta in winter. On the other hand, between April and October, both ambient conditions and subglacial discharge values are suitable for the occurrence of plumes. The ambient conditions in the fjord were kept the same for both summer periods. Hence, the differences in plume melt rate between the summers can be explained by the differences in the subglacial discharge that feeds the plumes. As an exemplification, Fig. 4.4 shows two different distributions of the plume melt rate at the calving front: a high–melting month, August 2009 (panel a) and a low–melting month, October

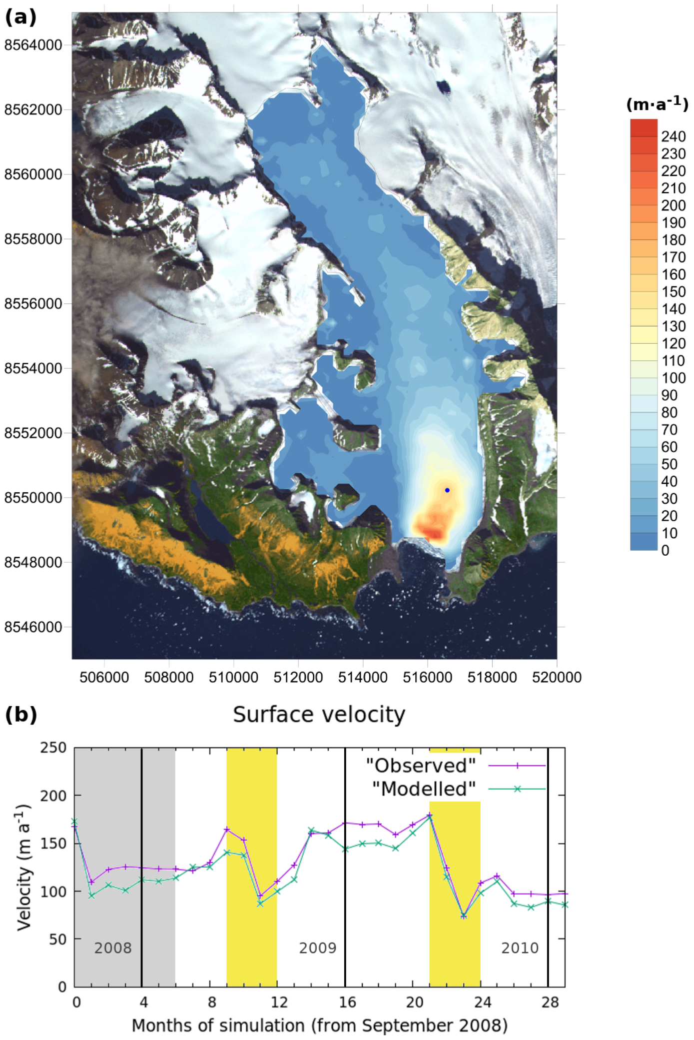

Figure 4.3: (a) Hansbreen surface velocity distribution obtained from the BK algorithm corresponding to September 2008, and (b) time evolution of the velocity at the stake located closer to the calving front (the southernmost blue point in Fig. 3.4 The shaded area corresponds to the initialization period. The yellow areas indicate the summer periods and the vertical black lines separate the different years. The satellite image used as background in (a) was available from ASTER © METI and NASA, all rights reserved, courtesy of the University of Silesia, Poland, within the frame of cooperation of the SvalGlac project.

2009 (panel b). Not only is the plume melt rate in August 2009 higher than the plume melt rate in October 2009, but also the melt extends to a larger area of the calving front. Comparing with other authors working on the same glacier–fjord system, the maximum melt rate values obtained for August 2010 are consistent with the ones obtained by De Andrés et al. (2018) (58 m^3 per month versus 64.28 m^3 per month (15 m^3 per week)).

The total amount of calving volume during the first year of simulation is significantly larger than during the second one, 9.24×10^6 m^3 per month versus 5.98×10^6 m^3 per month. This result aligns with the higher values of the plume melt rate during the first year, especially in August. However, the model results are not conclusive enough to establish a definitive quantitative relationship between plume melt rate and calving volume. For example, the plume melt rate in June 2010 is only slightly higher than that of June 2009, while the calving volume in June 2010 is more than twice that of June 2009. In September, however, a similar difference

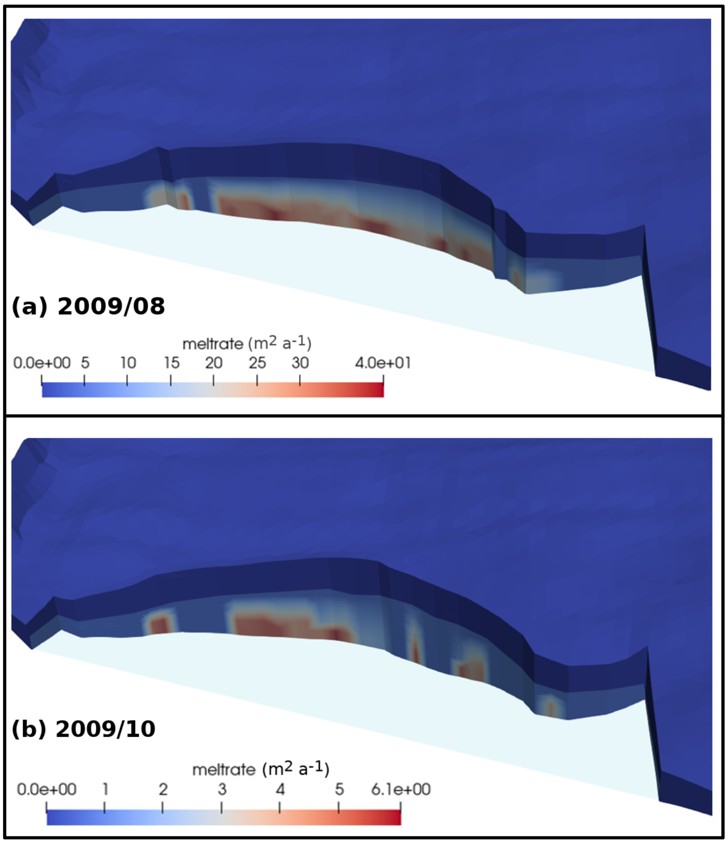

Figure 4.4: A 3D aerial view of the glacier calving front for (a) August 2009 and (b) October 2009. The red zones represent high values of the melt rate due to plume activity, although the scales used are not the same. Different scales have been chosen to account for the significant differences between the values.

in plume melt rate (i.e., the melt rate in September 2010 is only slightly higher than that of September 2009) results in calving volumes of the same order of magnitude for both months ($\sim 1 \times 10^6$ m^3 per month). Even so, in general, there is a clear correspondence between plume activity and calving, with the most intense plume activity consistently associated with the highest calving rates.

Figure 4.2 provides valuable insights into the calving front evolution and its resemblance to the expected behavior of a tidewater glacier. In general, the model provides a pattern consistent with observations: the glacier advances steadily during winter months with minimal calving activity, followed by retreat during summer months, reaching the largest retreat values in August (Fig. 4.2(b)). However, both the advance and the retreat of the calving front are being underestimated. A possible explanation for the advance underestimation would be the fact that the modelled velocities are generally lower than the observed ones (Fig. 4.3(b)). Conversely, calving underestimation is very likely to be the most important factor contributing to the retreat dissimilarities. Calving is the main contributor to frontal ablation, but plume–induced melting can lead to a larger number of calving events, so both factors are important in the control of the front position. Finally, the glacier front remains quite stable during the study period (Fig. 4.2(a)). In fact, it shows a small advance between September 2008 and 2010, in agreement with Błaszczyk et al. (2021).

To assess model performance, a comparison of the modelled and observed front positions is

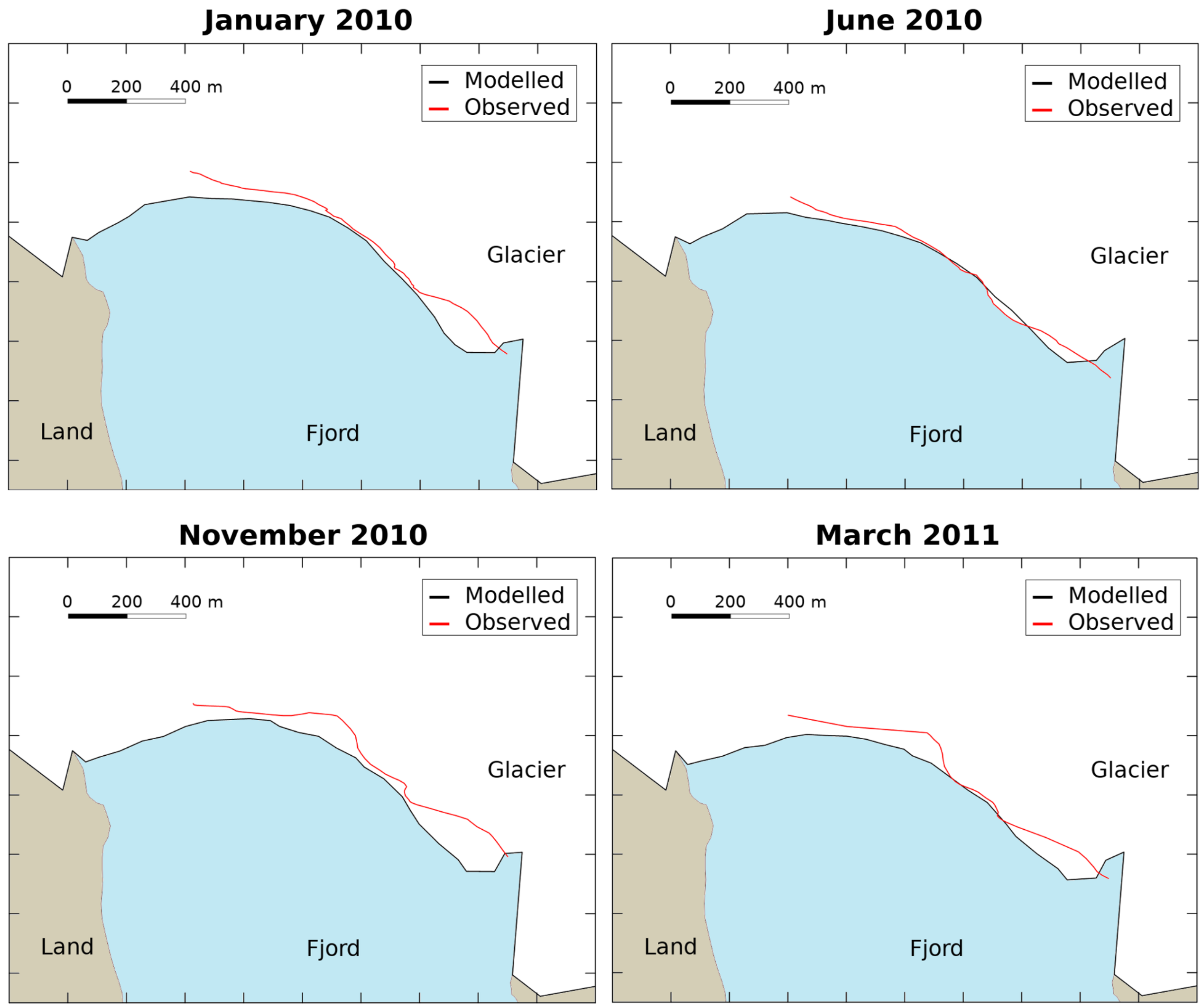

Figure 4.5: A 2D aerial view of the glacier–fjord system for January 2010, June 2010, November 2010 and March 2011. The solid black lines represent the modelled contour of the glacier, and the red lines represent the observed front position. Note that the observational data do not cover the westernmost part of the front.

conducted (Fig. 4.5). The modelled front generally exhibits a more advanced position compared to observations. The difference between modelled and observed positions varies throughout the simulation. It starts with a decreasing period from December 2009 to July 2010. Afterwards, there is an increasing period from August 2010 to November 2010, followed by a final decrease until the end of the simulation in March 2011 (Fig. 4.6). While a potential seasonal pattern is suggested by these observations, the lack of data beyond March 2011 limits our ability to definitively establish this. The results present a marked contrast between the central part and the east lateral margin of the glacier front. The maximum discrepancies in the eastern zone are approximately ten times larger than those observed in the central region. This is likely due to the lack of calving events produced by the model in that region of the glacier front that could be caused by low plume–induced melting in the area. Overall, the performance of the model is better when looking at only the central 350 m of the calving front. On average, the modelled positions are 40 % closer to the observed positions when taking just this central part (13.03 m versus 20.95 m for the total front), with half of the values below 10 m. Even so, in late

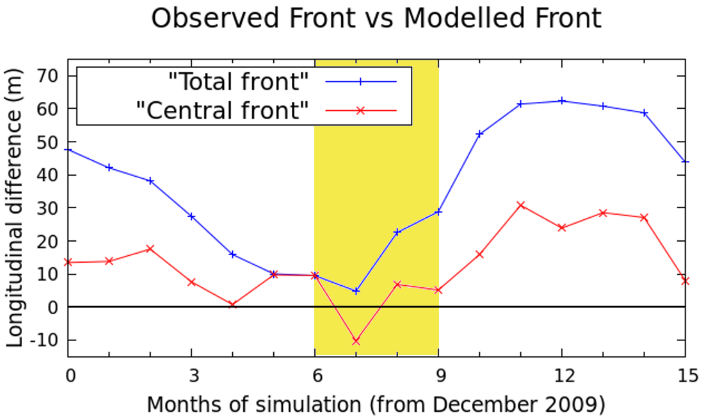

Figure 4.6: Evolution of the longitudinal difference between the modelled and the observed front position calculated as the difference in area between them divided by the glacier width (blue line), and that same evolution restricted to the central 350 m of the calving front (red line). Positive values indicate that the modelled front is more advanced than the observed one, while negative values indicate the opposite. The zero is marked with a horizontal black line so values closer to that line indicate a better agreement between modelled and observed positions. The yellow area indicates the summer period (June to September 2010).

spring and early summer, the differences in both cases, taking the whole calving front or just the central part, are considerably small and of the same order of magnitude.

Although a comparison between a 2D and a 3D model must be handled carefully, our results show a deviation of ±10 m for the central 350 m of the calving front between April and August 2010, which is consistent with the value obtained by De Andrés et al. (2018) for their 2D flow line model. To obtain those results, their model required a non–dimensional adjustable parameter used to parameterize the crevasse water depths (CWDs). In contrast, our model uses the 3D calving implementation of Todd et al. (2018), which ignores this process, so we do not need any CWD parameterization. Therefore, the inclusion of an across–glacier dimension extends the best results of the 2D model to the central 350 m of the calving front, where the 3D model predicts the observed front position with a good level of agreement. However, there is a region where the modelled positions are clearly behind the observed ones. The escalation of the difference coincides with months of higher calving activity at the glacier. A likely explanation, once again, would be an underestimation of calving events by the model. Potential reasons for this underestimation include the model's inability to capture all calving events occurring at the glacier, and an underestimation of submarine melting, since higher melt rates can enhance calving. Therefore, these two factors have to be closely examined in order to improve the performance of the model.

4.3 Conclusions

Calving and frontal ablation are essential processes to take into account in our understanding of tidewater glacier dynamics. We have developed a 3D glacier dynamics model that, in addition to solve calving and subglacial hydrology, accounts for oceanic (by a plume model) and atmospheric (by surface mass balance and surface meltwater) factors too. Subglacial hydrology provides discharge values that, in combination with appropriate fjord ambient conditions, are high enough to generate plumes at the calving front except for during the coldest months, i.e. from November to April. The results for the hydrology are consistent with other studies using a similar model (Cook et al., 2020), while the results for the plume melt rate are in agreement with other works on the Hansbreen–Hansbukta glacier–fjord system (De Andrés et al., 2018).

The model is able to predict the evolution of the front position in terms of advance and retreat following a seasonal cycle with steep retreats in summer months and steady advances during the rest of the year. However, there are still differences between observed and modelled positions, especially in the eastern margin, where the longitudinal difference reaches 150 m in November 2010. In fact, when taking only the central part of the glacier front, the results improve significantly and the modelled positions become, on average, 40 % closer to the observed ones. In general, the difference between the modelled and observed front positions increases during the calving period, and we assume that the cause is an underestimation of calving by our model. Even so, the difference between the modelled and observed front positions decreases in some months, such as May, June, and July. In these months, the model is able to predict the front position with a very good level of agreement. In the eastern margin, our model does not produce enough calving events, which causes that large differences. The timescale of this model is limited by the available data. We cannot say whether a longer simulation will result in a better agreement with observations, however, it would give us information on some results of the model that we cannot currently confirm. For example, do the differences in the eastern margin continue to increase or do they start to compensate at some point? As the results seem to suggest, is there a seasonality in the differences, such that they grow during the calving period and then decrease until reaching a minimum at the end of spring?

Changes in SMW alone are not able to explain plume behaviour, turning fjord ambient conditions into a key factor in this process. Additionally, plume–induced melting has proven to be an essential factor for calving to occur. Consequently, a logical next step would be to use a fjord model to obtain better estimates of ambient conditions. Surface velocity calculation could also be reviewed in order to address the underestimation of the glacier change length rate during the periods of advance.

4.4 Supplementary figures

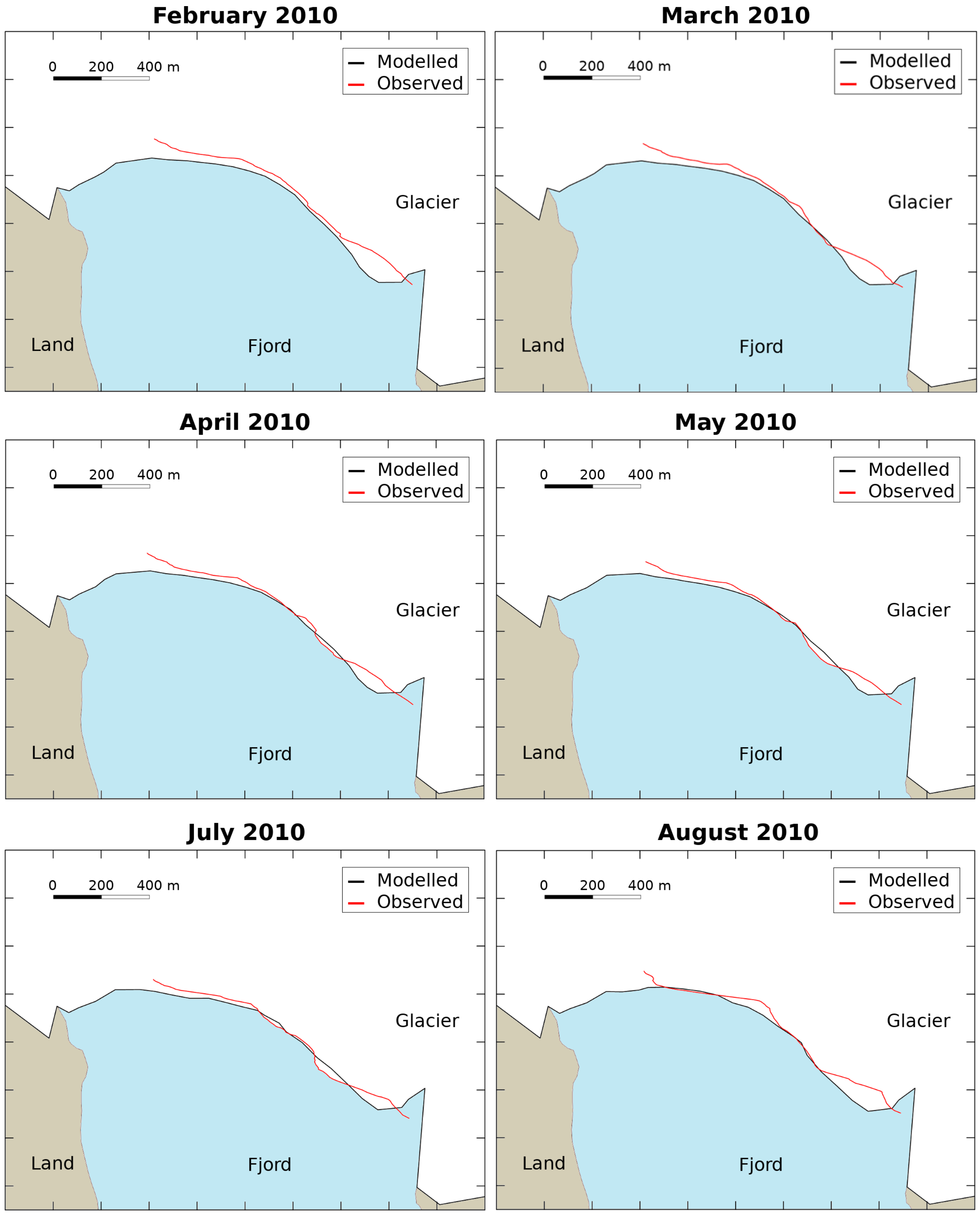

Figure 4.7: 2D aerial view of the glacier-fjord system for the rest of the months not presented in the Chapter. The solid black lines represent the modelled contour of the glacier and the red lines, the observed front position. Note that the observational data do not cover the westernmost part of the front.

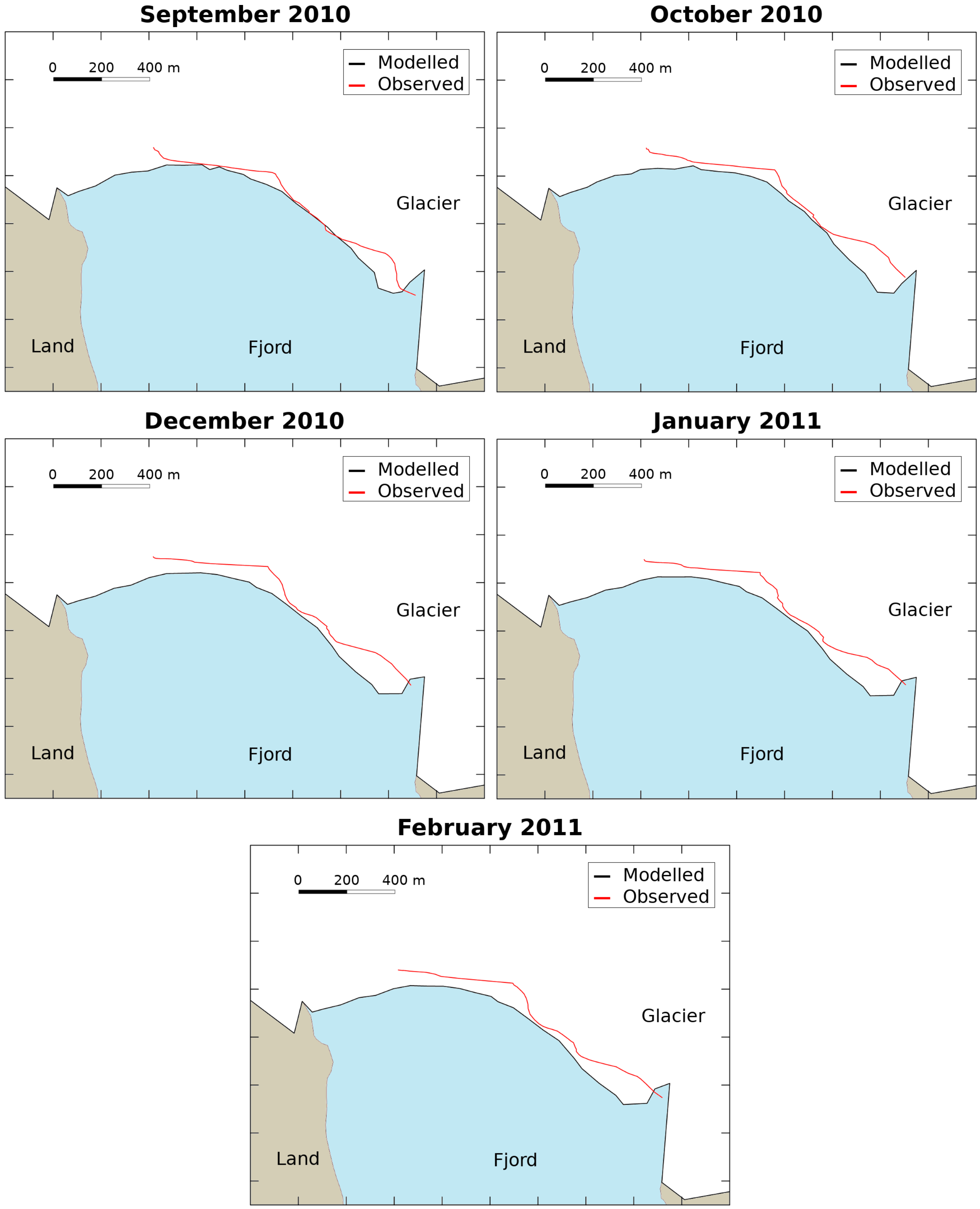

Figure 4.8: 2D aerial view of the glacier-fjord system for the rest of the months not presented in the Chapter. The solid black lines represent the modelled contour of the glacier and the red lines, the observed front position. Note that the observational data do not cover the westernmost part of the front.

Chapter 5

Model Refinement

This chapter starts by analysing the main problems of the model presented in the previous Chapter (Chapter 4, followed by an analysis of the oceanographic data and the input velocities. Then, two experiments are proposed to improve the model and both simulations are run: Experiment 1, a three–zone plume implementation, and Experiment 2, in which the front is extended one node further east. The results of Experiment 1 are discussed and compared with the results of Model 1. The results of Experiment 2, on the other hand, are not used to compare its results but to whether the front positions in the eastern margin are improved or not.

5.1 Towards and improved model

Following the results and the limitations of the 3D model presented in the last chapter, there are some options that have to be explored in order to improve the model performance. On the one hand, an analysis of the oceanographic data will be done in order to study the lack of calving during some months, and, therefore, the underestimation of the retreat. On the other hand, a refinement of the modelled velocities obtained through the inversions will be done in order to address the underestimation of the front advance.

5.1.1 Analysis of oceanographic data

Developing a 3D model to study in detail the fjord dynamics is beyond the scope of this work. The oceanic effect on the glacier front, thus, is carried out using the plume model, a simplification of the oceanic processes occurring next to the glacier front. The plume model requires the subglacial discharge and the environmental conditions of the fjord as input data to calculate the submarine melting.

In the model presented in Chapter 4, the values for the central part of the fjord were applied to the entire across–fjord direction because the model was only able to take a single temperature and salinity profile. In order to improve that approximation, it is necessary to carry out an analysis of the fjord ambient conditions – temperature and salinity profiles – in the across fjord direction, in which only the CTD closer to the calving front are taken into account (Fig. 5.1(a)).

Focusing on August 2010, a month where the CTD casts cover the whole front (Fig. 5.1(a)), the results show that the temperature and salinity profiles present differences across the fjord (Fig. 5.1(b)). Temperature gradient, for instance, is larger in the lateral zones than in the central one, where the values are almost stable along the water column. The eastern zone exhibits more variability, while the largest values are reached in the central zone. Likewise, salinity profiles show dissimilarities between the central and the lateral zones, and the largest values are also reached in the central region. In the case of salinity, the gradient in both lateral zones exhibits similarities. Therefore, as a first approximation, the fjord conditions could be divided into three different zones:

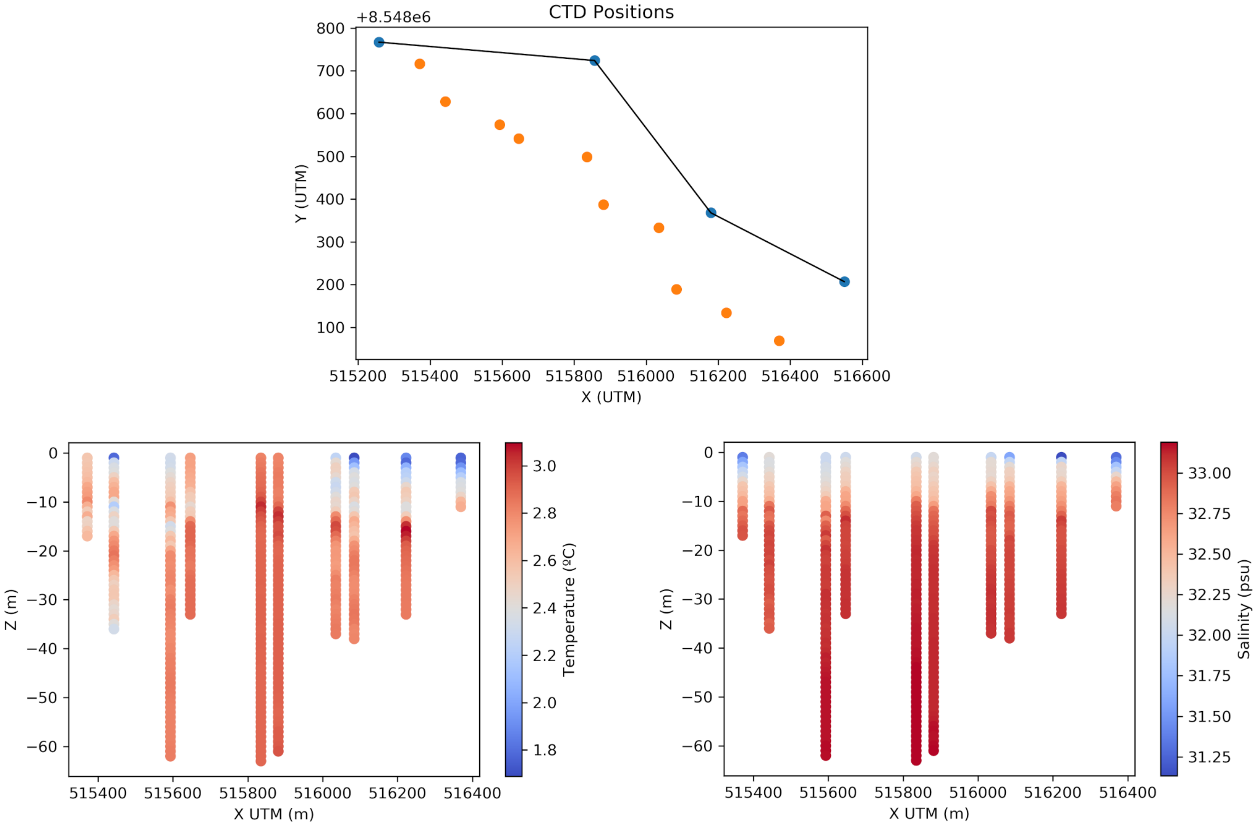

Figure 5.1: (a) Position of the CTD casts near the calving front for August 2010. The line represents the ice–ocean boundary and the orange dots the coordinates of the different CTDs. (b) Temperature and Salinity distribution across the fjord for August 2010. Every column represents a CTD cast.

$$\text{Fjord zones}\begin{cases}\text{West conditions,} & \text{if XCoor} \leq 515600 \text{ m UTM}\\ \text{East conditions,} & \text{if XCoor} \geq 516000 \text{ m UTM}\\ \text{Central conditions,} & \text{if any other case}\end{cases}$$

The results for April 2010 and July 2010 (Fig. 5.2(a), (b) respectively) support the election of these zones. Even so, it is interesting to point out that the number of CTD casts and the extension of the measurements is lower than in August. Besides, in April 2010 the largest values for the temperature are reached in the eastern zone. And there are still dissimilarities between the different zones of the front, but in the case of April that happens between the eastern zone and the other ones.

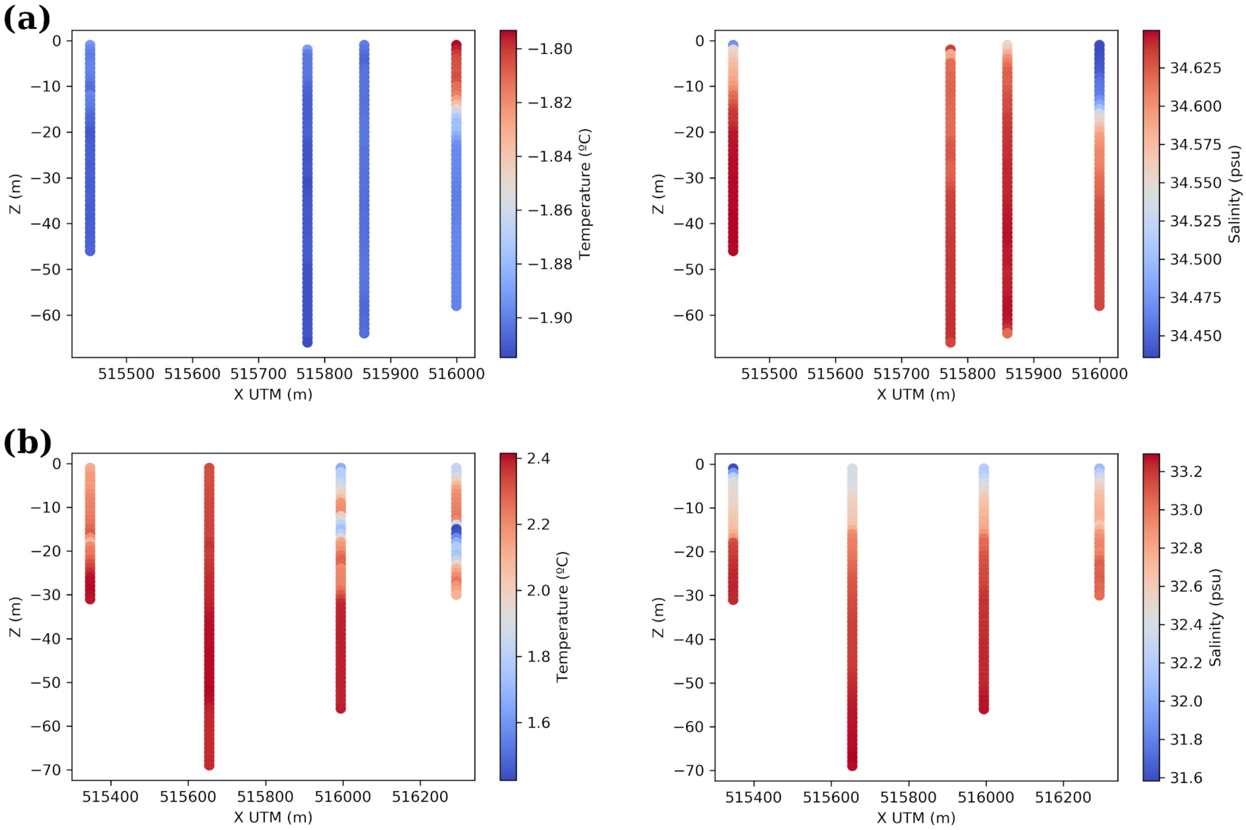

Figure 5.2: Temperature and Salinity distribution across the fjord for (a) April 2010 and (b) July 2010. Every column represents a CTD cast.

5.1.2 Refinement of he modelled velocities

The use of inversions to obtain the slip coefficient and, consequently, appropriate modelled velocities for the glacier, is a well–established technique employed for many authors working on glacier dynamics (Otero et al., 2017; Todd et al., 2018; De Andrés et al., 2018; Cook et al., 2020, 2022; Holmes et al., 2023, among others). One of the problems of this method is the high computational cost, hence the need for careful consideration of the balance between accuracy and computational efficiency. The mismatch between observed and modelled velocities is likely the main cause for the underestimation of the front advance (Fig. 5.3). For this reason, inversions were run again in order to obtain better estimations of the modelled velocities.

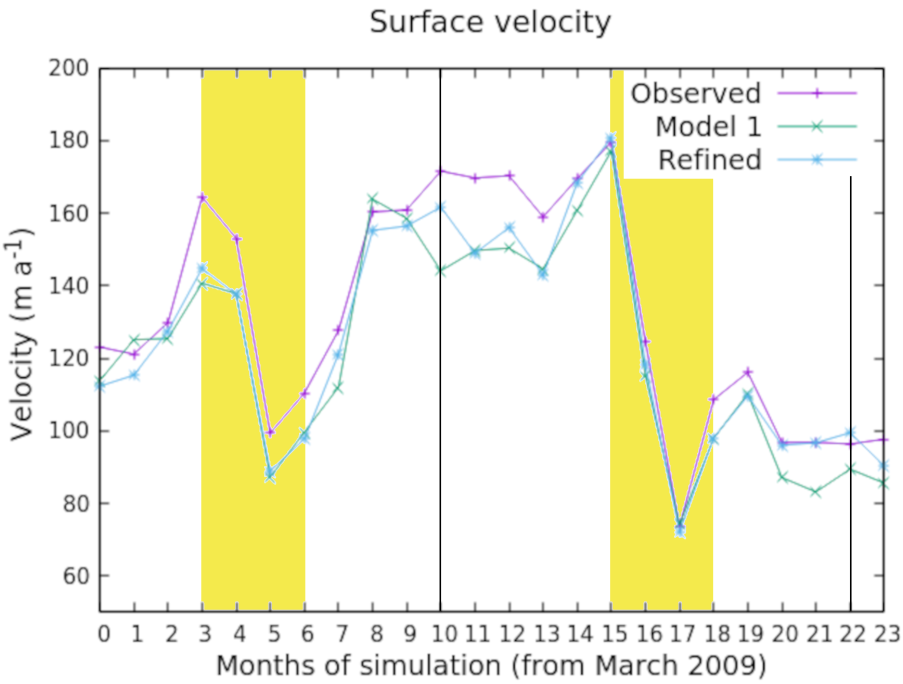

Figure 5.3: Time evolution of the velocity at the stake located closer to the calving front (the southernmost blue point in Fig. 3.4).The yellow areas indicate the summer periods and the vertical black lines separate the different years.

In general, with few exceptions, the new velocities are closer to the observed than the previous velocities used in the model in Chapter 4 (Fig. 5.3). The improvement in the estimation is clearly discernible at the end of the simulation. The mismatch between observed and modelled velocities has been reduced by 2.935 m$\cdot s^{-1}$, from 10.949 m$\cdot s^{-1}$ to 8.014 m$\cdot s^{-1}$, a 26,80 %. Even if in some months the modelled values are still not close enough to observations, such a significant refinement is expected to have an impact in the new simulations.

5.2 Experiments

Once the ambient conditions and the modelled velocities have been analysed, the main problems potentially caused for the input data of the model have been taken into account. But the eastern margin differences could be also related to the geometry of the problem itself. In the model, only the nodes of the glacier considered front nodes are permitted to evolve in terms of advance and retreat. The choice of those front nodes, thus, could be causing the problem in the eastern zone. Having in mind the described possibilities, two new sets of simulations have been proposed:

- **Experiment 1:** This set of simulations starts from the model included in Chapter 4 and incorporates the refinement of the modelled velocities and the implementation of the three–zone plume model. The results will be compared to the ones obtained in Chapter 4 (Model 1).
- **Experiment 2:** This set of simulations includes the same implementations as Experiment 1, and extends the front one node further east. The results will be used just to compare

the obtained front positions and verify whether the eastern margin problem persists or not.

5.3 Results

The main results of Experiment 1 simulations present similarities to the ones obtained in Chapter 4. Starting in March 2009, the modelled monthly values of surface meltwater, subglacial discharge, plume melt rate and calving volume present a seasonal pattern (Fig. 5.4). The largest SMW values are also reached in July (9.3×10^5 m^3 a^{-1} and 8.3×10^5 m^3 a^{-1} for 2009 and 2010 respectively), and the cumulative SMW for both summer seasons is of the same order of magnitude, being the value for 2009 ∼16 % higher than the one for 2010 (Fig. 5.4(a)). The largest subglacial discharge values are also reached in July (5.9×10^5 m^3 a^{-1} and 7.7×10^5 m^3 a^{-1} for 2009 and 2010 respectively), but in this case the total amount for summer 2009 is around 16 % lower than the one for 2010 (Fig. 5.4(b)). Beyond the summer months, the SMW and subglacial discharge maintain a baseline value around 1×10^5 m^3 a^{-1}, except for May, where the values double those numbers.

(a) Surface meltwater (b) Subglacial discharge

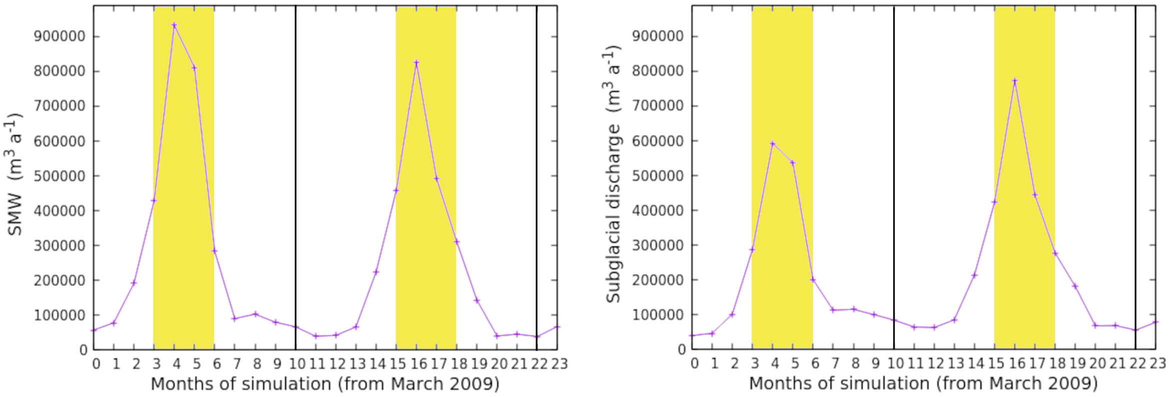

(c) Plume melt rate (d) Calving

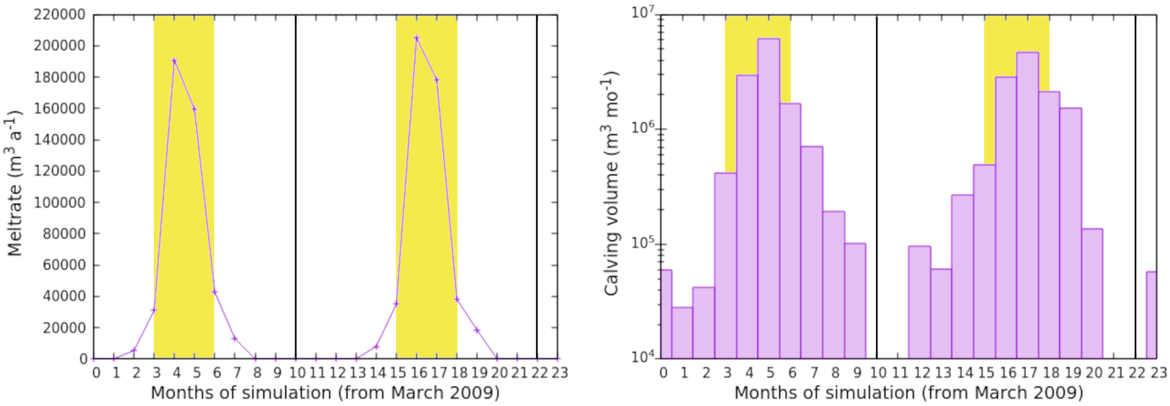

Figure 5.4: Temporal evolution of the (a) surface meltwater (SMW), (b) subglacial discharge produced by surface and basal melt, (c) total melt rate produced by plume activity computed on the first day of every month and (d) calving volume produced by the model for every month of the simulation (log scale). The yellow areas indicate the summer periods and the vertical black lines separate the different years.

The total melt rate due to plume activity presents a difference of ∼7 % between the two summer periods (4.2×10^5 m^3 a^{-1} and 4.6×10^5 m^3 a^{-1} for 2009 and 2010 respectively). The largest plume melt rates for each summer period are reached in July in both summer periods (1.9×10^5 m^3 a^{-1} and 2.1×10^5 m^3 a^{-1} for 2009 and 2010 respectively), with values for August around 15 % lower than the ones for July (Fig. 5.4(c)). Other than that, June and September exhibit values of the same order ($\sim 3.3 \times 10^4$ m^3 a^{-1} for June and $\sim 4 \times 10^4$ m^3 a^{-1} for September), and October and April present the lowest values, not negligible at all but definitely small compared to the other mentioned months. Note that no plume melt rate is produced from November to April, as no plumes are formed during these months.

Calving volume reaches the highest values in summer for both years (Fig. 5.4(d)). The total calving volume during the first summer (2009) is slightly bigger, ∼9 %, than during the second one (2010), 1.11×10^7 m^3 per month versus 1.01×10^7 m^3 per month. In both periods the distribution presents some similarities: August is the month with the largest calving volume, 6.11×10^6 m^3 per month for 2009 and 4.68×10^6 m^3 per month for 2010; July comes in second with 2.94×10^6 m^3 per month for 2009 and 2.85×10^6 m^3 per month for 2010, more than half the volume of August in the first summer but less than half in the second summer; September presents a value more than 20 % lower in 2009 than in 2010 (1.66×10^6 m^3 per month versus 2.12×10^6 m^3 per month), and June exhibits the lowest values, around 4.5×10^5 m^3 per month. The summer periods concentrate, on average, around 86 % of the calving total volume (2.13×10^7 m^3 per month out of 2.45×10^7 m^3 per month), but calving occurs during the whole simulation except for four months. Outside of the summer period, October exhibits values above the ones for June, almost double in the first year of simulation (7.07×10^5 m^3 per month for October and 4.18×10^5 m^3 per month) and significantly higher in the second one (1.53×10^6 m^3 per month for October and 4.94×10^5 m^3 per month). Finally, even if the calving volume is larger in the first summer, when taking the whole year, March 2009 to February 2010 and March 2010 to February 2011 present very similar values (1.226×10^7 m^3 per month and 1.228×10^6 m^3 per month for 2009 and 2010 respectively).

The calving front follows a seasonal pattern in terms of advance and retreat during the whole simulation period, generally retreating between July and October and advancing during the rest of the year (Fig. 5.5 (b)). The periods of advance are longer and the advancing rate moves from 7 m per month to 15 m per month of longitudinal difference. The periods of retreat, however, are shorter, concentrating the largest values in July and August. The retreating rate can reach up to -48.1 m per month. The largest negative values (indicating retreat) occur in August every year, with the closest values, obtained in July, being only half that amount (-48.1 m per month vs -20.3 m per month for 2009 and -37.1 m per month vs 18.9 m per month for 2010). Now, the total advance is practically the same during the first year (March 2009-2010), 100.71 m per month, as during the second one (March 2010-2011), 101.08 m per month. On the other hand, cumulative retreat in the first year amounts to -72.62 m per month, whereas in the second one the value is lower, -64.29 m per month (Fig. 5.5 (a)).

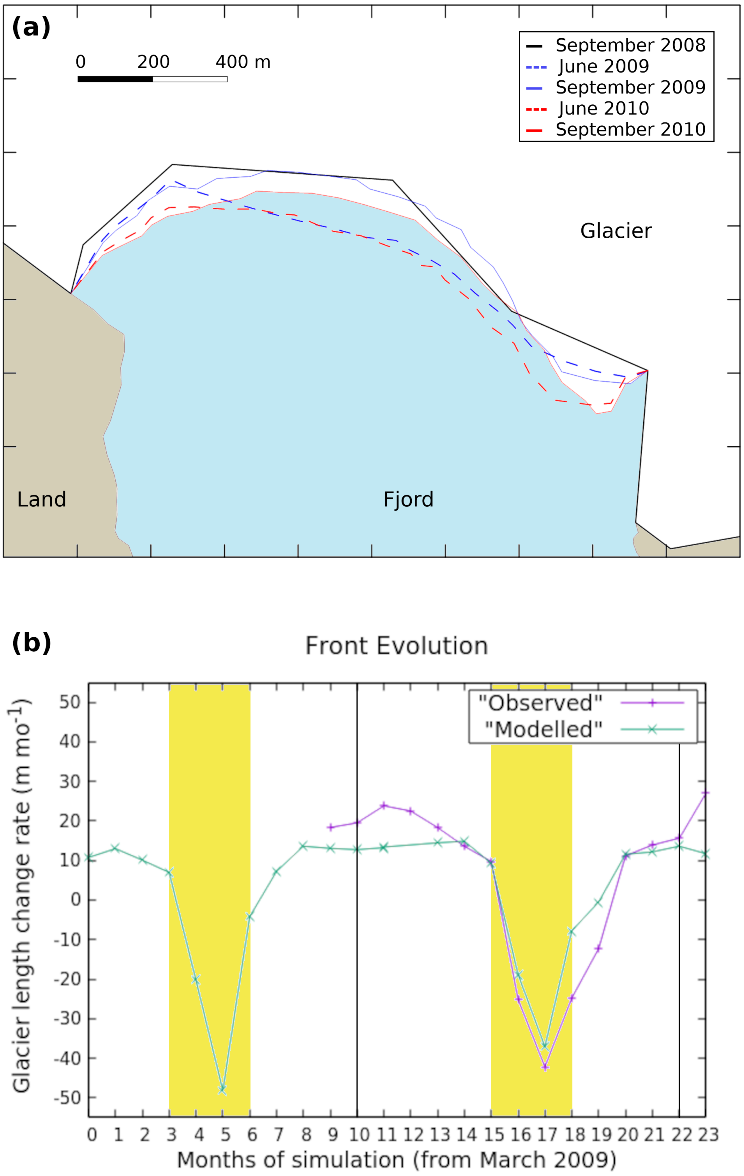

Figure 5.5: Calving front evolution. (a) The different positions represent the interannual evolution and the summer evolution of the calving front: the solid lines correspond to September 2008 (black), September 2009 (blue) and September 2010 (red), whereas the dashed lines correspond to June 2009 (blue) and June 2010 (red). (b) The graph represents the longitudinal difference along the whole simulation, calculated as the difference in area between subsequent months divided by the glacier width. The yellow areas indicate the summer periods and the vertical black lines separate the different years.

Summarising, by the end of the first year of simulation, March 2010, the front position has advanced 28.09 m per month with respect to the position in March 2009, while by the end of the second year of simulation, March 2011, the front position has advanced 36.78 m per month with respect to March 2010, resulting in a total advance of 64.87 m per month with respect to March 2009.

5.4 Discussion

5.4.1 Experiment 1

The results of the model indicate that the glacier presents a marked seasonal behaviour. Figures 5.3 and 5.4(a), (b) exemplify this feature in the input data as well. Subglacial discharge values correlate with surface meltwater values, with the first ones being generally higher than the second (Fig. 5.4(a), (b)). It has been applied a constant value of basal and internal melting ($\sim 2.6 \times 10^4$ m^3 a^{-1}) by using the geothermal heat flux defined in Sect. 2.1.3. This explains, as well as some other processes like internal refreezing, why in some months the subglacial discharge is larger than the SMW. The correlation presents, however, some anomalies in the first summer period. Even if the SMW values are larger than in the second summer period, the subglacial discharge values are lower for the first summer. The anomaly is especially important in July 2009, when the maximum difference between the SMW and subglacial discharge is reached. While during the second summer the subglacial discharge values represent around 90 % of the SMW, during the first summer period this percentage decreases to 65-70 %. It is not clear what could be happening, but one possible explanation for this subglacial discharge reduction would be a change in the efficiency of the drainage system that is not being captured by the model. A more thorough study of the subglacial hydrology should be carried out in order to find out what is going on.

Now, plume melt rate is affected by both fjord ambient conditions and subglacial discharge. The model calculates non–zero freshwater flux into the fjord in winter months (Fig. 5.4(b)), in agreement with Cook et al. (2020). However, in the present study, either the subglacial discharge values are not high enough or the winter ambient conditions are not suitable for the occurrence of plumes, unlike the work of Cook et al. (2020) (Fig. 5.4(c)) This is a limitation of the model since plumes have been observed at Hansbukta in winter. On the other hand, between April and October, both ambient conditions and subglacial discharge values are suitable for the occurrence of plumes, and, in general, there is a good correlation between the two variables. The ambient conditions in the fjord were kept the same for both summer periods. Hence, the differences between them can be explained by the differences in the subglacial discharge that feeds the plumes. This fact is exemplified during the second summer, where the increase in the subglacial discharge values with respect to the previous summer period produces higher melt rate values (Fig. 5.4(b), (c)). As an exemplification, Fig. 5.6 shows different distributions of the plume melt rate at the calving front: a low–melting month at the beginning of the plume activity period, April 2010 (a), a high–melting month at the beginning of the summer period, June 2010 (b), a very high–melting month, August 2010 (c) and a low–melting month at the end of the plume activity season, October 2010 (c). The plume melt rate in the summer months is not only higher than the plume melt rate in April and October, but it also extends to a larger area of the calving front. October, however, still exhibits large values compared to April, and fair values compared to June, even if the extension of the plume activity does not extend to the whole front.

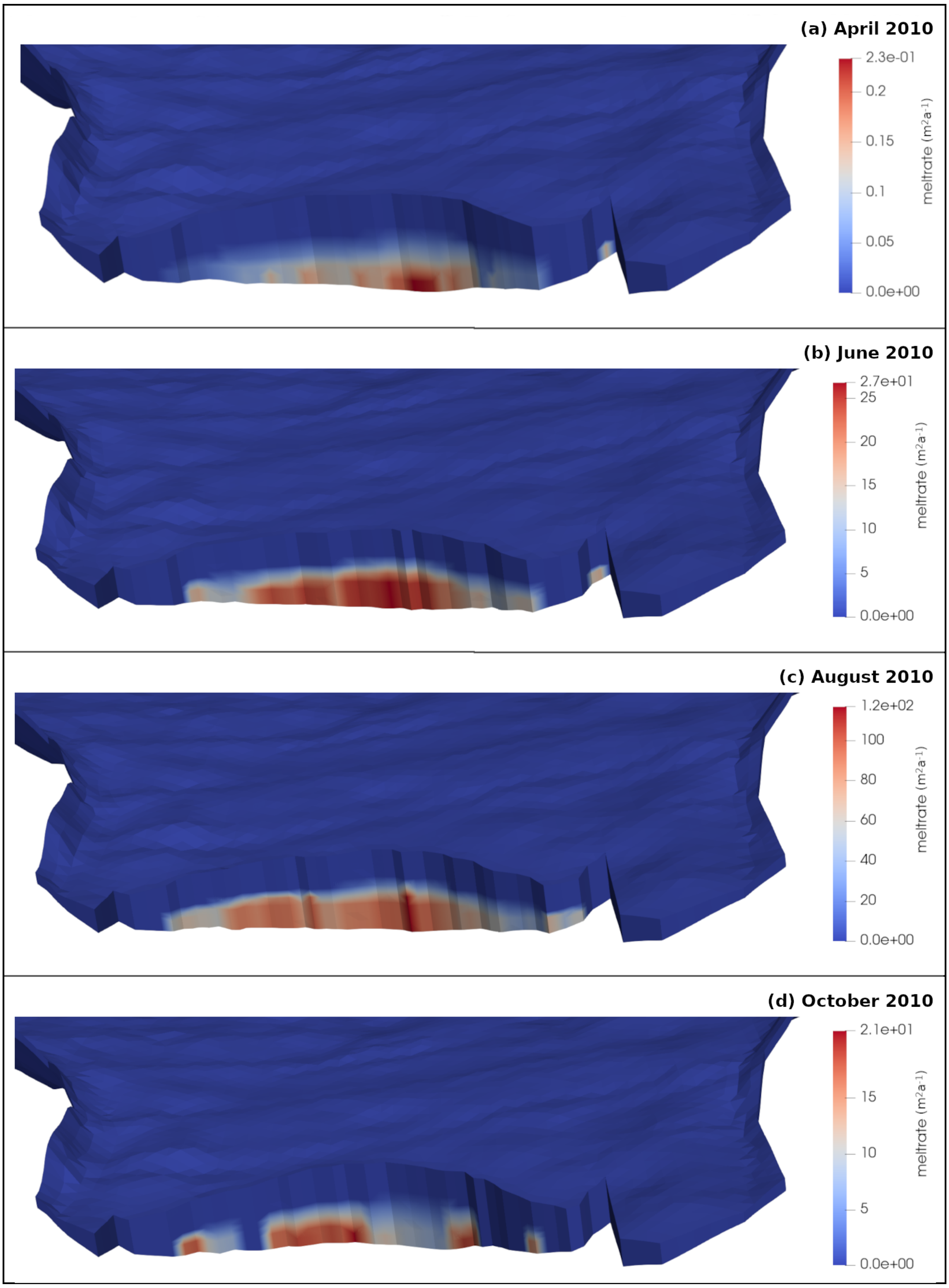

Figure 5.6: 3D aerial view of the glacier calving front for (a) April 2010, (b) June 2010, (c) August 2010, and (d) October 2010. The red zones represent high values of melt rate due to plume activity, although the scales used are not the same. Different scales have been chosen to account for the significant differences between the values.

As for the calving volume, the total amount in the two years of simulation is very similar, 1.226×10^7 m^3 per month and 1.228×10^7 m^3 per month for 2009 and 2010 respectively. This is consistent with the slightly difference in the plume melt rate, 4.4×10^5 m^3 a^{-1} for 2009 and 4.8×10^5 m^3 a^{-1} for 2010. From the results of this model it is not possible to establish an exact relation between plume melt rate and calving. On the one hand, larger calving volumes concentrate in the summer season, where plume activity is stronger, but, on the other hand, the largest values of calving are reached in August, whereas the strongest plume activity occurs in July. Besides, the values of calving volume are higher during the first summer, while the largest values for plume activity are reached during the second summer. And some months like May or October present a substantial difference in terms of calving volume although they have similar plume melt rate values. Even so, in general, there is a clear correspondence between plume activity and calving, in agreement with other studies such as Holmes et al. (2023), with the most intense plume activity consistently associated with the highest calving rates.

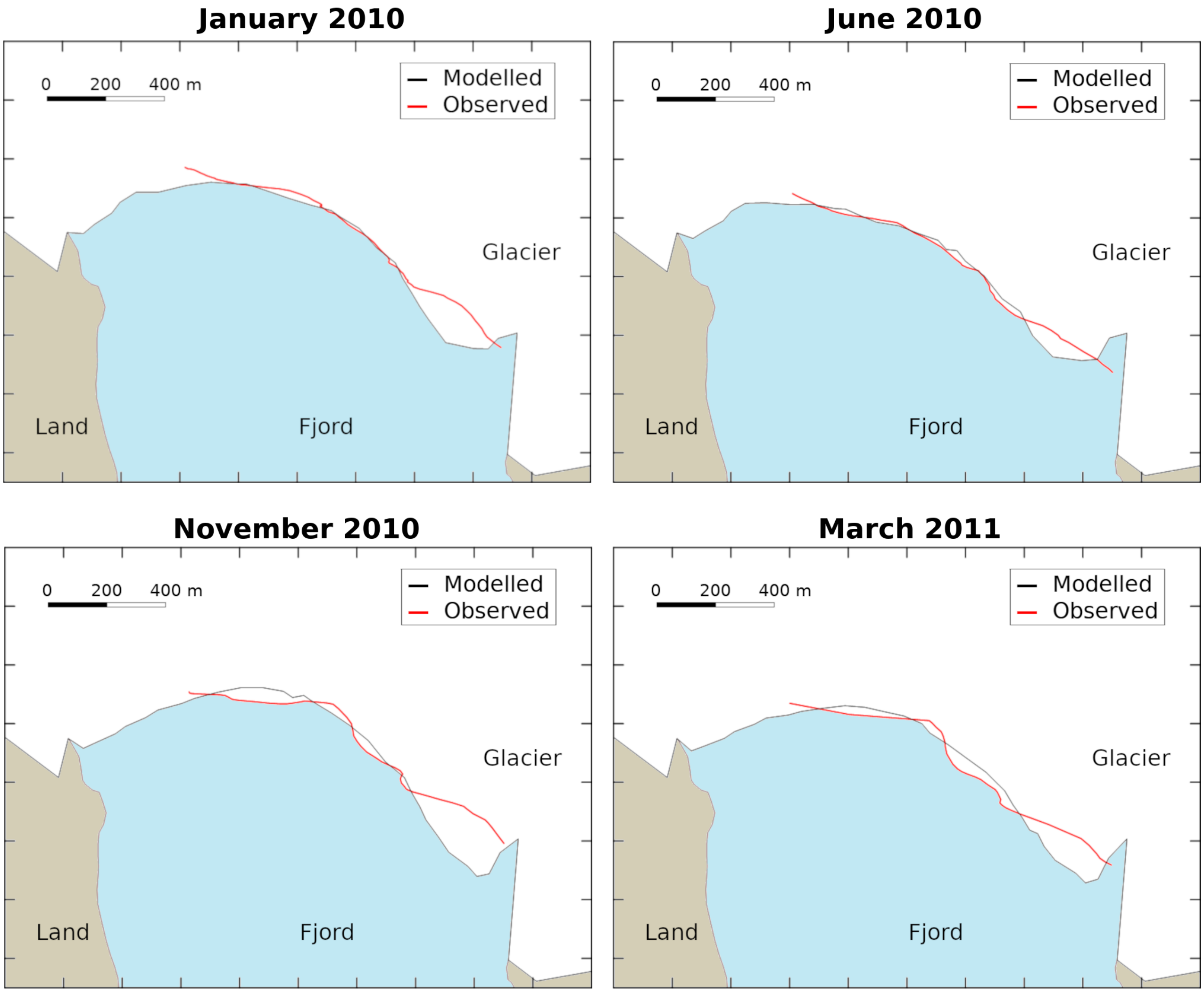

Figure 5.7: 2D aerial view of the glacier–fjord system for January 2010, June 2010, November 2010 and March 2011. The solid black lines represent the modelled contour of the glacier and the red lines, the observed front position. Note that the observational data do not cover the westernmost part of the front.

To study the evolution of the calving front and how it compares to the expected behaviour of a tidewater glacier, Fig. 5.5 outputs some interesting features. First of all, the glacier advances steadily during the winter months, when calving is not present in general, and retreats during the summer months, especially in August, when it reaches the highest absolute values. In general, the model is able to reproduce the seasonal tidewater glacier behaviour since the modelled front evolution follows the same pattern as the observed one (Fig. 5.5(b)). However, both advance and retreat of the calving front are being underestimated. The first occurs during the spring and winter, when calving is low or nonexistent. The second occurs in summer and early autumn, especially in September and October. A more than possible explanation for the advance underestimation could be attributed to the fact that the modelled velocities are generally lower than the observed ones (Fig. 5.3(b)), while calving underestimation is very likely to be the most important factor in the retreat dissimilarities. Secondly, calving is, by approximately two orders of magnitude (Fig. 5.4(c), (d)), the main contributor to frontal ablation, but plume–induced melting can lead to a larger number of calving events, so both factors are important in the control of the front position. Finally, the glacier front remains quite stable during the study period (Fig. 5.5(a)). In fact, it shows a small advance between September 2008 and 2010, in agreement with Błaszczyk et al. (2021).

To validate the model performance, we also compare the modelled and observed front positions (Fig. 5.7). The modelled positions are, on average, more advanced than the observed ones, but there is a strong variability. For instance, in June 2010 the positions are really closed, whereas in November the differences are significant. As mentioned, the difference between modelled and observed positions varies throughout the simulation (Fig. 5.8). It starts by a decreasing period from December 2009 to May 2010. Afterwards, there is steady period from June 2010 to September 2010. Then there is an increasing period from October 2010, reaching the maximum value in December 2010. Finally, there is a new decreasing period until the end of the simulation in March 2011. There seems to be a seasonal pattern, supported by the underestimation of both, the retreat and the advance of the modelled front. But the lack of observational data beyond March 2011 does not allow us to establish such a thing. The results present a marked contrast between the central part and the east lateral margin of the glacier front, so that the maximum differences in the eastern zone of the front are approximately 10 times larger than in the central one. This is likely due to the lack of calving events produced by the model in that region of the glacier front that could be caused by low plume–induced melting in the area. In general, the performance of the model is better when removing the lateral parts, especially the eastern area, and looking just at the central 700 m of the calving front. On average, the modelled positions are $\sim$43.3 % closer to the observed positions when taking just the central part (10,59 m versus 18.68 m for the total front), with most of the values, 68.75 %, below 10 m, and half of the values below 8 m. Even so, in late spring and early summer, the differences in both cases, taking the whole calving front or just the central part, are considerably small.

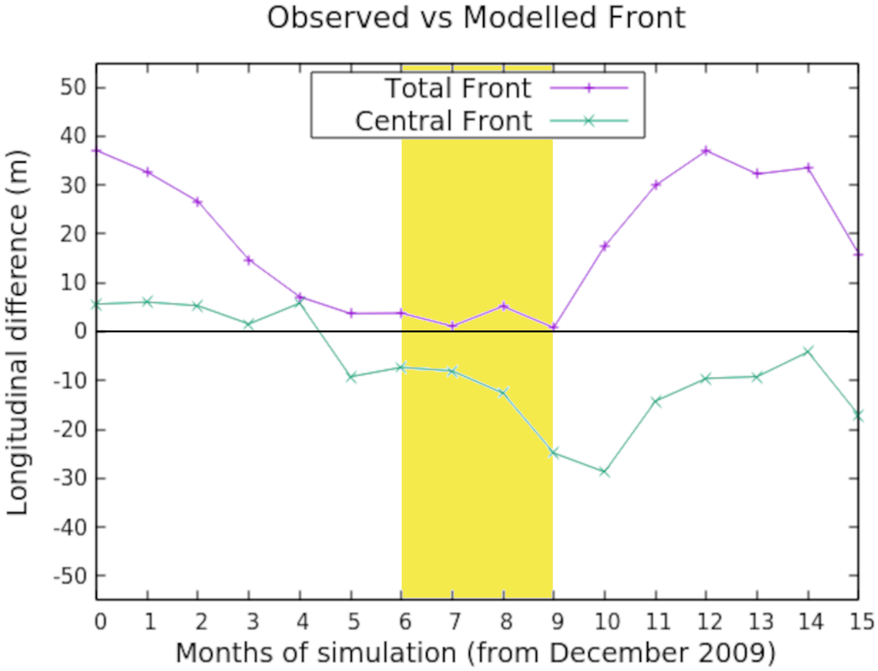

Figure 5.8: Evolution of the longitudinal difference between the modelled and the observed front position calculated as the difference in area between them divided by the glacier width (blue line), and that same evolution restricted to the central 700 m of the calving front (red line). Positive values indicate that the modelled front is more advanced than the observed, while negative values indicate the opposite. The zero is marked with a horizontal black line so values closer to that line indicate a better agreement between modelled and observed positions. The yellow area indicates the summer period (June to September 2010).

Although a comparison between a 2D and a 3D model must be handled carefully, our results show a deviation with respect to observations of ±10 m for the central 700 m of the calving front for almost the whole period between December 2010 and March 2011. This is the same deviation value obtained by De Andrés et al. (2018) for their flow line model. To obtain those results, they needed to include a non–dimensional adjustable parameter used to parameterize the crevasse water depths (CWD). In contrast, our model uses the 3D calving implementation of Todd et al. (2018), which ignores this process, so we do not need any CWD parameterization. Therefore, the inclusion of an across glacier dimension extends the best results of the 2D model to the central 700 m of the calving front, where the 3D model predicts the observed front position with a good level of agreement. However, there is a region where the modelled positions are clearly behind the observed ones. The escalation of the difference coincides with the months when calving is larger at the glacier. Consequently, the cause of this increase could be, again, an underestimation of calving by the model. And the reasons would be that the model is not able to capture all calving events occurring at the glacier due to the underestimation of the input velocities or an underestimation of submarine melting, since higher values of submarine melting can enhance calving. So these factors have to be closely examined in order to improve the performance of the model.

5.4.2 Comparison between the models

Results from the model presented in Chapter 4 (Model 1) and from the model including the refined velocities and the three–zone plume (Experiment 1) exhibit, on the one hand, a similar seasonal behaviour (Fig. 5.9). In both cases, there are characteristic responses to summer conditions and the largest values of the SMW, subglacial discharge, plume melt rate and calving are reached during those months. But, on the other hand, there are some important dissimilarities.

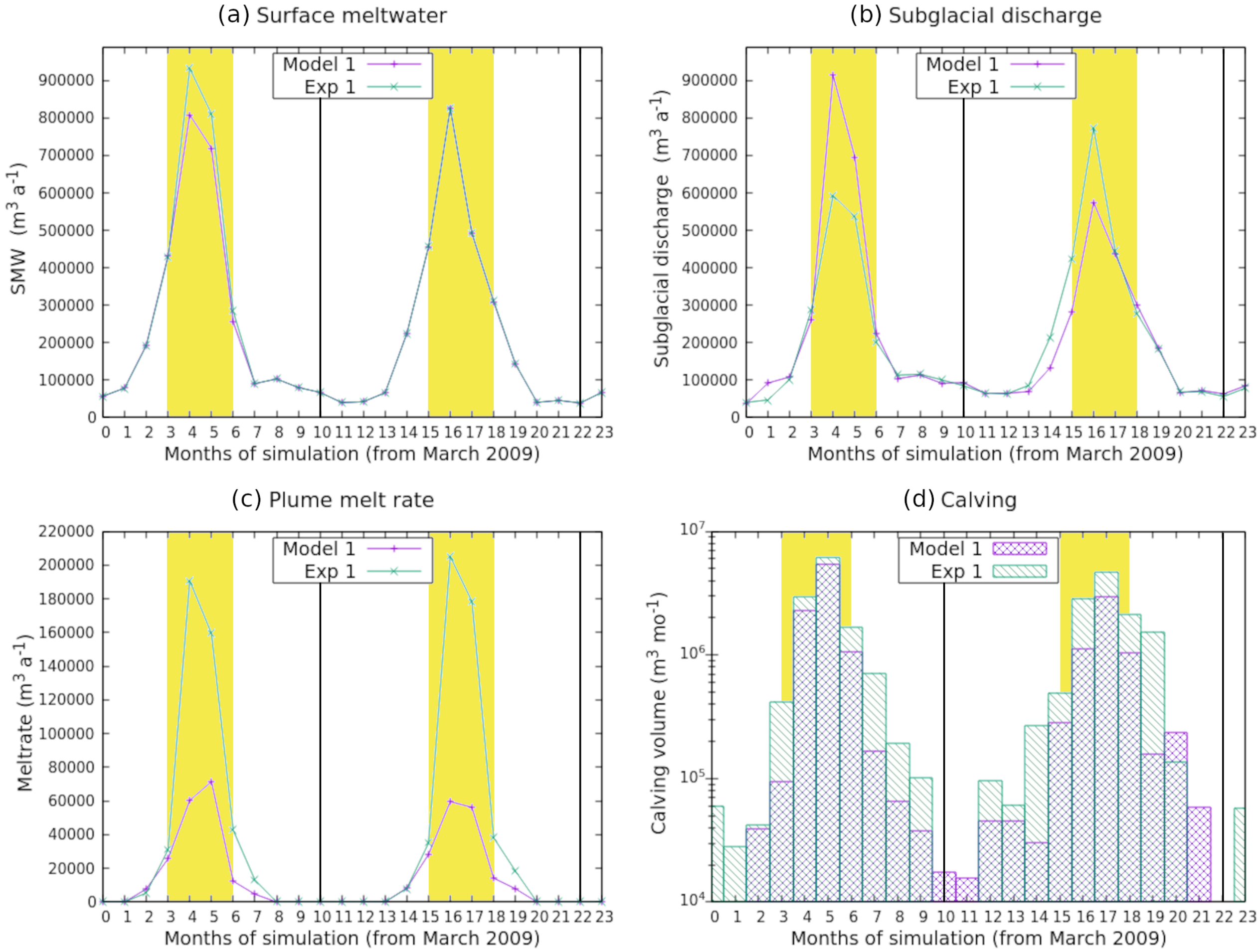

Figure 5.9: Temporal evolution of the (a) surface meltwater (SMW), (b) subglacial discharge produced by surface and basal melt, (c) total melt rate produced by plume activity computed on the first day of every month and (d) calving volume produced by the model for every month of the simulation (log scale). The yellow areas indicate the summer periods and the vertical black lines separate the different years.

First, the SMW during the first summer period is larger in Experiment 1 than in Model 1 (Fig. 5.9(a)). This increase, however, only occurs in July and August 2009, while in the rest of the months the values are practically the same. But July and August are the months that exhibit the largest values for SMW, and the maximum values for the SMW concentrate next to the calving front. Consequently, the differences could be attributed to variations in the glacier extension. This is very likely taking into account that, for Model 1, September and October 2008 are months with very large retreat rates in comparison to Experiment 1. Therefore, the extension of the Model 1 glacier is larger than the extension of the Experiment 1 glacier during the first months of simulation. Actually, those differences decrease after July and August 2009 because in those two months the retreat rates are larger for Experiment 1 than for Model 1.

Secondly, subglacial discharge presents differences in the two summer periods, but other than that, the values are practically the same – with the exceptions of April 2009 and May 2010 (Fig. 5.9(b)). During the first summer, the discrepancy between the values for July is very pronounced, being the value for Model 1 around 35 % larger than the one for Experiment 1. August 2009 also presents a larger value for Model 1 than for Experiment 1, with a variation around 23 %, lower than the one for July, but still very important. It is not evident why the values of subglacial discharge are swapped with respect to the values of the SMW, as the SMW is larger for Experiment 1 than for Model 1 for those months. In the previous section, a change in the efficiency of the drainage system that is not being captured by the model was suggested as an explanation for the decrease in the subglacial discharge. But it is difficult to establish such a thing without a more thorough examination of the subglacial hydrology, something out of the scope of this work. Likewise, during the second summer period there is a discrepancy between the subglacial discharge values for the two models. Actually, the discrepancy starts in late spring, May 2020, and extends only until July. In this case, it is Experiment 1 which presents larger values than Model 1, even if the SMW values are nearly the same for both models. Again, the decrease in the subglacial discharge for Model 1 was attributed to a change in the efficiency of the drainage system that is not being captured by the model. But, in the same way as before, such a thing cannot be established without further examination of the subglacial hydrology. Overall, the total amount of subglacial discharge for the two periods is almost the same, 5.13×10^6 m^3 a^{-1} for Model 1 and 5.03×10^6 m^3 a^{-1} for 2010, while the total amount of SMW is also quite similar, but the value for Model 1 is lower than the one for Experiment 1, 5.68×10^6 m^3 a^{-1} versus 5.92×10^6 m^3 a^{-1}.

Thirdly, melt rate due to plume activity is notably higher for Experiment 1 than for Model 1 (Fig. 5.9(c)). For the first summer period, even if the subglacial discharge values are larger for Model 1, the plume melt rate values are considerably lower than those of Experiment 1. During the second summer period, July and August exhibit substantially larger values for Experiment 1 than for Model 1, although the subglacial discharge values for August are similar – the same thing happens in September and October 2010, where the subglacial discharge is similar for the two models and still there are noteworthy differences in plume activity. In a month with a fair activity like September 2010, plumes are present in more zones of the front and with larger values of melt rate for Experiment 1 than for Model 1 (Fig. 5.10). Particularly Experiment 1, unlike Model 1, shows plume activity in the eastern zone of the glacier front in September 2010. This fact points out the importance of the fjord conditions in the plume formation and in comparison to the subglacial discharge. Comparing with other authors working on the same glacier–fjord system, the maximum melt rate values obtained in Model 1 for August 2010 are consistent with the ones obtained by De Andrés et al. (2018) (58 m^3 per month versus 64.28 m^3 per month (15 m^3 per week)). However, the maximum melt rate values obtained in Experiment 1 for August 2010, around 116 m^3 per month, almost double that quantity.

(a) Exp 1 (September 2010)

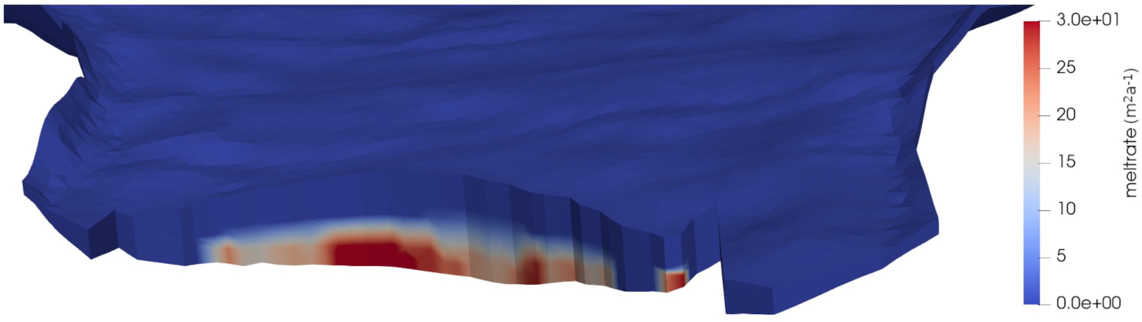

(b) Model 1 (September 2010)

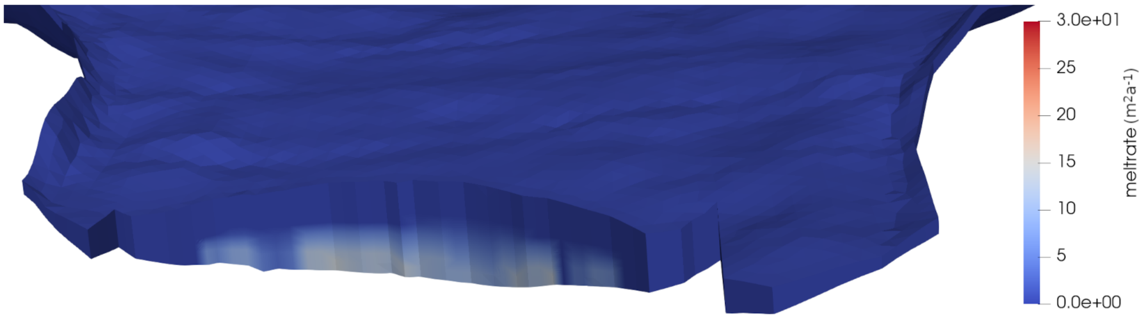

Figure 5.10: 3D aerial view of the glacier calving front corresponding to September 2010 for (a) Experiment 1, and (b) Model 1. The red zones represent high values of melt rate due to plume activity.

Lastly, calving volume shows a similar pattern for both Model 1 and Experiment 1, but the values present significant differences during the whole simulation, especially in the second year (Fig. 5.9(d)). The biggest calving volumes are produced during the summer periods, corresponding to the highest values of the plume melting, but in both models, calving is present in 20 out of 24 months of the simulation, even if in some cases the values are very low. During the first summer, calving volume in Experiment 1 is around 20 % bigger than in Model 1. This percentage increases a bit, around 25 %, when taking the first year of simulation. During the second year, the difference significantly scales up to ∼46 % when taking just the summer period, and reaches 51.4 % for the whole year. As for the total period of simulation, the variation is of ∼ 38 %. Comparing now the differences in plume melt rate between the models during the whole simulation, the value for Model 1 is around 40 % of that for Experiment 1. The variation, thus, is larger in melt rate than in calving volume. Furthermore, the largest values of calving are reached in August and not in July, when the largest values of the plume melting are reached. Therefore, it cannot be established a direct correlation between plume activity and calving. Even so, in general, the results show that the larger the former, the larger the latter.

Now, regarding the evolution of the glacier front, Model 1 and Experiment 1 both are underestimating the front advance (Fig. 5.11). The two models show a similar behaviour during the advance period. There are some months – concentrated in the first year of simulation – in which Model 1 exhibits a larger advance compared to Experiment 1, and some others – concentrated in the second year or simulation – in which Experiment 1 advances at larger rates. But the differences are not really important and practically compensate when taking the two years of simulation. On the contrary, the retreat periods present a marked difference between Model 1 and Experiment 1, with the latter showing larger retreat values during the two summer periods. Nothing can be said about the observed front during the first year of simulation, since no values are provided. But, during the second year of simulation, the increase in the retreat rates for Experiment 1 brings it closer to the observed front. Still, the value for September 2010 is pretty far from the observed one. Overall, Experiment 1 and Model 1 reproduce the seasonal advance and retreat cycle of the glacier, but underestimate both the advance and the retreat rates. But, with the refinement of the velocities and the application of the three–zone plume, Experiment 1 significantly improves the results in the retreat season. During the first summer, the retreat values of Experiment 1 are also larger than the ones of Model 1, but the lack of data prevents the possibility to confirm if this improvement extends to the whole simulation. Finally, there are some months where the difference in the advance rate has not been addressed only with the refinement of the velocities. Therefore it is something that should be more closely examined in the future.

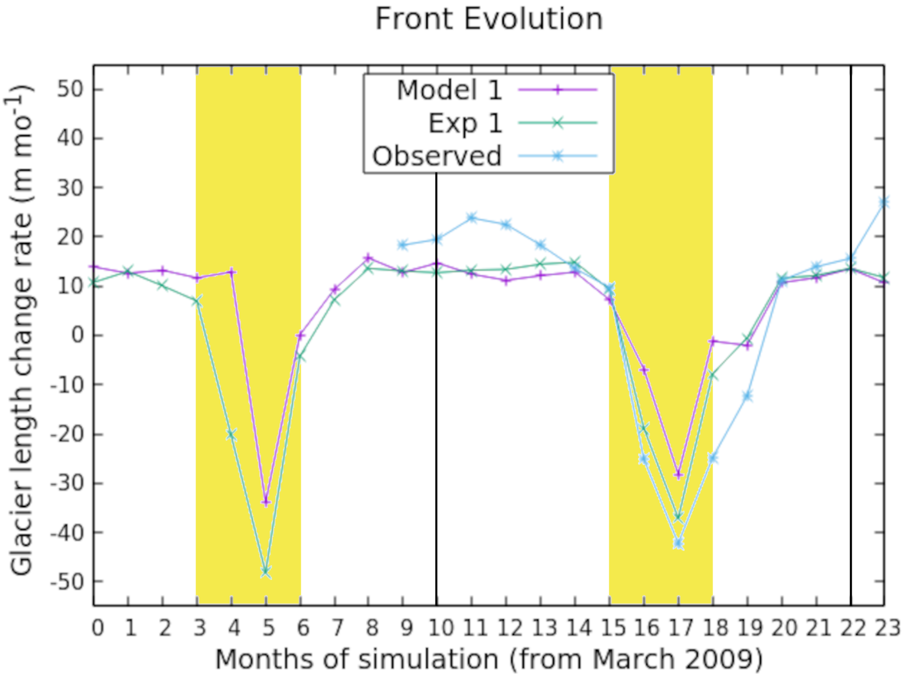

Figure 5.11: Calving front evolution. The graph represents the longitudinal difference along the whole simulation, calculated as the difference in area between subsequent months divided by the glacier width. The yellow areas indicate the summer periods and the vertical black lines separate the different years. Observations start in December 2009.

When comparing the front positions, Experiment 1 shows better results than Model 1 at first glance, especially during the first months (Fig. 5.12). Experiment 1 positions are closer to observations than Model 1 positions except in the easternmost part of the front, where both are significantly far anyway. From November 2010 to the end of the simulation, there are areas of the front where Model 1 is closer to observations but, on average, still Experiment 1 shows a better performance (Fig. 5.13). The two models exhibit variability when compared with observations, with a pattern somehow similar in both cases. At the beginning of the comparison, December 2009, the positions are relatively far from observations. As the months go by, the differences start to decrease. In late spring and early summer, the results are considerably good for both models, being Experiment 1 the best of them. Model 1 starts to increase the difference with respect to observations in August, but Experiment 1 remains really close until October. Beyond that, both models reach the worst result in December 2010, from when differences go down again. On average, Model 1 longitudinal difference with respect to observations is 36.65 m, while Experiment 1 reduces that until 18.86 m, practically half the value of Model 1. Even if the best results for Experiment 1 are reached in July and September, the most remarkable improvement takes place in the following months, with a reduction of around 52 % during the period October 2010 to March 2011.

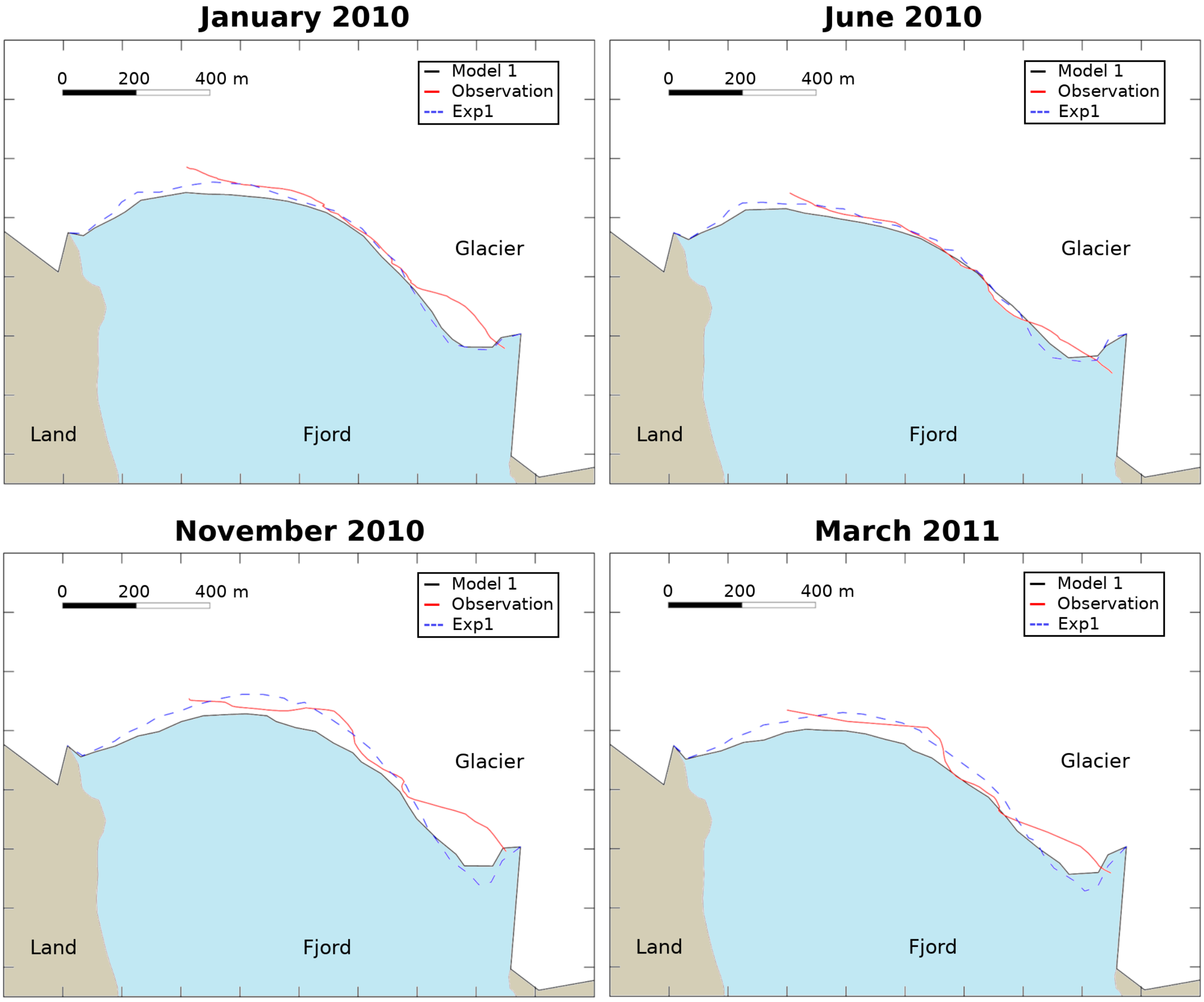

Figure 5.12: 2D aerial view of the glacier–fjord system for January 2010, June 2010, November 2010 and March 2011. The solid black lines represent Model 1 contour of the glacier, the blue dashed line represent the front estimated by Experiment 1, and the red lines represent the observed front positions. Note that the observational data do not cover the westernmost part of the front.

But results are even better when taking just the central part of the glacier front. Just looking at Fig. 5.12, it is easy to see a discrepancy between the central zone of the glacier front and eastern margin. In both cases, the easternmost 250 to 300 m present a strong disagreement between any of the models and observations. But the westernmost part of the observed front also shows large differences when compared to Model 1. Experiment 1, however, improves the western differences and problems only persist in the last points, where it can be considered that the observations could even present some errors. Therefore, it is interesting, on the one hand, to consider that neither of the models are properly solving the eastern margin. On the other hand, Model 1 obtains its best results when looking only at the central 350 m, while in Experiment 1 the best results are obtained taking into account the central 700 m, doubling the extension considered for Model 1. When comparing both, Model 1 central 350 m and Experiment 1 central 700 m results Fig. 5.14, some interesting insights arise. First, the improvement of Model 1 when taking just the central part is significant, around 60 %, and greater than the improvement of Experiment 1, around 43 %. Still, both percentages are notable and manifest the importance of the eastern margin disagreement into the main results. Second, although the improvement of Experiment 1 is lower in comparison with that of Model 1, Experiment 1 exhibits a better solution for the total front, and, therefore, the final results are still better and closer to observations than the ones of Model 1. Besides, this model is doubling the 350 m of Model 1, extending the good results to a very important length of the calving front. The best result of both series is that of April 2010 for Model 1, 0.765 m, whereas Experiment 1 does not reach any value below 1 – 1.567 for March 2010 is the closest one. The worst result, however, belongs to Model 1, 30.893 for November 2010, while Experiment 1 worst value is slightly lower, -28.739 for October 2010. There are just 4 months in which the solution for Model 1 is closer to observations, and, on average, Experiment 1 – even taking a longer part of the front – refine the solution up to 26 %. Finally, Model 1 central 350 m comparison basically exhibits positive values – all months except for August – while Experiment 1 central 700 m comparison shows a majority of negative values. The first corresponds to an underestimation of both, advance and retreat rates of the calving front, and the second corresponds to a better estimation of the retreat, while still underestimating the advance (Fig. 5.11). Therefore, the preponderance of negative values.

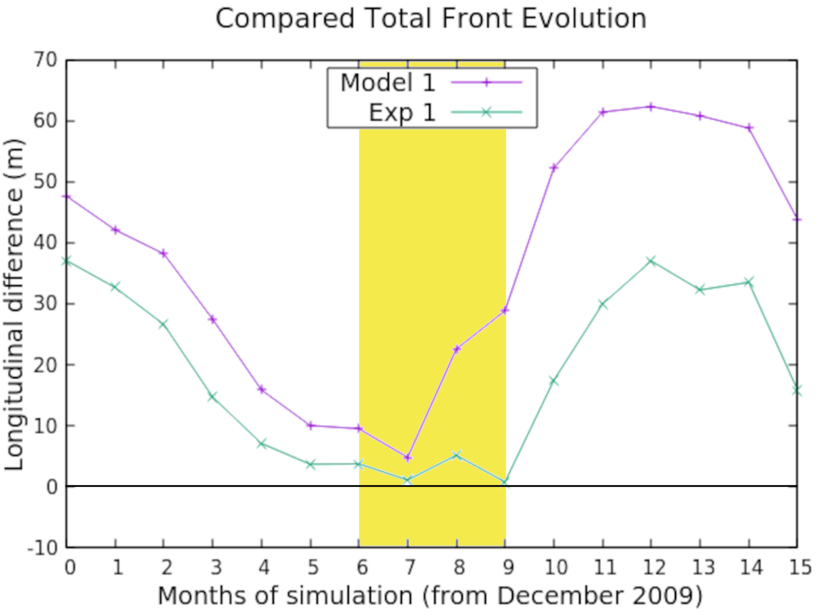

Figure 5.13: Evolution of the longitudinal difference, calculated as the difference in area between model and observations divided by the glacier width, for Model 1 and Experiment 1. Positive values indicate that the modelled front is more advanced than the observed, while negative values indicate the opposite. The zero is marked with a horizontal black line so values closer to that line indicate a better agreement between modelled and observed positions. The yellow area indicates the summer period (June to September 2010).

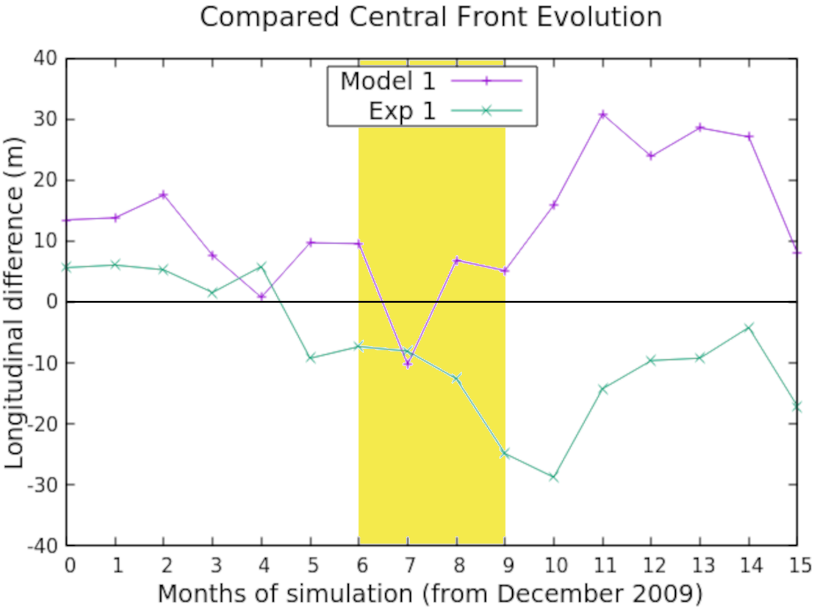

Figure 5.14: Evolution of the longitudinal difference reduced to the central 350 m for Model 1 and to the central 700 m for Experiment 1. Positive values indicate that the modelled front is more advanced than the observed, while negative values indicate the opposite. The zero is marked with a horizontal black line so values closer to that line indicate a better agreement between modelled and observed positions. The yellow area indicates the summer period (June to September 2010)..

Nevertheless, the issue in the eastern margin persists. In order to address this problem, Experiment 2 proposes to extend the front one node further east. This way, there would be more flexibility in that part of the front – since there is a new node of the front that is able to move – and the solution may be more close to observations. The results show a moderate improvement, especially in the zone closer to the central front. But still not good enough to

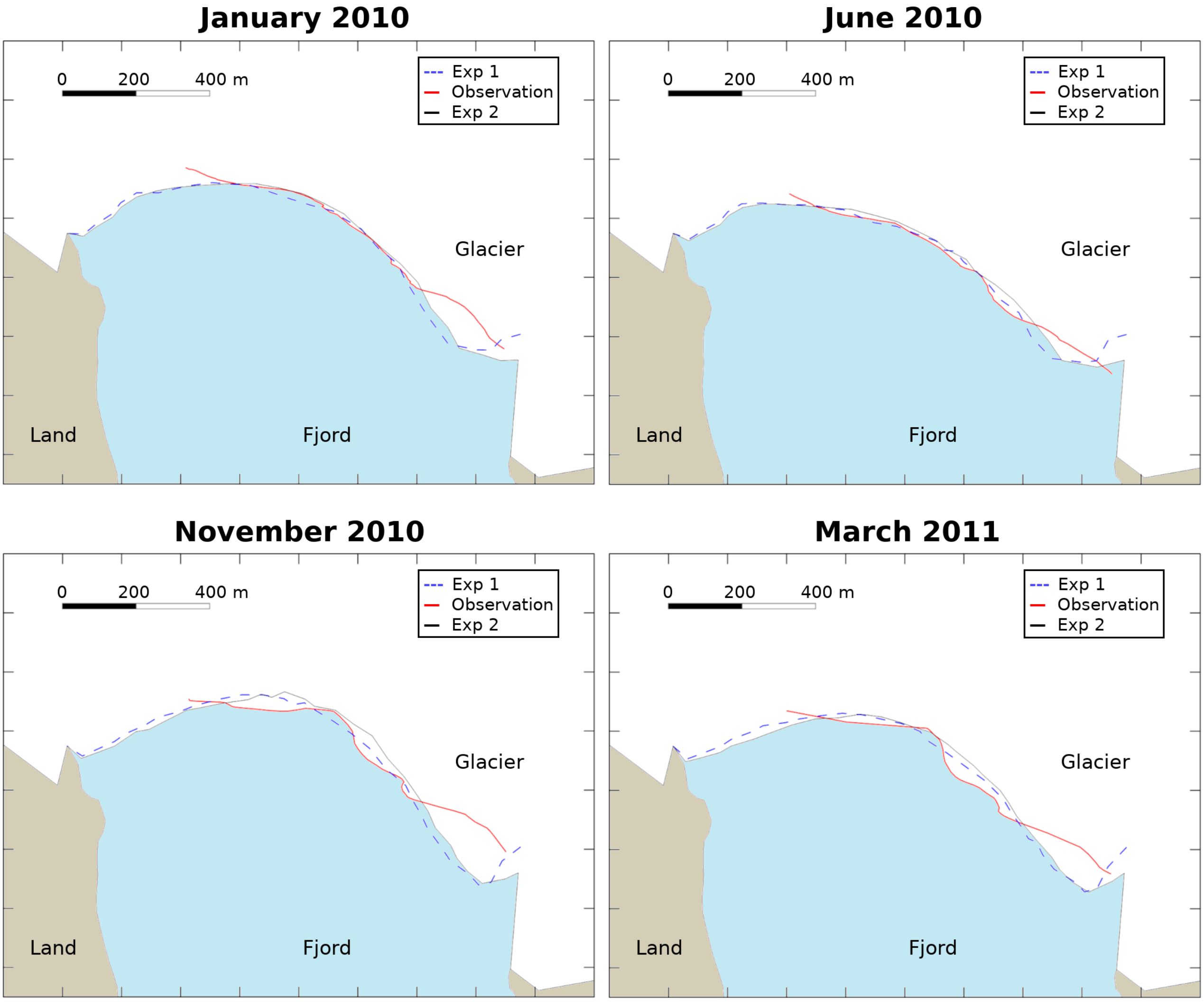

Figure 5.15: 2D aerial view of the glacier–fjord system for January 2010, June 2010, November 2010 and March 2011. The solid black lines represent Experiment 2 contour of the glacier, the blue dashed line represent the front estimated by Experiment 1, and the red lines represent the observed front positions. Note that the observational data do not cover the westernmost part of the front.

solve the problem. It could be said, therefore, that the selection of the front nodes, i.e, the nodes that are going to be able to move back and forth, is important and has effects on the behaviour of the front margins, but there are other factors that have to be taken into account.

To illustrate the eastern margin problem, another approach is an analysis of the observed front positions (Fig. 5.16). Hence, it can be established if the problem is related to a greater advance, a lack of retreat of any other characteristic that the model could be not capturing. Figure 5.16 (a) shows the advance of the front from winter to summer, and it is clear that the eastern part of the front is moving forward during those months. Similarly, during the retreat period, the eastern part of the front is moving backwards (Fig. 5.16) (b)). Therefore, it is clear that the observed front is able to advance and retreat, whereas the modelled front – with any of the models – is advancing, but not retreating, or just barely retreating. Consequently, the more important factor affecting that zone would be calving underestimation.

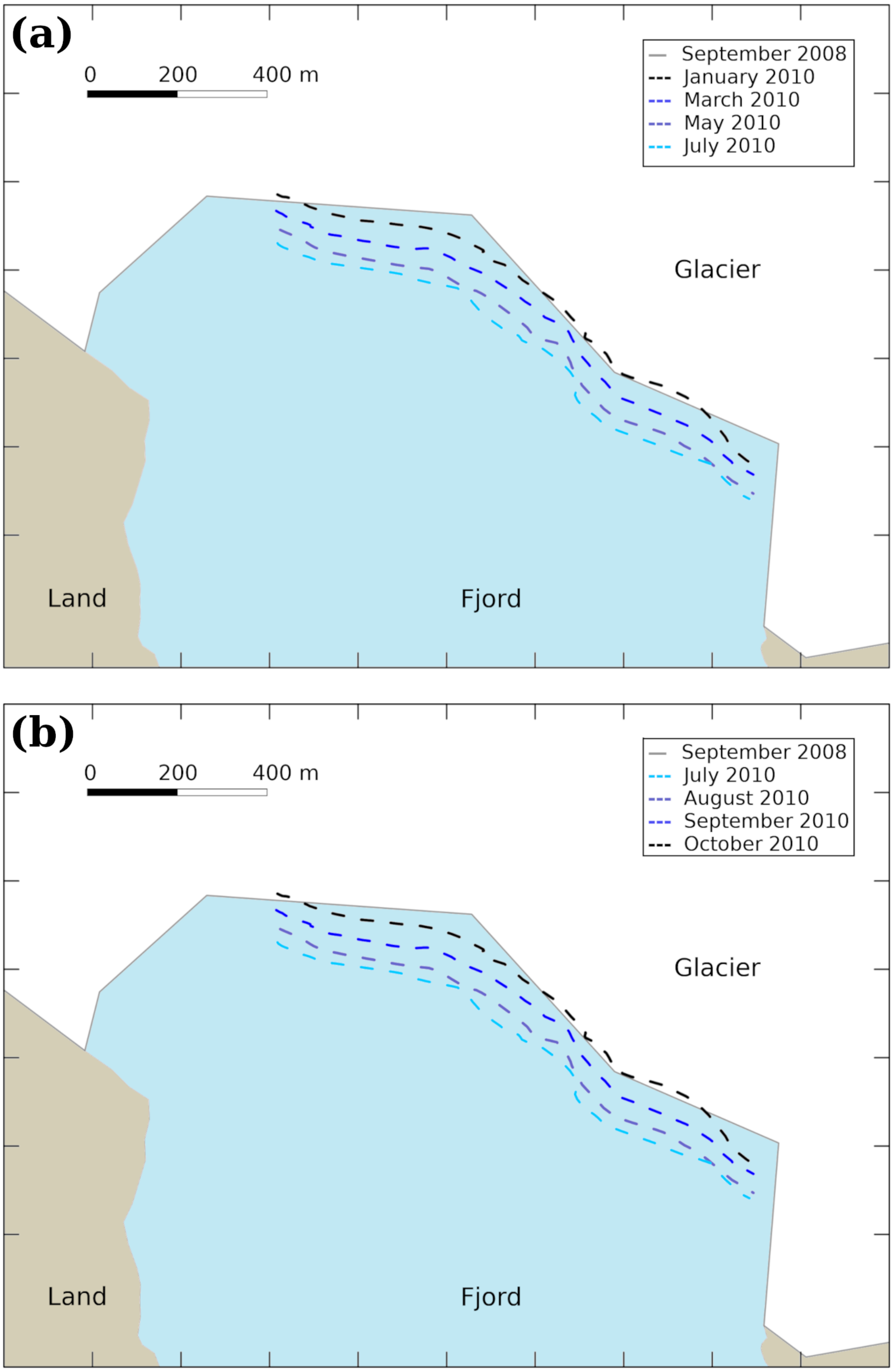

Figure 5.16: (a) Observed glacier front positions during the advance period. The dashed lines correspond to January, March, May and July 2010. (b) Observed glacier front positions during the retreat period. The dashed lines correspond to July, August, September and October 2010. In both cases, the grey solid line corresponds to the initial geometry, September 2008.

5.5 Conclusions

Taking into account the main problems of Model 1 presented in Chapter 4, a refinement of the input velocities as well as an analysis of the oceanographic data has been performed. The analysis resulted in the proposition of Experiment 1, a model which implements a three–zone plume and refines the input velocities. The results for Experiment 1 improve the ones for Model 1, especially the retreat rate of the calving front during the summer months, and extend the best results for Model 1 from 350 m to 700 m. In consequence, the new modelled positions are a better approximation to reality.

However, there is a zone of the front where both models fail significantly. In the eastern part of the glacier front the dissimilarities are very important for both models. Consequently, a problem in the geometry is proposed as the cause for those discrepancies. And to address that problem, Experiment 2 suggests the extension of the calving front one node further east. Hence, there is a new node able to move back and forth. But the results of Experiment 2 indicate that, even if the model reduces the differences in the eastern part of the front, there is still a noteworthy problem in that area.

When looking more closely at the observed front behaviour, it is clear that the eastern margin moves forward during the advance season, and moves backward during the retreat season. Neither of the models, however, is accounting for that retreat in that part of the glacier front. Therefore, the eastern margin problem could be related to the geometry of the front, but it is more likely to be affected by the surface velocities in that area or the ambient properties of the fjord.

5.6 Supplementary figures

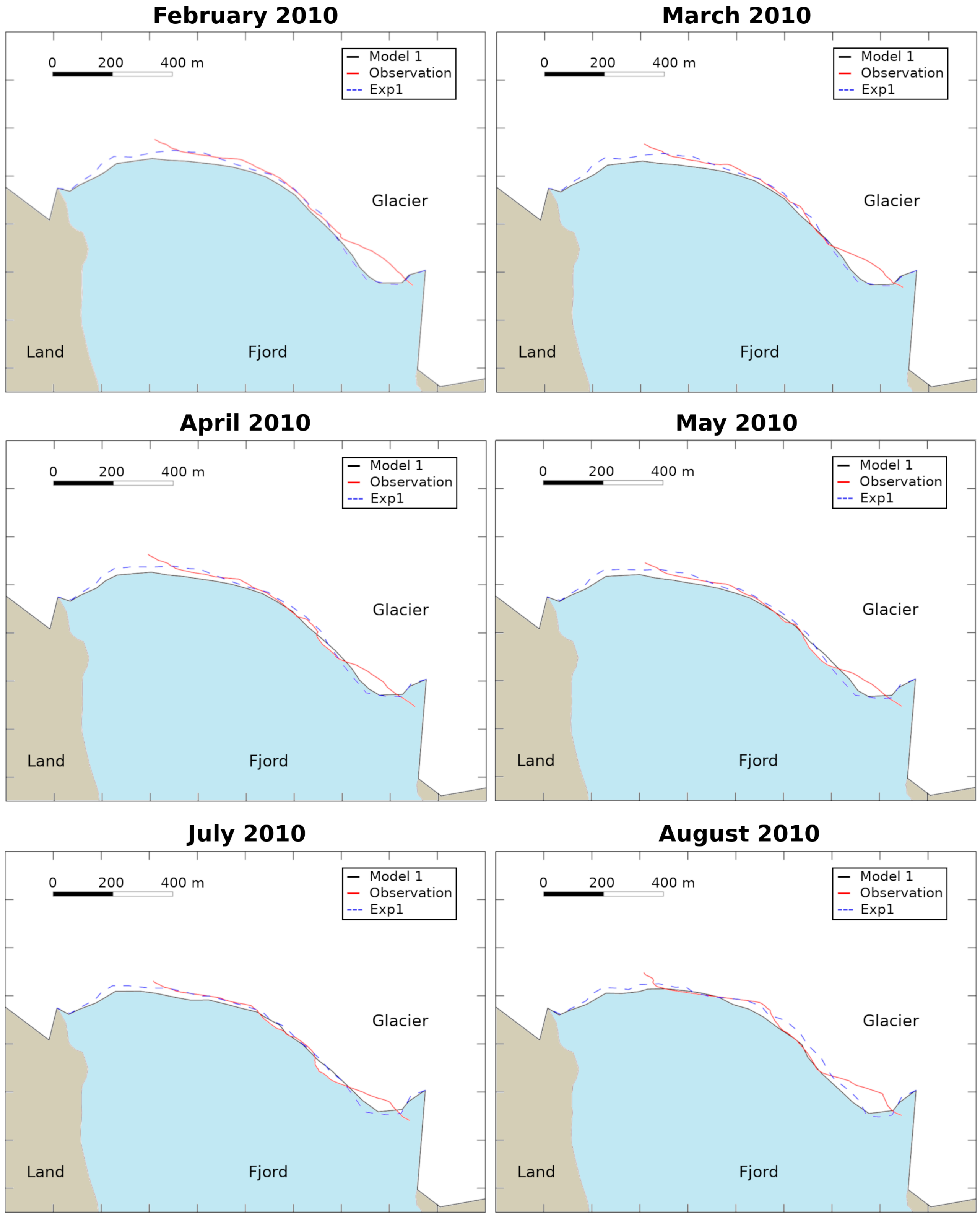

Figure 5.17: 2D aerial view of the glacier-fjord system for the rest of the months not presented in the Chapter. The solid black lines represent Model 1 contour of the glacier, the blue dashed line represent the front estimated by Experiment 1, and the red lines represent the observed front positions. Note that the observational data do not cover the westernmost part of the front.

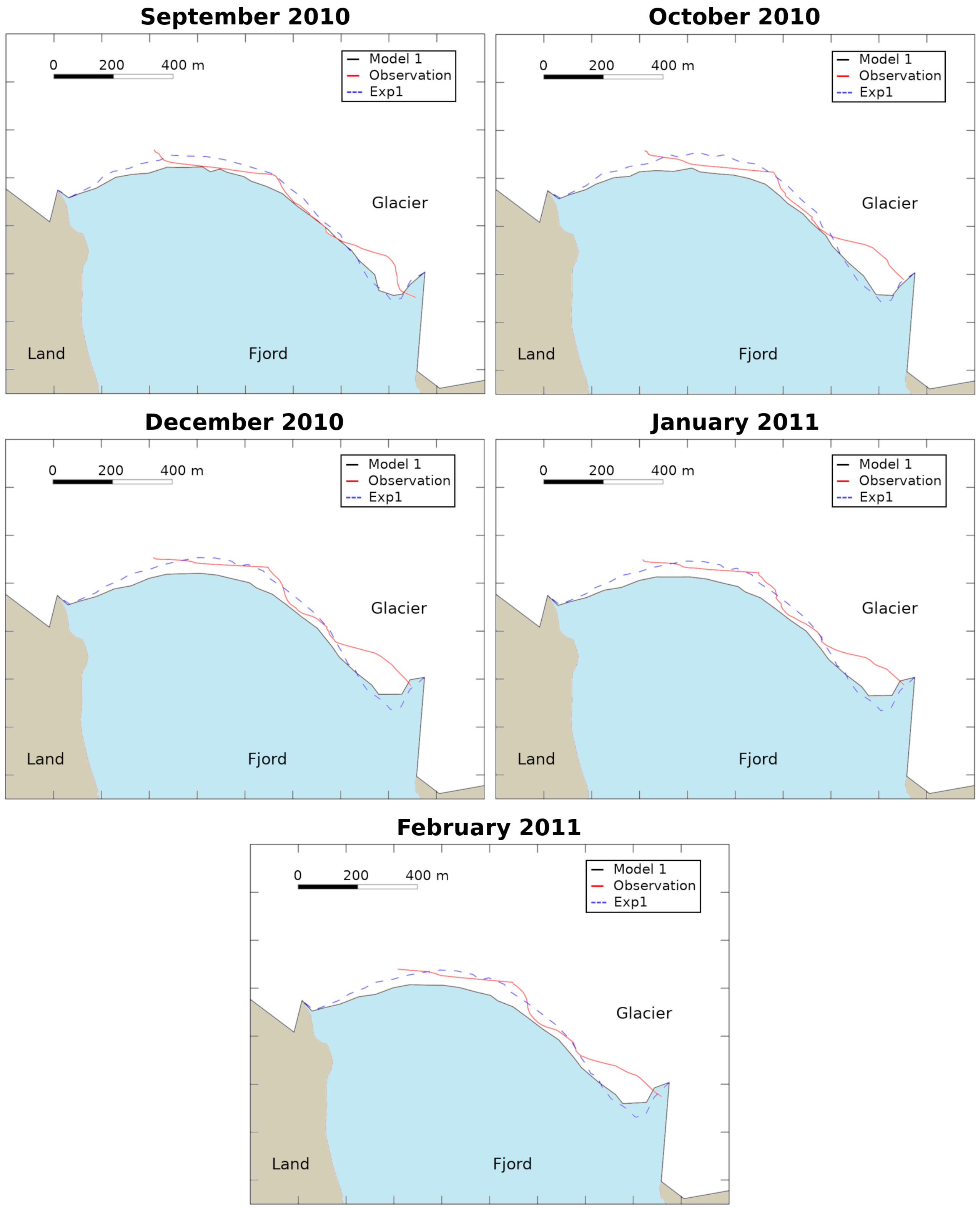

Figure 5.18: 2D aerial view of the glacier-fjord system for the rest of the months not presented in the Chapter. The solid black lines represent Model 1 contour of the glacier, the blue dashed line represent the front estimated by Experiment 1, and the red lines represent the observed front positions. Note that the observational data do not cover the westernmost part of the front.

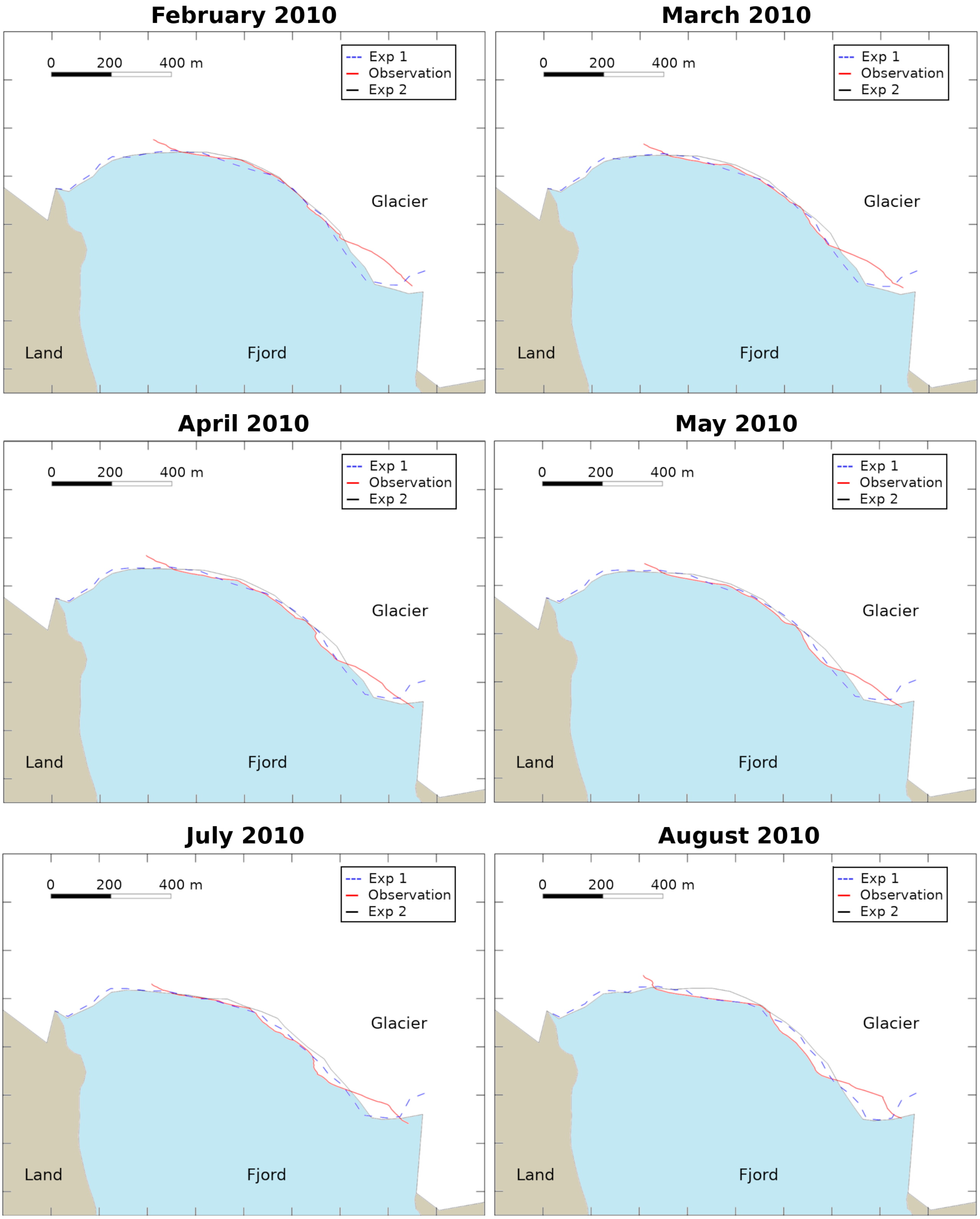

Figure 5.19: 2D aerial view of the glacier-fjord system for the rest of the months not presented in the Chapter. The solid black lines represent Experiment 2 contour of the glacier, the blue dashed line represent the front estimated by Experiment 1, and the red lines represent the observed front positions. Note that the observational data do not cover the westernmost part of the front.

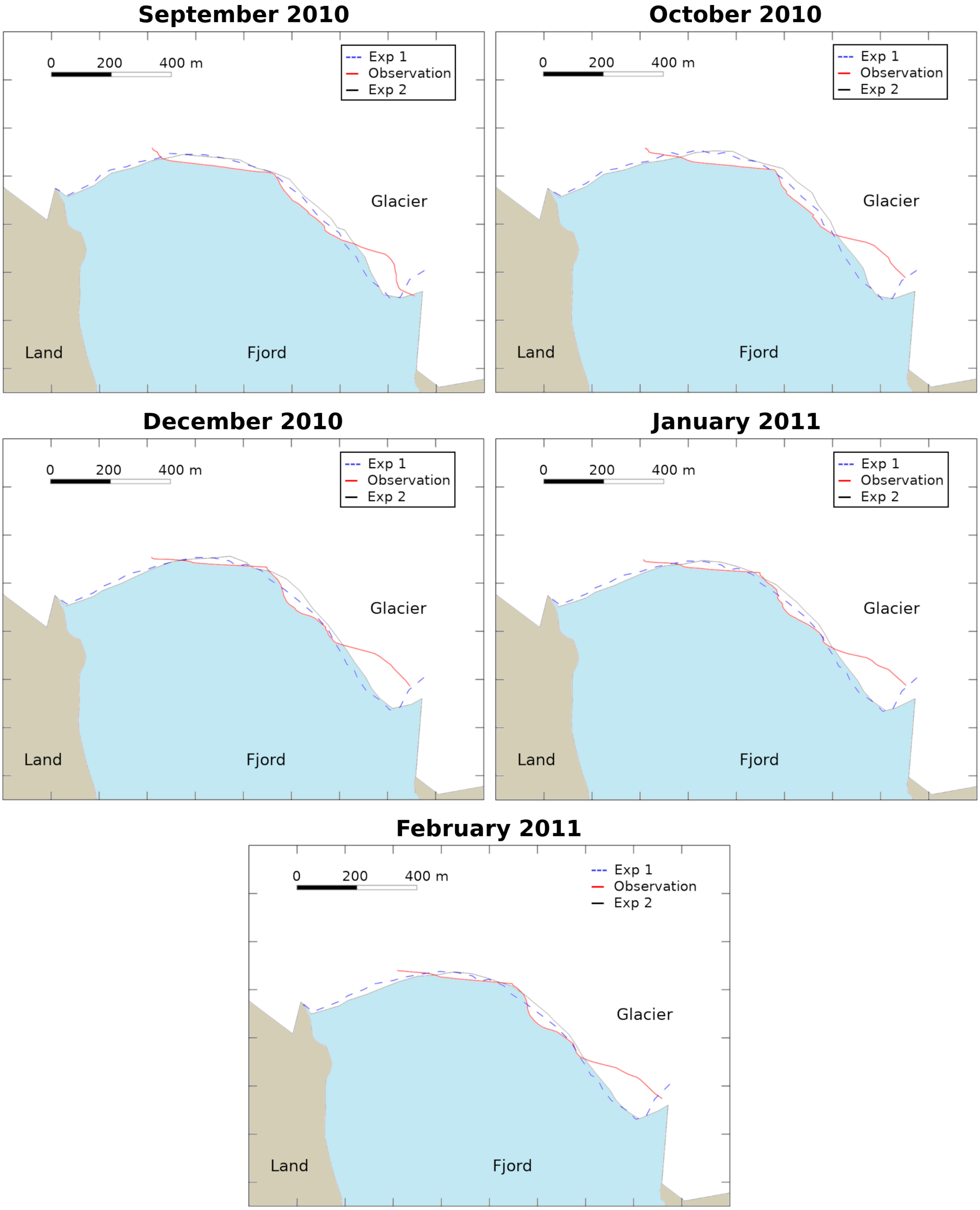
September 2010

October 2010

December 2010

January 2011

February 2011

Figure 5.20: 2D aerial view of the glacier-fjord system for the rest of the months not presented in the Chapter. The solid black lines represent Experiment 2 contour of the glacier, the blue dashed line represent the front estimated by Experiment 1, and the red lines represent the observed front positions. Note that the observational data do not cover the westernmost part of the front.

Chapter 6

Sensitivity Analysis

This chapter contains a sensitivity analysis performed on some of the input variables of the system. It starts by analysing how changes in the input velocities, surface meltwater and fjord ambient conditions can influence the melting rate in a typical winter month like January. Then, the same analysis is performed for a typical summer month like August. Finally, how the mentioned changes can affect the glacier front position is represented.

6.1 Motivation

To ensure the stability of such a complex model under varying input conditions, sensitivity analysis is crucial. Besides, analysing how these variations impact submarine melting, calving, and consequently, glacier front positions offers valuable insights for studying tidewater glaciers.

6.2 Winter Conditions

January 2010 represents a typical winter month in the behaviour of Hansbreen, i.e, low values of subglacial discharge, and cold, saline and stable fjord ambient conditions. Since winter conditions are not suitable to generate plumes, a variation in the surface velocities, which can affect the SMW but not the fjord conditions, is not going to produce any changes in plume activity. As for SMW, the increase of up to 100 % of the input values produces larger values of subglacial discharge, but not enough to generate plumes under the winter fjord conditions. Therefore, variations in the SWM are not producing changes in plume meltrate as well. But, when variations are applied to fjord ambient conditions, plumes do occur (Fig. 6.1).

A positive variation of 20 % in Temperature, with the respective reduction in Salinity – warmer and less saline water – produces a very low, but not null, value of plume meltrate. Beyond that, plume meltrate increases almost linearly with the percentage variation in T and S. Since changes of the same order in SMW are not able to generate plumes, for a winter month, plume meltrate is more sensitive to fjord ambient conditions than SMW. An example of how T and S variations affect plume meltrate are shown in Fig. 6.3.

Now, calving volume is more sensitive to variations in the input velocity than fjord conditions

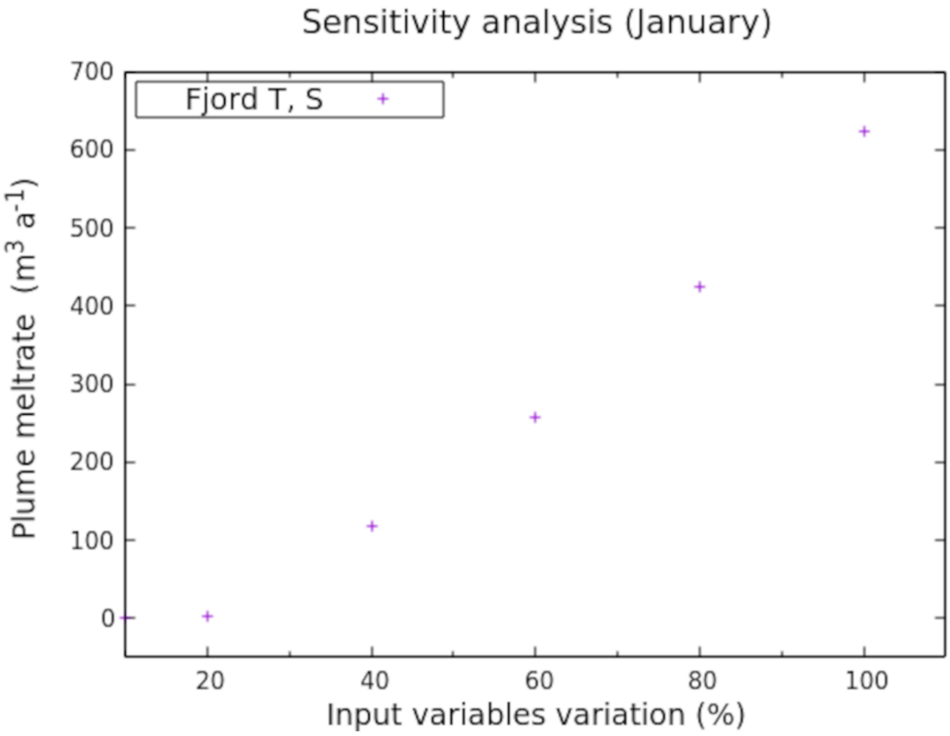

Figure 6.1: Changes in plume meltrate under a variation in the fjord ambient conditions (T, S) for January 2010.

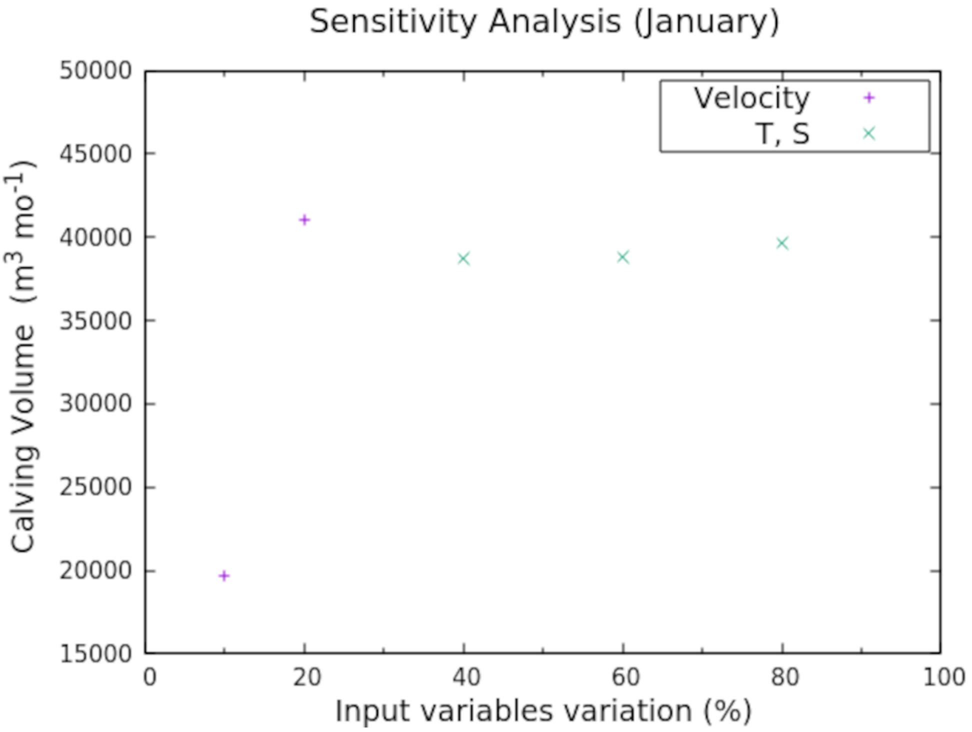

Figure 6.2: Changes in calving volume under a variation in the input velocities and the fjord ambient conditions (T, S) for January 2010.

(Fig. 6.2). Above an increase of 10 % of the velocities, calving volume becomes significantly larger when velocities grow. Below 10 %, there is no calving at all. In the same way, even an increase of 100 % in the input SMW is not enough to produce calving events. Fjord ambient conditions have an influence on submarine melting and, therefore, on calving as well, but the increase is relatively low and stable. Velocity variations, on the contrary, barely have an influence in the submarine melting but the increase in the calving volume is notable.

(a) January 2010 (-10% T, S)

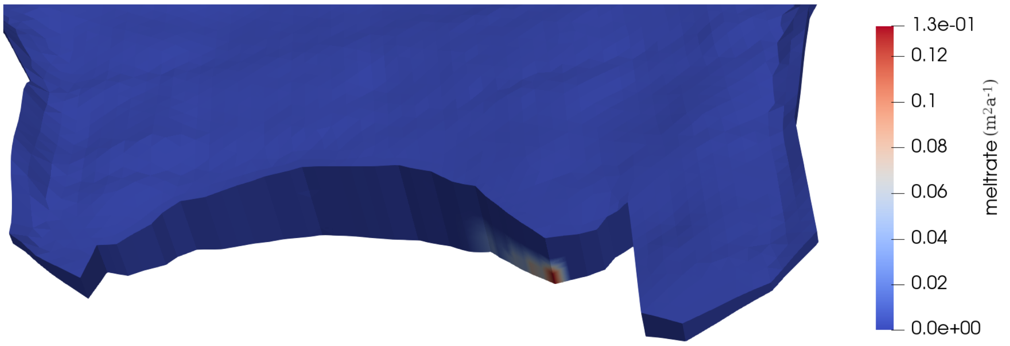

(b) January 2010 (+10% T, S)

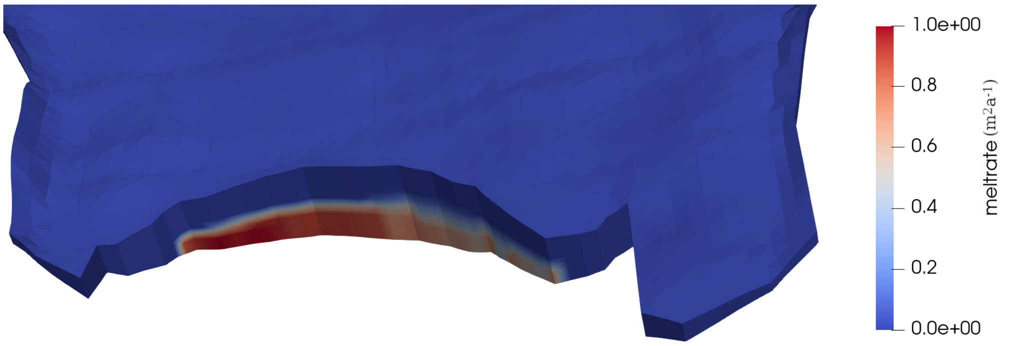

(c) January 2010 (+20% T, S)

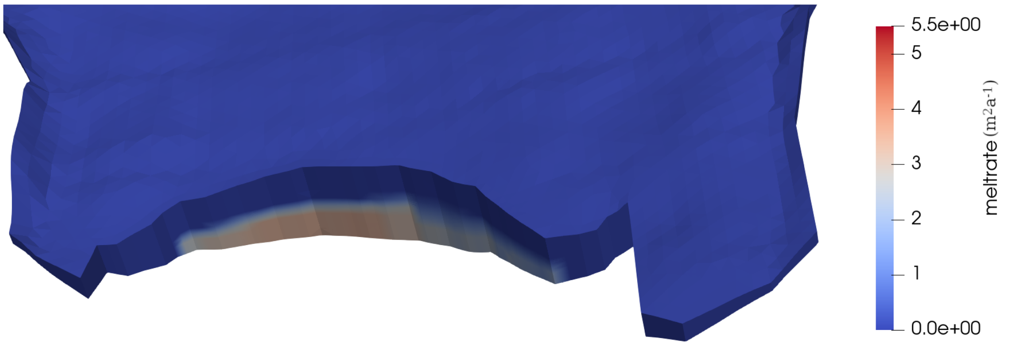

(d) January 2010 (+60% T, S)

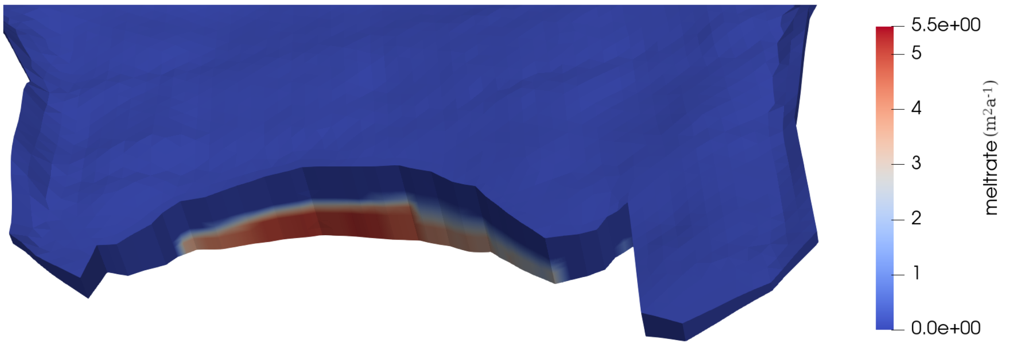

Figure 6.3: 3D aerial view of the glacier calving front corresponding to January 2010 for different variations of the observed fjord ambient conditions (Temperature and Salinity).

6.3 Summer Conditions

August 2010 represents a typical summer month in the behaviour of Hansbreen, i.e, large values of subglacial discharge, and warm and less saline fjord ambient conditions. A variation in the surface velocities within a 20 % barely produces any changes to subglacial discharge, and plume meltrate values remain constant. On the other hand, the increase of up to 100 % of the SMW values produces changes in the subglacial discharge and, thus, changes in plume meltrate as well (Fig. 6.4). Similarly, when variations are applied to fjord ambient conditions, there are some changes in the plume meltrate values (Fig. 6.4).

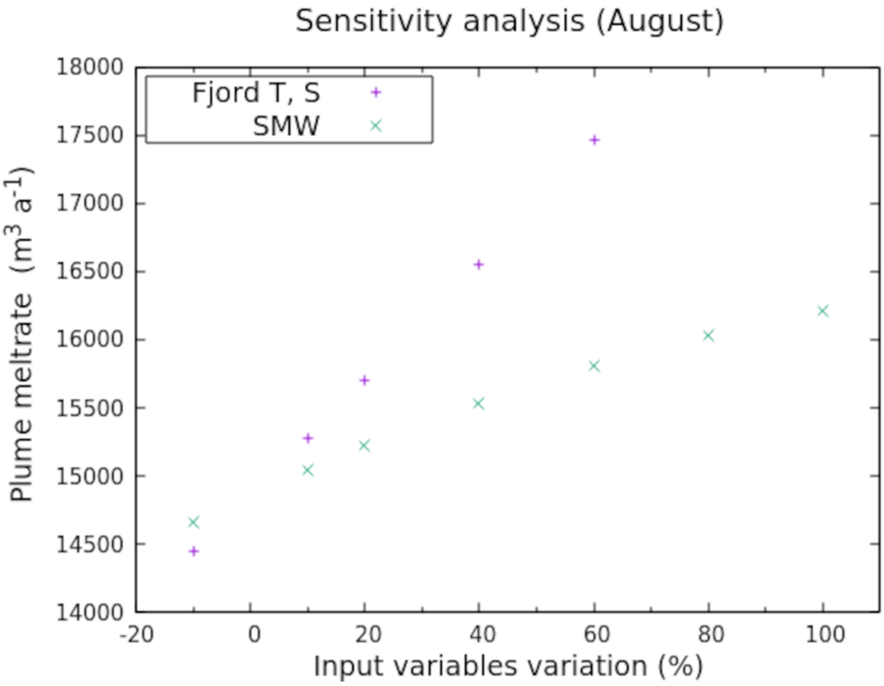

Figure 6.4: Changes in plume meltrate under variations in the input surface meltwater (SMW), and the fjord ambient conditions (T, S) for August 2010.

A negative variation of 10 % in Temperature, with the respective increase in Salinity – colder and more saline water – produces a decrease in the plume meltrate values. Likewise, a negative variation of 10 % in the input SMW and, therefore, a reduction of the subglacial discharge, also produces a decrease in the plume meltrate values. On the contrary, positive variations of both, Temperature –with the respective decrease of Salinity – and SMW result in largest values of plume meltrate. As in January, the relation between the variation in fjord ambient conditions and melting is linear, whereas the relation between the variation in SMW and plume meltrate is potential 6.4. Comparing both distributions, plume meltrate is also more sensitive to fjord ambient conditions than SMW in a summer month like August. The temperature and the salinity of fjord water, hence, is an essential factor not only in the occurrence of plumes, but also in their capacity to melt the glacier front. An example of how T and S variations affect plume meltrate are shown in Fig. 6.6. But once the conditions are suitable for the development of plumes – and this is always going to be the case for summer –, the changes in the SMW

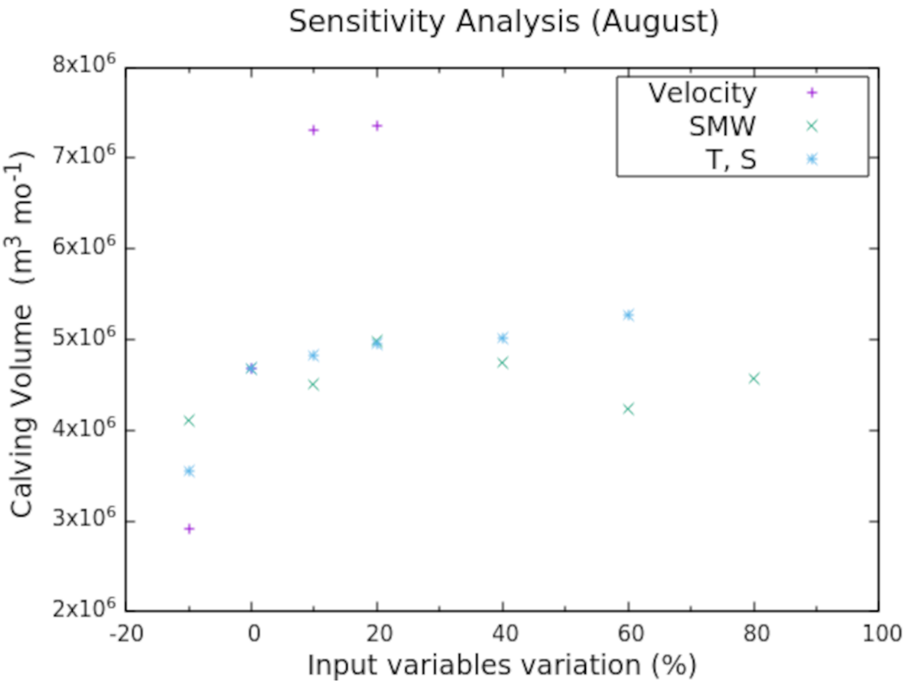

Figure 6.5: Changes in calving volume under a variation in the input velocities, the input surface meltwater and the fjord ambient conditions (T, S) for August 2010.

and, therefore, the changes in the subglacial discharge is also a very important factor in melting processes.

Calving volume is also more sensitive in summer to variations in the input velocity than fjord conditions and the surface meltwater (Fig. 6.5). Variations in the input SMW affect the submarine melting, but barely affect calving volume and there is not a clear tendency. Fjord ambient conditions, on the other side, present a potential relation with respect to calving volume. When increasing the temperature – with the respective decrease in the salinity – the calving volume becomes slightly larger. As for variation in the input velocities, between -10 and 20 % calving volume intensifies markedly, even if there is not a strengthening in the plume meltrate, but beyond that there is just a little increase. These results are in agreement with Cook et al. (2022), who found the hydrology–induced changes in terminus velocity to exert a strong control on calving in tidewater glaciers, and also that plume melt rates in excess of terminus velocity can exert a major control on terminus position.

6.4 Effect on the front positions

6.4.1 SMW

Since variations in the SMW are not enough to produce plumes, in a winter month there is no effect of the input SMW on the front positions. However, after running a summer month like August, the front positions present some changes (Fig. 6.7). A variation of -10 % yields to a more advanced front position, whereas variations above 10 % present more retreated positions – larger variations entail more retreated glacier fronts.

(a) August 2010 (-10% T, S)

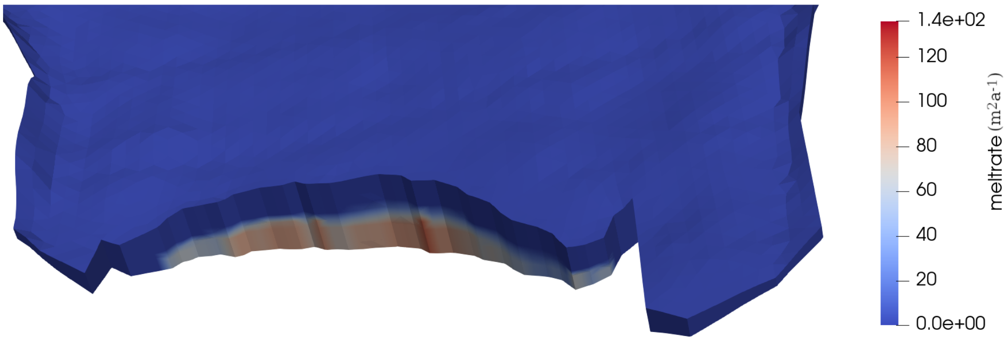

(b) August 2010 (+10% T, S)

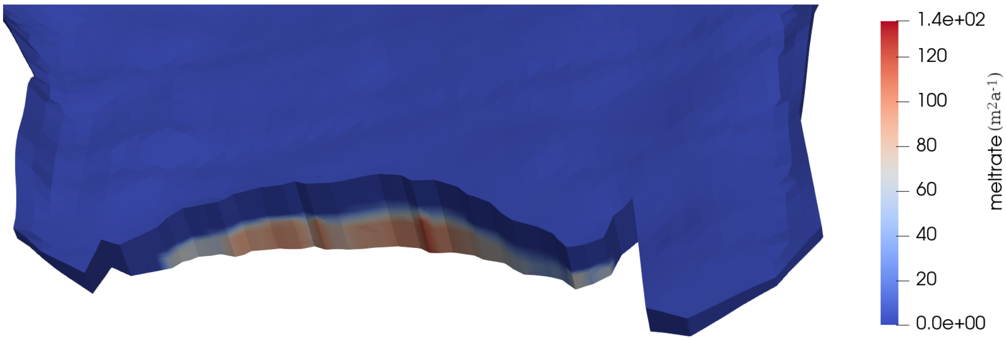

(c) August 2010 (+20% T, S)

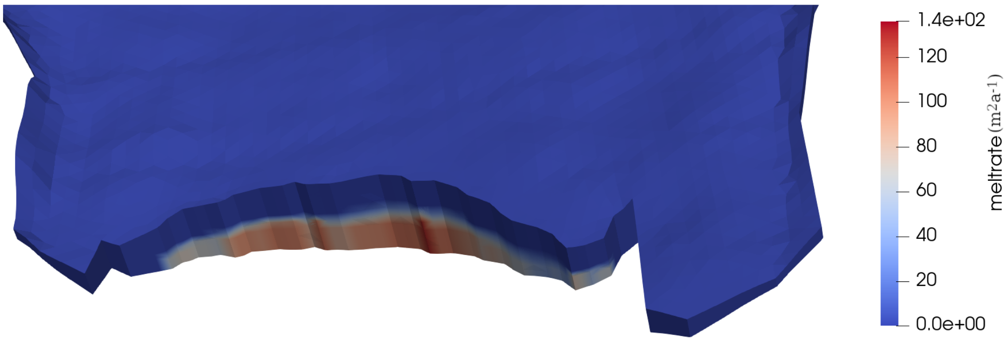

(d) August 2010 (+60% T, S)

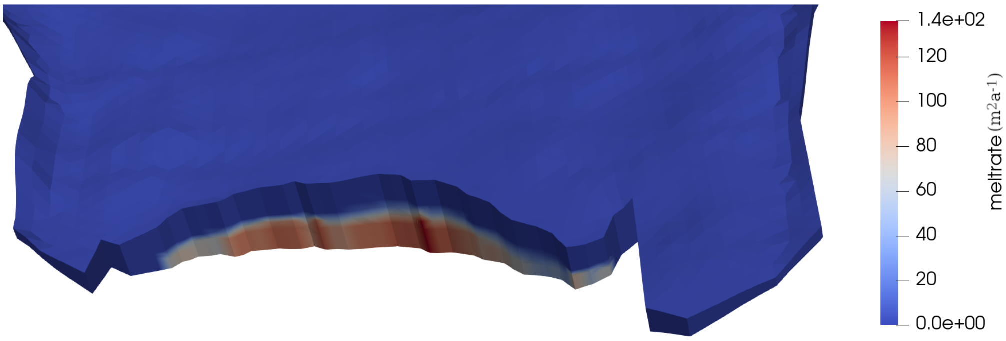

Figure 6.6: 3D aerial view of the glacier calving front corresponding to August 2010 for different variations of the observed fjord ambient conditions (Temperature and Salinity).

6.4.2 Velocity

Calving volume has proven to be sensitive to changes in the input velocity (Fig. 6.2 and Fig. 6.5). For a winter month, however, the calving generated, even in the maximum velocity variation conditions, is relatively low, whereas the front advances faster since velocities are

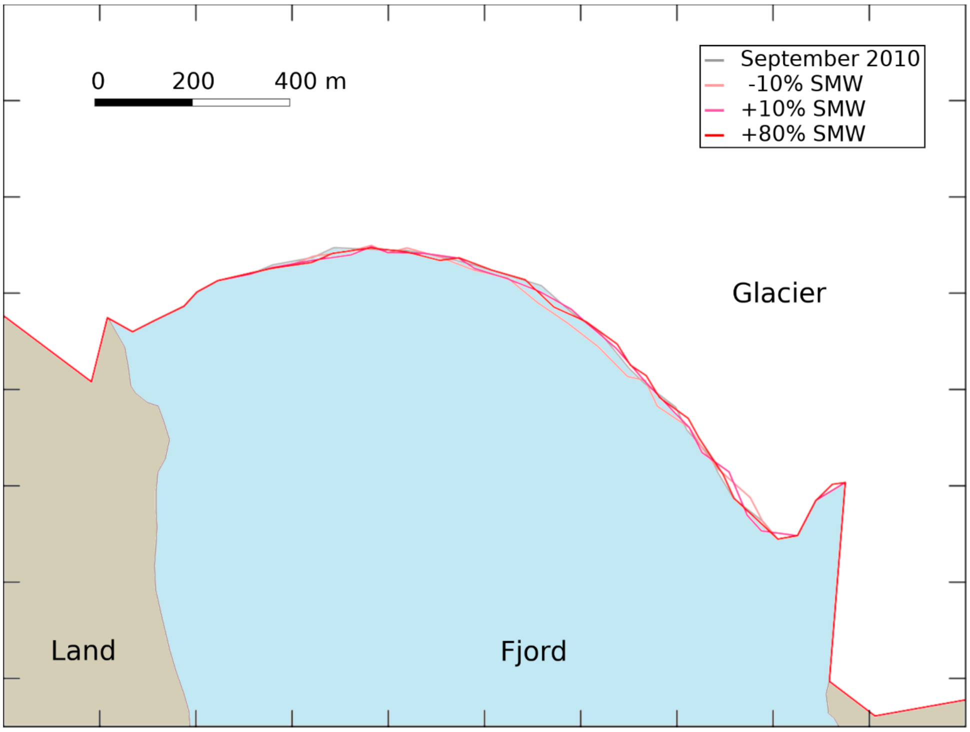

Figure 6.7: Modelled glacier front positions for September 2010 for different variations of input surface meltwater (SMW).

higher. Therefore, there are basically no changes in the front positions under velocity variations for a winter month (Fig. 6.9). On the contrary, in a summer month there are significant changes. When decreasing the velocity by 10 %, the resulting front position is more retreated because, even if calving decreases, the front advances slower. When increasing the velocity by 20 %, even if calving increases, the resulting front is more advanced than the rest because the glacier advances faster. However, when increasing the input velocities by just 10 %, the position is more retreated than when no variations are applied. This is because calving intensifies significantly and, at the same time, the front advances just slightly faster. Therefore, calving increases at a rate enough to compensate for the larger velocities. This is a very important finding because the increase of a 10 % is a very good approximation to solve the problem in the eastern margin (Fig. 6.8). Consequently, the underestimation in the input velocities in the eastern margin could be the reason for the large differences in that area produced by the model.

6.4.3 Fjord Ambient Conditions

Variations in the fjord ambient conditions, i.e., temperature and salinity, affect submarine melting and, therefore, calving and the resulting glacier front position after a simulation. For instance, for a winter month, changes above 40 % in the fjord conditions produce plume activity. Consequently, the front positions slightly change(Fig. 6.10). And this is more clear on a summer month when plume activity is stronger. By decreasing 10 % the ambient conditions – colder and more saline water – the resulting front position is more advanced. On the other hand, when increasing the ambient conditions – warmer and less saline water – the positions start to retreat

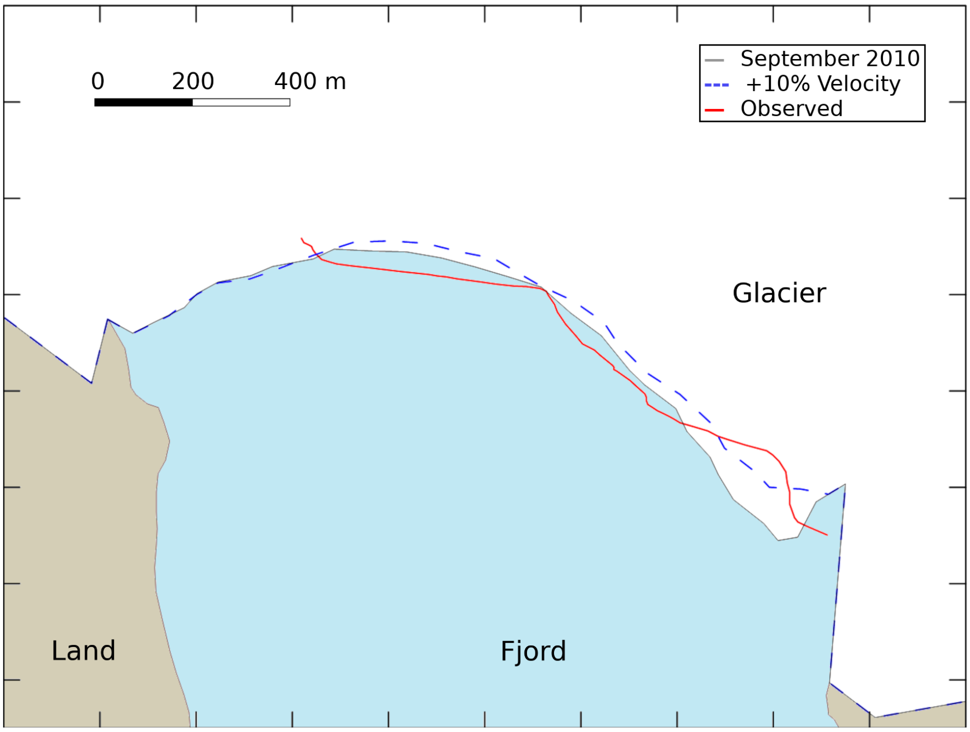

Figure 6.8: Modelled glacier front positions for February 2010 and September 2010 for different variations of input surface velocities.

due to the increase in plume meltrate and calving.

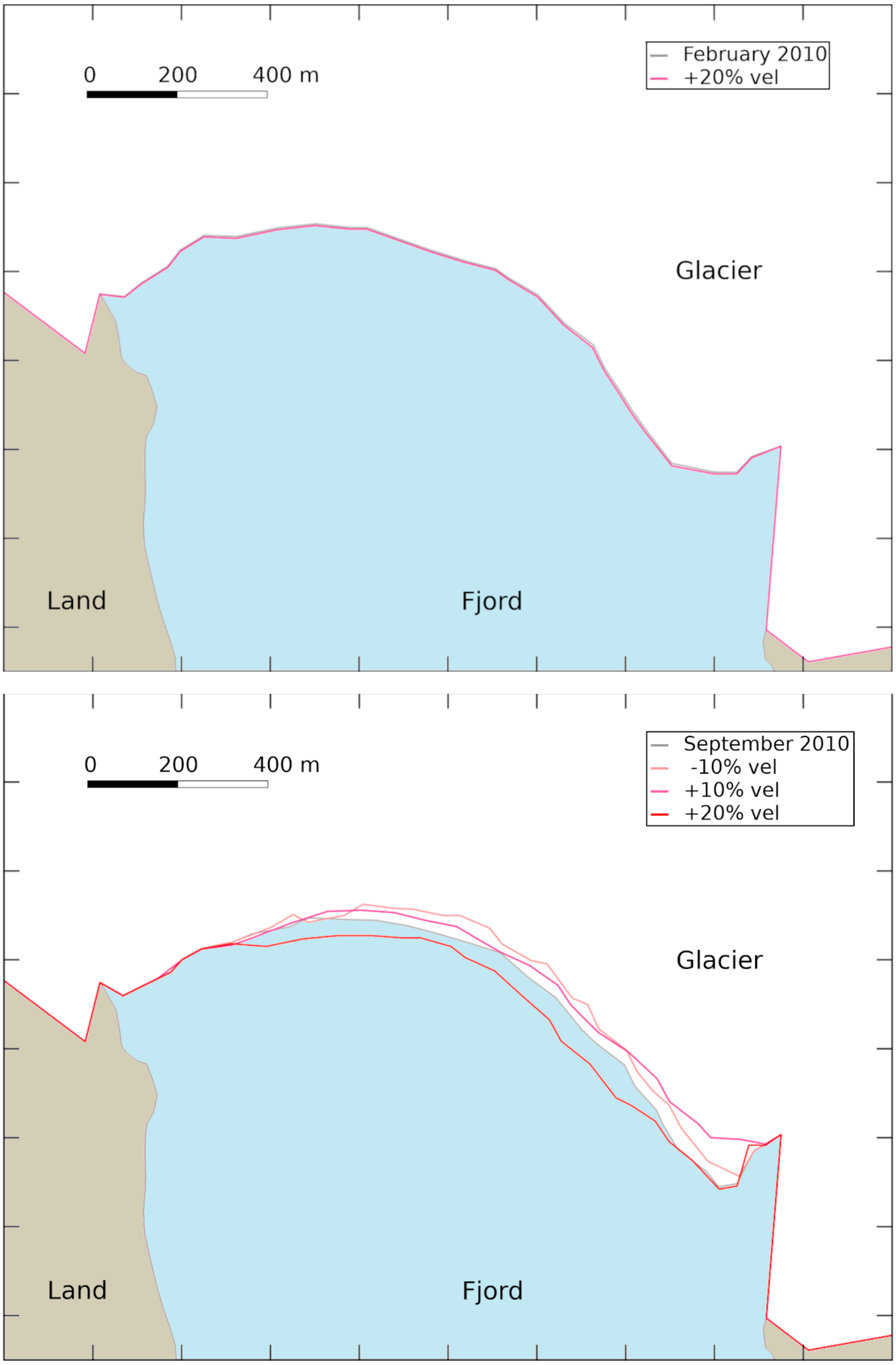

Figure 6.9: Modelled glacier front positions for February 2010 and September 2010 for different variations of input surface velocities.

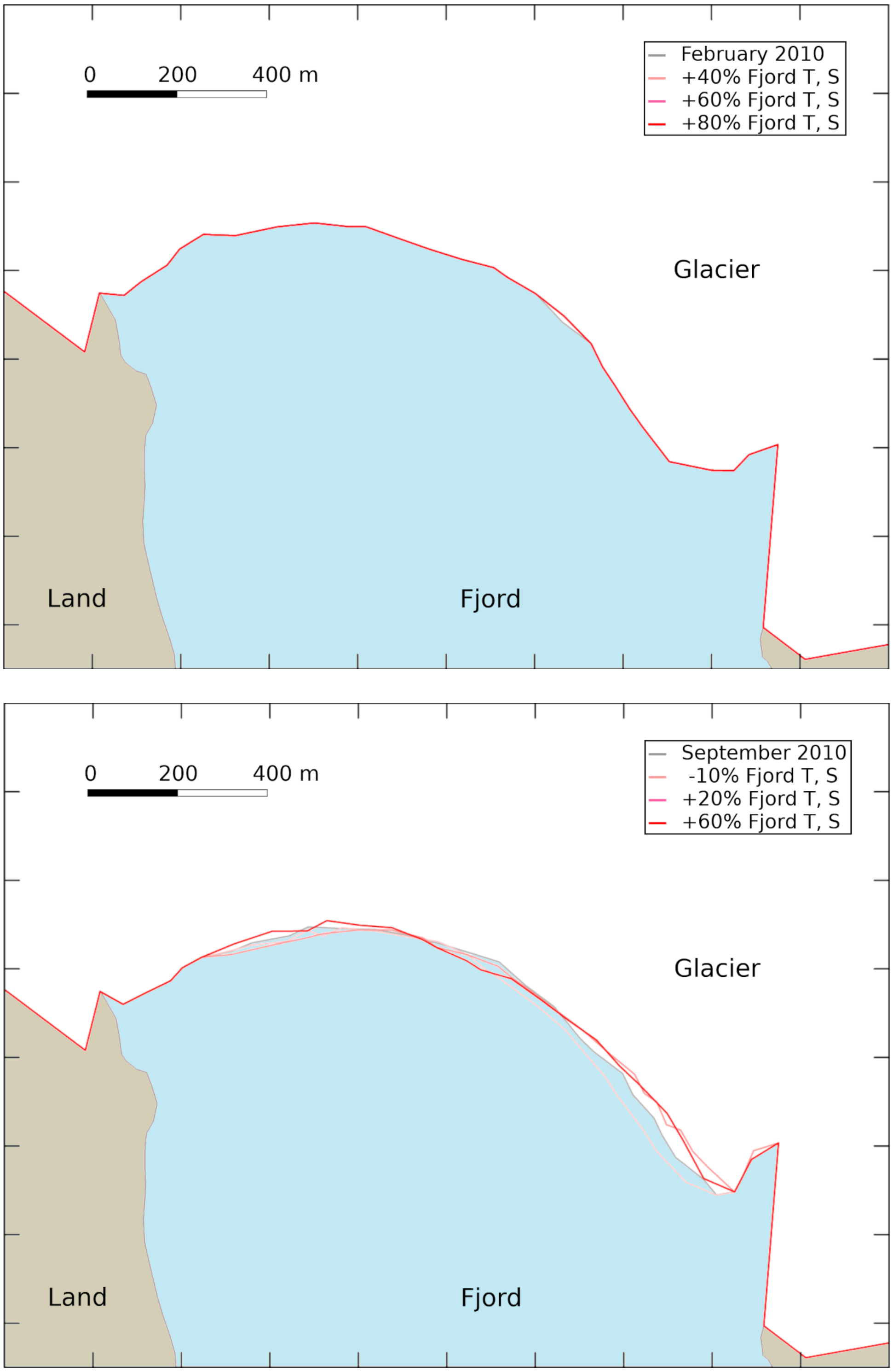

Figure 6.10: Modelled glacier front positions for February 2010 and September 2010 for different variations of the observed fjord ambient conditions (Temperature and Salinity).

Chapter 7

Conclusions and Outlook

The study of marine–terminating glaciers is crucial for understanding their dynamic response to climate change and their contributions to sea level rise. These glaciers exhibit complex interactions between ice, ocean, and atmosphere, making their behavior highly sensitive to both climatic and oceanographic conditions. In this thesis, we have focused on developing and implementing a three-dimensional glacier flow model to estimate the frontal ablation of marine-terminating glaciers, a critical component of their mass balance.

This conclusion chapter synthesizes the key findings from our model simulations by addressing the research objectives outlined in the introduction, discusses the implications of our results for the system that we are modelling, and suggests directions for future research. Given the complexity of the developed models, their potential limitations are also discussed. By integrating detailed physical processes and high-resolution data, our 3D glacier flow model provides novel insights into the mechanisms driving frontal ablation and enhances our predictive capabilities for tidewater glacier behavior.

In the following sections, we will summarise the main outcomes of our research, evaluate the model's performance, discuss about the limitations, and propose recommendations for further improvements and applications of our glacier model.

7.1 Conclusions

Calving and frontal ablation are essential processes to understand tidewater glacier dynamics. In this work, we have developed a 3D glacier dynamics model to estimate frontal ablation. To do so, the model includes modules to solve the main factors contributing to frontal ablation: submarine melting – through a plume model – and calving. Additionally, the model also accounts for atmospheric factors too through surface mass balance and surface meltwater.

The model solves the subglacial hydrology and provides subglacial discharge values that, in combination with appropriate fjord ambient conditions (temperature and salinity), are large enough to generate plumes at the calving front during most of the months of the year (except for the coldest months, i.e. from November to April). The results for the hydrology are consistent with other studies using a similar model (Cook et al., 2020), while the results for the plume melt rate are in agreement with other works on the Hansbreen–Hansbukta glacier–fjord system (De Andrés et al., 2018).

Larger values of subglacial discharge produce larger values of submarine melting. However, the results of the model indicate that changes in SMW alone are not able to explain plumes behaviour, turning fjord ambient conditions into a key factor in this process. Besides, the sensitivity analysis confirms the importance of fjord water conditions over SMW in terms of both submarine melting and calving volume. Consequently, the improvement of the first model through the inclusion of the three–zone plume results in a better performance of Experiment 1 versus Model 1.

Subglacial discharge distributes along the calving front and, in some cases, there seems to be a correspondence between the higher discharge values and a strong plume activity area. However, a more detailed study of the glacier hydrology would be necessary to establish such a relation.

Calving is the primary contributor to frontal ablation, followed by submarine melting. There is a clear relation between them, since larger values of submarine melting correlate with larger values of calving, but this work cannot establish the terms of that relation.

Model 1 is able to predict the evolution of the front position in terms of advance and retreat following a seasonal cycle with steep retreats in summer months and steady advances during the rest of the year. However, there are still differences between observed and modelled positions, especially in the eastern margin, where the longitudinal difference reaches 150 m in November 2010. In fact, when taking only the central part of the glacier front, the results improve significantly and the modelled positions become, on average, 40 % closer to the observed ones. In general, the difference between the modelled and observed front positions increases during the calving period, and we assume that the cause is an underestimation of calving by our model. Even so, the difference between the modelled and observed front positions decreases in some months, such as May, June, and July. In these months, the model is able to predict the front position with a very good level of agreement. In the eastern margin, our model does not produce enough calving events, which causes that large differences.

Experiment 1, with the implementation of the three–zone plume and the refinement of the input velocities, is also able to predict the evolution of the front position in terms of advance and retreat. It also follows a seasonal cycle, with steep retreats in summer months and steadily advances out of those months. Model 1 presents underestimation problems both in the advance and the retreat season. But Experiment 1 significantly improves the evolution in the retreat season. Therefore, Experiment 1 presents better results than Model 1 in terms of front evolution, and good results when compared to observations. The results for Experiment 1 improve the ones for Model 1, especially the retreat rate of the calving front during the summer months, and extend the best results for Model 1 at the central part of the front from 350 m to 700 m. In consequence, the new modelled positions are a better approximation to reality. Although a comparison between a 2D and a 3D model must be handled carefully, Experiment 1 results for the central 700 m of the calving front show a deviation from observation of ±10 m for most of the months of the simulation (around 70 % of the months for the period December 2009, March 2011). This is the same as the deviation value obtained by De Andrés et al. (2018) for their flow line model between April and August 2010.

However, there are still differences between observed and modelled positions, especially in the eastern margin where the longitudinal difference ascends to 150 m in November 2010 for Model 1 and Experiment 1. Experiment 2, just by extending the calving front one node further east, slightly improves those lateral differences, pointing out the importance of the geometry of the glacier front and the selection of the nodes that are allowed to advance and retreat. But the refinement is not enough and the problem persists. Even so, in some months such as May, June and July the longitudinal difference decreases, reaching a more than acceptable level of agreement. We see that the difference grows, especially for the eastern margin, during the calving period, especially in late summer and early autumn, and we assume that the cause could be an underestimation of calving by the models. In fact, when taking only the central part of the glacier front, and for Experiment 1 that part extends to 700 m – half of the total front – the results improve significantly. So, leaving the eastern margin behind, our model reproduces quite well the observations.

As for the eastern margin, when looking more closely at the observed front behaviour, it is clear that the eastern margin moves forward during the advance season, and moves backward during the retreat season. Neither of the models, however, is accounting for that retreat in that part of the glacier front. Therefore, the eastern margin problem could be related to the geometry of the front, but it is more likely to be affected by the surface velocities in that area or the ambient properties of the fjord. The sensitivity analysis pointed out that an increase of 10 % in the input velocity increases the calving activity as well, leading to a larger retreat in the eastern margin. Therefore, an underestimation in the input velocities in that area would be the reason why Model 1, Experiment 1 and Experiment 2 present notable differences in that zone.

Finally, Hansbreen is a largely studied glacier, becoming an essential context to test and to constrain our model. But, provided that we can count on having the required input data, this model could be applied to any other tidewater glacier or glacier–fjord system. This fact would turn the model into a valuable tool for studying other marine–terminating glaciers and, therefore, opens the possibility of estimating mass loss due to frontal ablation in such systems, which are crucial for understanding the current changes in the cryosphere

7.2 Models limitations

Even if the performance of the model developed in this work has provided some important findings, there are still some limitations.

Firstly, modelled velocities could be more refined. The differences between observed and modelled velocities are still a problem, especially in some specific months. And velocity has proven to be an essential variable both in the advance and the retreat season.

Secondly, there are aspects like the differences between SMW and subglacial discharge in some months that our model is not able to explain. For instance, the proposed change in the hydrological regime as possible cause for the mentioned differences. In addition, subglacial hydrology, plume and calving are not fully coupled, and SMW is an important factor in both submarine melting and calving.

Thirdly, our model is not properly solving the eastern margin of the glacier, even with Experiment 2. Looking at the evolution of the observed front, it advances and retreats in that zone in the same way as in the rest of the front. In our model, however, the retreat is minimum, which is causing those large differences when compared to observations. The sensitivity analysis has shown that input velocities could have been underestimated in that zone. However, we cannot establish such a thing because there are no stakes to constrain the velocity values in that area.

Lastly, the time–scale of this model is limited by the available data. We cannot say whether a longer simulation will result in a better agreement with observations, however, it would give us information on some results of the model that we cannot currently confirm. For example, do the differences in the eastern margin continue to increase or do they start to compensate at some point?

7.3 Future work

Such a complex model has helped us better understand some of the phenomena that occur in marine–terminating glaciers. But there are several issues that are still pending or that have not been explored in sufficient depth. Here we discuss some possible lines of future work to continue with the study of marine–terminating glaciers and take advantage of a model that, while good, still has room for improvement.

Firstly, surface velocity has proven to be an important factor not only in the advance season but also in the retreat, since they can affect calving. Daily velocities would imply daily inversions, and that is quite a lot in terms of computational cost, but it is known that velocities experiment important changes within days and maybe a 2–week or weekly inversions would improve the results of the model. Besides, a different sliding law could be implemented. For instance, a Coulomb–type sliding law, which has a direct relation with the hydrology through the hydraulic potential and has been used in some recent related works (Cook et al., 2022; Holmes et al., 2023), could improve the input modelled velocities. Besides, input velocities in the eastern margin have to be examined in detail, seeing that increasing the velocities 10 % solves the problem in that area.

Secondly, a more detailed study of the hydrology would let us better understand some aspects that this model is not able to explain. Besides, a fully coupling between the hydrology and the dynamic model with the calving and plume modules would be desirable to perform a more exhaustive study of the relation between all those processes.

Thirdly, considering that fjord ambient conditions have proven to be an essential factor in submarine melting due to plume activity and, consequently, for calving as well, a logical next step would be to use a fjord model to obtain better estimations of these conditions.

Finally, the study period of this experiment is limited by the available data and running a longer simulation could help us better understand the seasonal patterns and allow us to determine whether the lateral differences grow larger or start to decrease at some point.

Bibliography

AMAP: Snow, Water, Ice and Permafrost in the Arctic (SWIPA), Arctic Monitoring and Assessment Programme (AMAP), Oslo, URL https://www.amap.no/documents/doc/snow-water-ice-and-permafrost-in-the-arctic-swipa-2017/1610, [Last Access: 24/01/2024], 2017.

Amaral, T., Bartholomaus, T. C., and Enderlin, E. M.: Evaluation of iceberg calving models against observations from Greenland outlet glaciers, J. Geophys. Res. Earth Surf., 125, e2019JF005 444, https://doi.org/10.1029/2019JF005444, 2020.

Benn, D. I., Warren, C. R., and Mottram, R. H.: "Calving laws", "sliding laws" and the stability of tidewater glaciers, Ann. Glaciol., 46, 123–130, https://doi.org/10.3189/172756407782871161, 2007a.

Benn, D. I., Warren, C. R., and Mottram, R. H.: Calving processes and the dynamics of calving glaciers, Earth-Science Reviews, 82, 143–179, https://doi.org/10.1016/j.earscirev.2007.02.002, 2007b.

Benn, D. I., Cowtom, T., Todd, J., and Luckman, A.: Glacier calving in Greenland, Curr. Clim. Change Rep., 3, 282–290, https://doi.org/10.1007/s40641-017-0070-1, 2017.

Benn, D. I., Todd, J., Luckman, A., Bevan, S., Chudley, T. R., Åström, J., Zwinger, T., Cook, S., and Christoffersen, P.: Controls on calving at a large Greenland tidewater glacier: stress regime, self-organised criticality and the crevasse-depth calving law, J. Glaciol., pp. 1–16, https://doi.org/10.1017/jog.2023.81, 2023.

Benn, D. I. and Åström, J.: Calving glaciers and ice shelves, Advances in Physics: X, 3, 1513 819, https://doi.org/10.1080/23746149.2018.1513819, 2018.

Bojinski, S., M.Verstraete, Peterson, T. C., Richter, C., Simmons, A., and Zemp, M.: The concept of essential climate variables in support of climate research, applications, and policy, Bulletin of the American Meteorological Society, 95, 1431–1443, https://doi.org/10.1175/BAMS-D-13-00047.1, 2014.

Błaszczyk, M., Jania, J. A., and Kolondra, L.: Fluctuations of tidewater glaciers in Hornsund Fjord (Southern Svalbard) since the beginning of the 20th century, Polish Polar Researh, 4, 327–352, 2013.

Błaszczyk, M., Jania, J. A., Ciepły, M., Grabiec, M., Ignatiuk, D., Kolondra, L., Kruss, A., Luks, B., Moskalik, M., Pastusiak, T., Strzelewicz, A., Walczowski, W., and Wawrzyniak, T.: Factors controlling terminus position of Hansbreen, a tidewater glacier in Svalbard, J. Geophys. Res.: Earth Surf., 126, e2020JF005 763, https://doi.org/10.1029/2020JF005763, 2021.

Cassotto, R., Fahnestock, M., Amundson, J., Truffer, M., Boettcher, M., De la Peña, S., and Howat, I.: Non-linear glacier response to calving events, Jakobshavn Isbræ, Greenland, J. Glaciol., 65, 39–54, https://doi.org/10.1017/jog.2018.90, 2018.

Church, J., Clark, P., Cazenave, A., Gregory, J., Jevrejeva, S., Levermann, A., Merrifield, M., Milne, G., Nerem, R. S., Nunn, P., Payne, A., Pfeffer, W. T., Stammer, D., and Alakkat, U.: Sea Level Change. In Stocker, T.F., D. Qin, G.-K. Plattner, M. Tignor, S.K. Allen, J. Boschung, A. Nauels, Y. Xia, V. Bex and P.M. Midgley (eds.), Climate Change 2013: The Physical Science Basis. Contribution of Working Group I to the Fifth Assessment Report of the Intergovernmental Panel on Climate Change, pp. In press. 1137–1216, https://doi.org/10.1017/CBO9781107415324, 2013.

Cogley, J. G., Hock, R., Rasmussen, L. A., Arendt, A. A., Bauder, A., Braithwaite, R. J., Jansson, P., Kaser, G., Möller, M., Nicholson, L., and Zemp, M.: Glossary of glacier mass balance and related terms, IHP-VII Technical Documents in Hydrology No. 86, IACS Contribution No. 2, Paris: UNESCO-IHP., https://doi.org/10.5167/uzh-53475, 2011.

Cook, S. J., Chrostoffersen, P., Todd, J., Slater, D., and Chaucé, N.: Coupled modelling of subglacial hydrology and calving-front melting at Store Glacier, West Greenland, The Cryosphere, 14, 905–924, https://doi.org/10.5194/tc-14-905-2020, 2020.

Cook, S. J., Chrostoffersen, P., and Todd, J.: A fully-coupled 3D model of a large Greenlandic outlet glacier with evolving subglacial hydrology, frontal plume melting and calving, J. Glaciol., 68, 486–502, https://doi.org/10.1017/jog.2021.109, 2022.

Cownton, T. R., Slater, D. A., Sole, A., Goldberg, D., and Nienow, P.: Modeling the impact of glacial runoff on fjord circulation and submarine melt rate using a new subgrid-scale parameterization for glacial plumes, J. Geophys. Res. Oceans, 120, 796–812, https://doi.org/10.1002/2014JC010324, 2015.

Cownton, T. R., Todd, J. A., and Benn, D. I.: Sensitivity of tidewater glaciers to submarine melting governed by plume locations, Geophys. Res. Lett., 46, 11 219–11 227, https://doi.org/10.1029/2019GL084215, 2019.

Cuffey, K. and Paterson, W. S. B.: The physics of glaciers, Elsevier, Oxford: Elsevier, 4th edn., 2010.

De Andrés, E.: Coupling a fjord circulation model with subglacial discharge to a glacier dynamics model with calving, through the estimation of submarine melting at the glacier front, Phd Thesis, E.T.S.I. Telecomunicación (UPM), https://doi.org/10.20868/UPM.thesis.62689, 2020.

De Andrés, E., Otero, J., Navarro, F., Promińska, A., and Lapazaran, J.: A two-dimensional glacier–fjord coupled model applied to estimate submarine melt rates and front position changes of Hansbreen, Svalbard, J. Glaciol., 64, 745–758, https://doi.org/10.1017/jog.2018.61, 2018.

De Andrés, E., Otero, J., Navarro, F., and Walczowski, W.: Glacier–plume or glacier–fjord circulation models? A 2-D comparison for Hansbreen–Hansbukta system, Svalbard, J. Glaciol., 67, 797–810, https://doi.org/10.1017/jog.2021.27, 2021.

Edwards, T. L., Nowicki, S., Marzeion, B., Hock, R., Goelzer, H., Seroussi, H., Jourdain, N. C., Slater, D. A., Turner, F. E., Smith, C. J., McKenna, C. M., Simon, E., Abe-Ouchi, A., Gregory, J. M., Larour, E., Lipscomb, W. H., Payne, A. J., Shepherd, A., Agosta, C., Alexander, P., Albrecht, T., Anderson, B., Asay-Davis, X., Aschwanden, A., Barthel, A., Bliss, A., Calov, R., Chambers, C., Champollion, N., Choi, Y., Cullather, R., Cuzzone, J., Dumas, C., Felikson, D., Fettweis, X., Fujita, K., Galton-Fenzi, B. K., Gladstone, R., Golledge, N. R., Greve, R., Hattermann, T., Hoffman, M. J., Humbert, A., Huss, M., Huybrechts, P., Immerzeel, W., Kleiner, T., Kraaijenbrink, P., Le clec'h, S., Lee, V., Leguy, G. R., Little, C. M., Lowry, D. P., abd D. F. Martin, J. M., Da Maussion, F., Morlighem, M., O'Neill, J. F., Nias, I., Pattyn, F., Pelle, T., Price, S. F., Quiquet, A., Radić, V., Reese, R., Rounce, D. R., Rückamp, M., Sakai, A., Shafer, C., Schlegel, N., Shannon, S., abd F. Straneo, R. S. S., Sun, S., Tarasov, L., Trusel, L. D., Van Breedam, J., van de Wal, R., van den Broeke, M., Winkelmann, R., Zekollari, H., Zhao, C., Zhang, T., and Zwinger, T.: Projected land ice contributions to twenty-first-century sea level rise, Nature, 593, 74–82, https://doi.org/10.1038/s41586-021-03302-y, 2021.

EROS (USGS): Svlabard, Norway, `https://eros.usgs.gov/earthshots/svalbard-norway` [Last Access: 27/02/2024], 2013.

Farinotti, D., Huss, M., Fürst, J. J., Landmann, J., Machguth, H., Maussion, F., and Pandit, A.: A consensus estimate for the ice thickness distribution of all glaciers on Earth, Nature Geoscience, 12, 168–173, https://doi.org/10.1038/s41561-019-0300-3, 2019.

Finkelnburg, R.: Climate variability of Svalbard in the first decade of the 21st century and its impact on Vestfonna ice cap, Nordaustlandet, Phd Thesis, Technischen Universität Berlin, https://doi.org/10.14279/depositonce-3598, 2013.

Fretwell, P., Pritchard, H. D., Vaughan, D. G., Bamber, J. L., Barrand, N. E., Bell, R., Bianchi, C., Bingham, R. G., Blankenship, D. D., Casassa, G., Catania, G., Callens, D., Conway, H., Cook, A. J., Corr, H. F. J., Damaske, D., Damm, V., Ferraccioli, F., Forsberg, R., Fujita, S., Gim, Y., Gogineni, P., Griggs, J. A., Hindmarsh, R. C. A., Holmlund, P., Holt, J. W., Jacobel, R. W., Jenkins, A., Jokat, W., Jordan, T., King, E. C., Kohler, J., Krabill, W., Riger-Kusk, M., Langley, K. A., Leitchenkov, G., Leuschen, C., Luyendyk, B. P., Matsuoka, K., Mouginot, J., Nitsche, F. O., Nogi, Y., Nost, O. A., Popov, S. V., Rignot, E., Rippin, D. M., Rivera, A., Roberts, J., Ross, N., Siegert, M. J., Smith, A. M., Steinhage, D., Studinger, M., Sun, B., Welch, B. K. T. B. C., Wilson, D., Young, D. A., C.Xiangbin, and Zirizzotti, A.: Bedmap2: improved ice bed, surface and thickness datasets for Antarctica, The Cryosphere, 7, 375–393, https://doi.org/10.5194/tc-7-375-2013,2013, 2013.

Fried, M. J., Catania, G. A., Bartholomaus, T. C., Duncan, D., Davis, M., Stearns, L. A., Nahs, J., Shroyer, E., and Sutherland, D.: Distributed subglacial discharge drives significant submarine melt at a Greenland tidewater glacier, Geophys. Res. Lett., 42, 9328–9336, https://doi.org/10.1002/2015GL065806, 2015.

Gagliardini, O. and Werder, M.: Influence of increasing surface melt over decadal timescales on land-terminating Greenland-type outlet glaciers, J. Glaciol., 64, 700–710, https://doi.org/10.1017/jog.2018.59, 2018.

Gagliardini, O., Zwinger, T., Gillet-Chaulet, F., Durand, G., Favier, L., de Fleurian, B., Greve, R., Malinen, M., Martín, C., Råback, P., Ruokolainen, J., Sacchettini, M., Schäfer, M., Seddik, H., and Thies, J.: Capabilities and performance of Elmer/Ice, a new-generation ice sheet model, Geoscientific Model Development, 6, 1299–1318, https://doi.org/10.5194/gmd-6-1299-2013, 2013.

Gillet-Chaulet, F., Gagliardini, O., Seddik, H., Nodet, M., Durand, G., Ritz, C., Zwinger, T., Greve, R., and Vaughan, D. G.: Greenland ice sheet contribution to sea-level rise from a new-generation ice-sheet model, The Cryosphere, 6, 1561– 1576, https://doi.org/10.5194/tc-6-1561-2012, 2012.

Grabiec, M., Jania, J. A., Puczko, D., Kolondra, L., and Budzik, T.: Surface and bed morphology of Hansbreen, a tidewater glacier in Spitsbergen, Polish Polar Research, 33, 111–138, URL https://api.semanticscholar.org/CorpusID:59475531, [Last Access: 24/01/2024], 2012.

Hanna, E., Pattyn, F., Navarro, F., Favier, V., Goelzer, H., van den Broeke, M. R., Vizcaino, M., Whitehouse, P. L., Ritz, C., Bulthuis, K., and Smith, B.: Mass balance of the ice sheets and glaciers–progress since AR5 and challenges, Earth-Science Reviews, 201, 102 976, https://doi.org/10.1016/j.earscirev.2019.102976, 2020.

Hewitt, I. J.: Subglacial plumes, Annual Review of Fluid Mechanics, 52, 145–169, https://doi.org/10.1146/annurev-fluid-010719-060252, 2020.

Hock, R., Bliss, A., Marzeion, B., Giesen, R. H., Hirabayashi, Y., Huss, M., Radić, V., and Slangen, A. B. A.: GlacierMIP – A model intercomparison of global-scale glacier mass-balance models and projections, J. Glaciol., 65, 453–467, https://doi.org/10.1017/jog.2019.22, 2019.

Holland, D. M. and Jenkins, A.: Modeling Thermodynamic Ice–Ocean Interactions at the Base of an Ice Shelf, J. Phys. Oceanogr., 29, 1787–1800, https://doi.org/https://doi.org/10.1175/1520-0485(1999)029<1787:MTIOIA>2.0.CO;2, 1999.

Holmes, F. A., Kirchner, N., Kuttenkeuler, J., Krützfeldt, J., and Noormets, R.: Relating ocean temperatures to frontal ablation rates at Svalbard tidewater glaciers: Insights from glacier proximal datasets, Sci. Rep., 9, 9442, https://doi.org/https://doi.org/10.1038/s41598-019-45077-3, 2019.

Holmes, F. A., van Dongen, E., and Kirchner, N.: Modelled frontal ablation and velocities at Kronebreen, Svalbard, are sensitive to the choice of submarine melt rate scenario, J. Glaciol., pp. 1–12, https://doi.org/10.1017/jog.2023.94, 2023.

Hugonnet, R., McNabb, R., Berthier, E., Menounos, B., Nuth, C., Girod, L., Farinotti, D., Huss, M., Dussaillant, I., Brun, F., and Kääb, A.: Accelerated global glacier mass loss in the early twenty-first century, Nature, 592, 726–731, https://doi.org/10.1038/s41586-021-03436-z, 2021.

Huss, M. and Hock, R.: A new model for global glacier change and sea-level rise, Front. Earth Sci., 3, 54, https://doi.org/10.3389/feart.2015.00054, 2015.

Isaksen, K., Nordli, Ø., Førland, E. J., Łupikasza, E., Eastwood, S., and Niedźwiedź, T.: Recent warming on Spitsbergen – influence of atmospheric circulation and sea ice cover, J. Geophys. Res. Atmos., 121, 11 913–11 931, https://doi.org/10.1002/2016JD025606, 2016.

Jackson, R. H., Shroyer, E. L., Nash, J. D., Sutherland, D. A., Carroll, D., Fried, M. J., Catania, G. A., Bartholomaus, T. C., and Stearns, L. A.: Near-glacier surveying of a subglacial discharge plume: implications for plume parameterizations, Geophys. Res. Lett., 44, 6886–6894, https://doi.org/10.1002/2017GL073602, 2017.

Jackson, R. H., Nash, J. D., Kienholz, C., Sutherland, D. A., Amundson, J. M., Motyka, R. J., Winters, D., Skyllingstad, E., and Pettit, E. C.: Meltwater intrusions reveal mechanisms for rapid submarine melt at a tidewater glacier, Geophys. Res. Lett., 47, e2019GL085 335, https://doi.org/10.1029/2019GL085335, 2019.

Jacques Descloitres, MODIS Rapid Response Team, NASA/GSFC: Svalbard, Arctic Ocean, https://www.visibleearth.nasa.gov/images/68942/svalbard-arctic-ocean/689451 [Last Access: 27/02/2024], 2003.

Jenkins, A.: A one-dimensional model of ice shelf-ocean interaction, J. Geophys. Res., 96, 671–677, 1991.

Jenkins, A.: Convection-driven melting near the grounding lines of ice shelves and tidewater glaciers, J. Phys. Oceanogr., 41, 2279–2294, https://doi.org/10.1175/JPO-D-11-03.1, 2011.

Jouvet, G., Weidmann, Y., Kneib, M., Detert, M., Seguinot, J., Sakakibara, D., and Sugiyama, S.: Short-lived ice speed-up and plume water flow captured by a VTOL UAV give insights into subglacial hydrological system of Bowdoin Glacier, Remote Sens. Environ., 17, 389–399, https://doi.org/10.1016/j.rse.2018.08.027, 2018.

Kochtitzky, W., Copland, L., Van Wychen, W., Hugonnet, R., Hock, R., Dowdeswell, J. A., Benham, T., Strozzi, T., Glazovsky, A., Lavrentiev, I., Rounce, D. R., Millan, R., Cook, A., Dalton, A., Jiskoot, H., Cooley, J., Jania, J., and Navarro, F.: The unquantified mass loss of Northern Hemisphere marine-terminating glaciers from 2000–2020, Nat. Commun., 13, 5835, https://doi.org/10.1038/s41467-022-33231-x, 2022.

Korona, J., Berthier, E., Bernard, M., Rémy, F., and Thouvenot, E.: SPIRIT. SPOT 5 stereoscopic survey of Polar Ice: Reference Images and Topographies during the fourth International Polar Year (2007–2009), ISPRS Journal of Photogrammetry and Remote Sensing, 64, 204–212, https://doi.org/10.1016/j.isprsjprs.2008.10.005, 2009.

Levermann, A., Albrecht, T., Winkelmann, R., Martin, M. A., Haseloff, M., and Joughin, I.: Kinematic first-order calving law implies potential for abrupt ice-shelf retreat, The Cryosphere, 6, 273–286, https://doi.org/10.5194/tc-6-273-2012, 2012.

Luckman, A., Benn, D. I., Cottier, F., Bevan, S., Nilsen, F., and Inall, M.: Calving rates at tidewater glaciers vary strongly with ocean temperature, Nat. Commun., 6, 8566, https://doi.org/10.1038/ncomms9566, 2015.

Masson-Delmotte, V., Zhai, P., Pirani, A., Conners, S., Péan, C., Berger, S., Caud, N., Chen, Y., Goldfarb, L., Gomis, M. I., Huang, M., Leitzell, K., Lonnoy, E., Matthews, J. B. R., Maycock, T. K., Waterfield, T., Yelekçi, O., Yu, R., and Zhou, B., eds.: IPCC Climate Change 2021: The Physical Science Basis. Contribution of Working Group I to the Sixth Assessment Report of the Intergovernmental Panel on Climate Change, Cambridge University Press, Cambridge, UK and New York, NY, USA, https://doi.org/10.1017/9781009157896, 2021.

Meier, M. F., , Dyurgerov, M. B., Rick, U. K., O'neel, S., Pfeffer, W. T., Anderson, R. S., Anderson, S. P., and Glazovsky, A. F.: Glaciers dominate eustatic sea-level rise in the 21st century, Science, 317, 1064, https://doi.org/10.1126/science.1143906, 2007.

Mercenier, R., Lüthi, M. P., and Vieli, A.: Calving relation for tidewater glaciers based on detailed stress field analysis, The Cryosphere, 12, 721–739, https://doi.org/10.5194/tc-12-721-2018, 2018.

Morlighem, M., Bondzio, J., Seroussi, H., Rignot, E., Larour, E., Humbert, A., and Rebuffi, S.: Modeling of Store Gletscher's calving dynamics, West Greenland, in response to ocean thermal forcing, Geophys. Res. Lett., 43, 2659–2666, https://doi.org/10.1002/2016GL067695, 2016.

Morlighem, M., Williams, C. N., Rignot, E., An, L., Arndt, J. E., Bamber, J. L., Catania, G., Chauché, N., Dowdeswell, J. A., Dorschel, B., Fenty, I., Hogan, K., Howat, I., Hubbard, A., Jakobsson, M., Jordan, T. M., Kjeldsen, K. K., Millan, R., Mayer, L., Mouginot, J., Noël, B. P. Y., O'Cofaigh, C., Palmer, S., Rysgaard, S., Seroussi, H., Siegert, M. J., Slabon, P., Straneo, F., van den Broeke, M. R., Weinrebe, W., Wood, M., and Zinglersen, K. B.:

Distributed subglacial discharge drives significant submarine melt at a Greenland tidewater glacier, Geophys. Res. Lett., 44, 11 051–11 061, https://doi.org/10.1002/2017GL074954, 2017.

Morton, B. R., Taylor, G., and Turner, J. S.: Turbulent gravitational convection from maintained and instantaneous sources, Proceedings of the Royal Society A: Mathematical, Physical and Engineering Sciences, 234, 1–23, https://doi.org/10.1098/rspa.1956.0011, 1956.

Motyka, R. J., Dryer, W. P., Amundson, J., Truffer, M., and Fahnestock, M.: Rapid submarine melting driven by subglacial discharge, LeConte Glacier, Alaska, Geophys. Res. Lett., 40, 5153–5158, https://doi.org/10.1002/grl.51011, 2013.

Möller, M., Navarro, F., Huss, M., and Marzeion, B.: Projected sea-level contributions from tidewater glaciers are highly sensitive to chosen bedrock topography: A case study at Hansbreen, Svalbard, J. Glaciol., 69, 966–980, https://doi.org/10.1017/jog.2022.117, 2023.

Navarro, F. J., Martín-Español, A., Lapazaran, J. J., Grabiec, M., Otero, J., Vasilenko, E. V., and Puczko, D.: Ice volume estimates from Ground-Penetrating Radar surveys, Wedel Jarlsberg Land Glaciers, Svalbard, Arct. Antarct. Alp. Res., 46, 394–406, https://doi.org/10.1657/1938-4246-46.2.394, 2014.

Nick, F. M., Van der Veen, C., Vieli, A., and Benn, D. I.: A physically based calving model applied to marine outlet glaciers and implications for the glacier dynamics, J. Glaciol., 56, 781–794, https://doi.org/10.3189/002214310794457344, 2010.

Nordli, Ø., Wyszyński, P., Gjelten, H. M., Isaksen, K., Łupikasza, E., Niedźwiedź, T., and Przybylak, R.: Revisiting the extended Svalbard Airport monthly temperature series, and the compiled corresponding daily series 1898–2018, Polar Res., 39, https://doi.org/10.33265/polar.v39.3614, 2020.

Nye, J. F. and Perutz, M. F.: The distribution of stress and velocity in glaciers and ice-sheets, Proc. R. Soc. A Math. Phys. Sci., 239, 113–133, https://doi.org/10.1098/rspa.1957.0026, 1957.

Oerlemans, J., Jania, J., and Kolondra, L.: Application of a minimal glacier model to Hansbreen, Svalbard, The Cryosphere, 5, 1–11, https://doi.org/10.5194/tc-5-1-2011, 2011.

Otero, J., Navarro, F. J., Martin, C., Cuadrado, M. L., and Corcuera, M.: A three-dimensional calving model: numerical experiments on Johnsons Glacier, Livingston Island, Antarctica, J. Glaciol., 56, 200–214, https://doi.org/10.3189/002214310791968539, 2010.

Otero, J., Navarro, F. J., Lapazaran, J. J., Welty, E., Puczko, D., and Finkelnburg, R.: Modeling the controls on the front position of a tidewater glacier in Svalbard, Front. Earth Sci., 5, 29, https://doi.org/10.3389/feart.2017.00029, 2017.

Perez-Doña, I. and Otero, J.: Sobre el uso de Kriging Bayesiano para estimar la evolución de las velocidades en superficie del Glaciar Hansbreen (Svalbard), 10a Asamblea Hispano-Portuguesa de Geodesia y Geofísica, pp. 1137–1140, https://doi.org/10.7419/162.07.2023, 2023.

Pörtner, H. O., Roberts, D. C., Masson-Delmotte, V., Zhai, P., Tignor, M., Poloczanska, E., Mintenbeck, K., Alegría, A., Nicolai, M., Okem, A., Petzold, J., Rama, B., and Weyer, N., eds.: IPCC Special Report on the Ocean and Cryosphere in A Changing Climate, Cambridge University Press, Cambridge, UK and New York, NY, USA, https://doi.org/10.1017/9781009157964, 2019.

Pętlicki, M., Ciepły, M., Jania, J., Promińska, A., and Kinnard, C.: Calving of a tidewater glacier driven by melting at the waterline, J. Glaciol., 61, 851–863, https://doi.org/10.3189/2015JoG15J062, 2015.

RGI Consortium, .: Randolph Glacier Inventory - A Dataset of Global Glacier Outlines, Version 6, https://doi.org/10.7265/4m1f-gd79, 2017.

Rignot, E., Koppes, M., and Velicogna, I.: Rapid submarine melting of the calving faces of west Greenland glacier, Nature Geoscience, 3, 187–191, https://doi.org/10.1038/ngeo765, 2010.

Slater, D. A., Nienow, P., Cownton, T. R., Goldberg, D., and Sole, A.: Effect of near-terminus subglacial hydrology on tidewater glacier submarine melt rates, Geophys. Res. Lett., 42, 2861–2868, https://doi.org/10.1002/2014GL062494, 2015.

Slater, D. A., Straneo, F., Das, S. B., Richards, C. G., Wagner, T. J. W., and Nienow, P. W.: Localized plumes drive front-wide ocean melting of a Greenlandic tidewater glacier, Geophys. Res. Lett., 45, 12 350–12 358, https://doi.org/10.1029/2018GL080763, 2018.

Straneo, F. and Cenedese, C.: The dynamics of Greenland's glacial fjords and their role in climate, Annu. Rev. Mar. Sci, 7, 89–112, https://doi.org/10.1146/annurev-marine-010213-135133, 2015.

Sutherland, D. A., Jackson, R. H., Kienholz, C., Amundson, J. M., Dryer, W. P., Duncan, D., Eidam, E. F., Motyka, R. J., and Nash, J. D.: Direct observations of submarine melt and subsurface geometry at a tidewater glacier, Science, 365, 369–374, https://doi.org/10.1126/science.aax3528, 2019.

Todd, J. and Christoffersen, P.: Are seasonal calving dynamics forced by buttressing from ice mélange or undercutting by melting? Outcomes from full-Stokes simulations of Store Glacier, West Greenland, The Cryosphere, 8, 2353–2365, https://doi.org/10.5194/tc-8-2353-2014, 2014.

Todd, J., Christoffersen, P., Zwinger, T., Råback, P., Chauché, N., Benn, D., Luckman, A., Ryan, J., Toberg, N., Slater, D., and Hubbard, A.: A full-Stokes 3D calving model applied to a large greenlandic glacier, J. Geophys. Res.: Earth Surf., 123, 410–432, https://doi.org/10.1002/2017JF004349, 2018.

Todd, J., Christoffersen, P., Zwinger, T., Râback, P., and Benn, D. I.: Sensitivity of a calving glacier to ice–ocean interactions under climate change: new insights from a 3-D full-Stokes model, The Cryosphere, 13, 1681–1694, https://doi.org/10.5194/tc-13-1681-2019, 2019.

Vallot, D., Adinugroho, S., Strand, R., How, P., Pettersson, R., Benn, D. I., and Hulton, N. R. J.: Automatic detection of calving events from time-lapse imagery at Tunabreen, Svalbard, Geosci. Instrum. Method. Data Syst., 8, 113–127, https://doi.org/10.5194/gi-8-113-2019, 2019.

Van der Veen, C.: Tidewater calving, J. Glaciol., 42, 375–385, https://doi.org/10.3189/S0022143000004226, 1996.

Vaughan, D. G., Comiso, J., Allison, I., Carrasco, J., Kaser, G., Kwok, R., Mote, P., Murray, T., Paul, F., Ren, J., Rignot, E., Solomina, O., Steffen, K., and Zhang, T.: Observations: Cryosphere. In: Climate Change 2013: The Physical Science Basis. Contribution of Working Group I to the Fifth Assessment Report of the Intergovernmental Panel on Climate Change, Cambridge University Press, Cambridge, UK and New York, NY, USA, 2013.

Vieli, A., Funk, M., and Blatter, H.: Tidewater glaciers: Frontal flow acceleration and basal sliding, Ann. Glaciol., 31, 217–221, https://doi.org/10.3189/172756400781820417, 2000.

Vieli, A., Funk, M., and Blatter, H.: Flow dynamics of tidewater glaciers: A numerical modelling approach, J. Glaciol., 47, 595–606, https://doi.org/10.3189/172756501781831747, 2001.

Vieli, A., Jania, J., and Kolondra, L.: The retreat of a tidewater glacier: Observations and model calculations on Hansbreen, Spitsbergen, J. Glaciol., 48, 592–600, https://doi.org/10.3189/172756502781831089, 2002.

Werder, M. A., Hewitt, I. J., Schoof, C. G., and Flowers, G. E.: Modeling channelized and distributed subglacial drainage in two dimensions, J. Geophys. Res.: Earth Surf., 118, 21402 158, https://doi.org/10.1002/jgrf.20146, 2013.

Xie, S., Dixon, T. H., Holland, D. M., Voytenko, D., and Vaňková, I.: Rapid iceberg calving following removal of tightly packed pro-glacial mélange, Nat. Commun., 10, 3250, https://doi.org/10.1038/s41467-019-10908-4, 2019.